

**Monitoring the Electron Beam Position
at the
TESLA Test Facility Free Electron Laser**

D i s s e r t a t i o n

zur Erlangung des akademischen Grades

d o c t o r r e r u m n a t u r a l i u m

(Dr. rer. nat.)

im Fach Physik

eingereicht an der

Mathematisch-Naturwissenschaftlichen Fakultät I

der Humboldt-Universität zu Berlin

von

Thorsten Kamps

geboren am 24.01.1970 in Hilten (jetzt Neuenhaus)

Präsident der Humboldt-Universität zu Berlin

Prof. Dr. Dr. h.c. Hans Meyer

Dekan der Mathematisch-Naturwissenschaftlichen Fakultät I

Prof. Dr. Jürgen Rabe

Gutachter: 1. Prof. Dr. Eberhard Jaeschke
 2.
 3.

Tag der mündlichen Prüfung:

Abstract

The operation of a free electron laser working in the Self Amplified Spontaneous Emission mode (SASE FEL) requires the electron trajectory to be aligned with very high precision in overlap with the photon beam. In order to ensure this overlap, one module of the SASE FEL undulator at the TESLA Test Facility (TTF) is equipped with a new type of waveguide beam position monitor (BPM). Four waveguides are arranged symmetrically around the beam pipe, each slot couples through a small slot to the electromagnetic beam field. The induced signal depends on the beam intensity and on the transverse beam position in terms of beam-to-slot distance. With four slot-waveguide combinations a linear position sensitive signal can be achieved, which is independent of the beam intensity. The signals transduced by the slots are transferred by ridged waveguides through an impedance matching stage into a narrowband receiver tuned to 12 GHz. The present thesis describes design, tests, and implementation of this new type of BPM.

Zusammenfassung

Der Betrieb eines Freien Elektronen Lasers (FEL), bei dem sich die spontan emittierte Undulatorstrahlung über Wechselwirkung mit dem Elektronenstrahl selbst verstärkt wird, setzt eine präzise Ausrichtung des Elektronenstrahls mit dem Photonenstrahl voraus. Um den Überlapp von Elektronen- und Photonenstrahl zu gewährleisten, wurde ein neuartiger Typ von Wellenleiter-Strahllagemonitor entwickelt, der in eine Vakuumkammer des Undulators des FELs der TESLA Test Facility (TTF) integriert ist. Vier um das Strahlrohr verteilte Wellenleiter koppeln über schmale Schlitze einen Bruchteil jenes elektromagnetischen Feldes aus, welches den Strahl begleitet. Die induzierten Signale hängen von der transversalen Strahlposition und der Strahlintensität ab. Mit vier Schlitz-Wellenleiter Paaren läßt sich ein lineares Signal ableiten, anhand dessen die Position des Elektronenstrahls bestimmt werden kann. Die induzierten Signale werden mittels eines stegbelasteten Wellenleiters in die erste Stufe eines bei 12 GHz arbeitenden Empfängers zugeführt. Die vorliegende Arbeit beschreibt Design, Tests und Implementierung dieses neuartigen Typs von Strahllagemonitor.

Contents

1	Introduction	1
2	TESLA Test Facility Free Electron Laser	3
2.1	TESLA Test Facility	3
2.2	SASE FEL at the TTF	4
2.2.1	SASE FEL Process	5
2.2.2	Electron Beam Requirements	8
2.2.3	Undulator	8
2.3	Electron Beam Diagnostics	10
2.3.1	Strategy	10
2.3.2	Requirements for the Undulator BPM System	11
2.3.3	Components	12
3	Microwave Characterization	19
3.1	Overview	19
3.2	Waveguide Design	20
3.3	Slot Coupling	25
3.3.1	Introduction to the Problem	25
3.3.2	Coupling between Beam Field and Rectangular Waveguide	26
3.3.3	Simulation of the BPM Coupling	31
3.4	Transition Step	35
3.5	Wake Field Estimation	37
3.5.1	Wake Field Quota	37
4	Measurements	41
4.1	Measurements in Laboratory	41
4.1.1	Simulating an Electron Beam	41
4.1.2	Testbench Description	43
4.1.3	Transfer Characteristics	47
4.1.4	Gain	50

4.1.5	Coupling Slot Angle	52
4.1.6	Sensitivity	54
4.2	Measurements with Beam at CTF2	58
4.2.1	Measurement Setup	58
4.2.2	Measurements	59
4.3	Measurements with Beam at SBTF	63
4.3.1	Setup and Preparatory Work	63
4.3.2	Measurements	65
5	Calibration Techniques	69
5.1	Motivation	69
5.2	Modelling BPM Output Signals	70
5.2.1	Recalling the Image Charge Model	70
5.2.2	From Ideal to Real BPM Heads	71
5.3	Beam Based Model Fit	71
5.3.1	Assumptions	72
5.3.2	Gain Detection	72
5.3.3	Simulation of the Method	73
5.3.4	Test with Measured Data	73
5.4	BPM Offset Determination	74
5.4.1	Local Orbit Correction	76
5.5	Beam Based Alignment	77
5.5.1	Global Dispersion Correction	78
5.6	Beam Position Determination	79
5.6.1	Normalized and Skew Differences	79
5.6.2	Linearization of Signalfuncions	80
6	Conclusion and Outlook	85
A	Beam Field Distribution	87
B	Guided Waves in Rectangular Structures	91
C	Remarks on BPM Resolution	97
D	Electro Discharge Machining	99

Chapter 1

Introduction

Particle accelerators play a vital role in modern research. The fundamental constituents of matter and their interactions are studied with high energy colliders. Synchrotron light sources utilizing the radiation emitted by accelerated particles cover a wide range of applications from solid state physics, life sciences, medicine, to materials research.

The international TESLA¹ collaboration proposes the construction of a superconducting linear collider with an integrated X-ray Free Electron Laser (FEL) facility. The high quality of the electron beam delivered by the TESLA linac is well suited to drive a FEL based on the principle of Self Amplified Spontaneous Emission (SASE). To study the feasibility of the TESLA concept, the TESLA Test Facility (TTF) has been planned, set up, and is now in operation. This facility comprises not only an electron linear accelerator, but also the complete infrastructure for cavity treatment. In order to include the FEL option in an early stage, a SASE FEL for the VUV² wavelength regime is also integrated into the design and is now in the phase of commissioning.

Coherent light emission in a SASE FEL is achieved by the interaction between the density-modulated electron beam inside an undulator and the spontaneous undulator radiation.

The overlap between the photon field and the electron beam over the complete length of the undulator region is essential for the operation of the SASE FEL. To ensure this overlap several position-sensitive diagnostics devices are mandatory along the FEL beamline. In the present work, a new type of waveguide beam position monitor (BPM) has been developed providing high resolution position

¹TeV Energy Superconducting Linear Accelerator

²Vacuum Ultra Violet

measurements with negligible influence on the electron beam. The position of the electron beam is reconstructed by comparing signals induced into four waveguides arranged symmetrically around the beam pipe. Each waveguide couples to the electromagnetic field co-propagating with the electron beam by a small aperture in the beam pipe wall. Transduced signals are then transported through matching stages into the first element of a narrowband receiver tuned to 12 GHz.

Outline

The TTF FEL is introduced in chapter 2, together with a brief review of the SASE operation principle. The need for a high precision beam orbit observation and correction system is motivated by performance considerations of the SASE FEL. This chapter also includes a presentation of the electron beam diagnostics and the general strategy for the alignment of the electron beam is presented.

Chapter 3 deals with a more detailed analysis of the operation principle of the waveguide BPM derived from microwave principles. Beside that, numerical calculations and an analytical model are used to study the reactions of the BPM on the electron beam.

Measurements performed with prototypes of the waveguide BPM are presented in chapter 4. A testbench for laboratory measurements is described together with measurements of intrinsic monitor parameters. Tests and results obtained under beam conditions at the CLIC Test Facility 2 (CTF2) and at the S-Band Test Facility (SBTF) are reported.

Chapter 5 is devoted to calibration techniques. In addition to that, estimates concerning the resolution and accuracy of the waveguide BPM are presented.

This thesis closes with a summary and an outlook on future development issues of the waveguide BPM.

Chapter 2

TESLA Test Facility Free Electron Laser

In this chapter the TTF FEL is introduced together with a brief review of the SASE operation principle. Furthermore, the electron beam diagnostics components of the FEL undulator are presented together with a report of the beam based alignment procedure.

2.1 TESLA Test Facility

The SASE FEL proposed by the TESLA collaboration [1,2] and currently under commissioning is driven by the TTF linear accelerator [3]. The TTF linac is based on superconducting cavities made of Niobium working with an accelerating mode at $f = 1.3$ GHz. The complete facility not only includes a linear accelerator, but also the required infrastructure for cavity processing. The research and development effort is carried out within an international collaboration with the aim to build a linear collider with integrated X-ray laser facility [4].

In Fig. 2.1 the layout of the two phases of the TTF FEL project is illustrated. Electrons generated in a 4 MeV laser driven photoinjector, are captured by a superconducting nine-cell cavity providing an energy gain of 13 MeV. The electron bunches with the desired time structure are accelerated further in the first cryomodule by eight nine-cell cavities with an average gradient of more than 15 MV/m. Since FEL operation requires a short bunch length, the electron bunches have to pass a magnetic chicane which reduces the root-mean-square bunch length from 1 mm to 250 μm . Additional modules accelerate the elec-

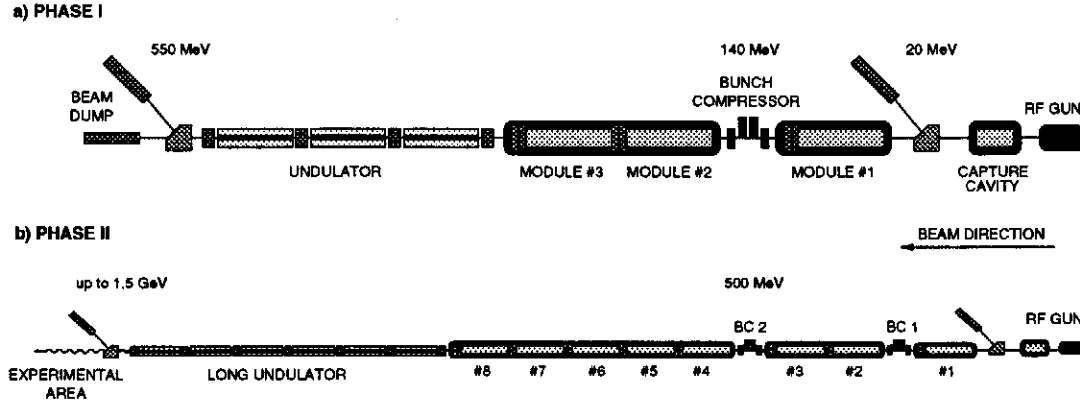


Figure 2.1: Development stages of the TTF FEL project.

tron bunches up to an energy of 500 MeV. In Tab. 2.1 design electron beam parameters of the TTF linac phase I are listed.

Beam energy	200 up to 500 MeV
Normalized emittance	2π mm mrad
Charge per bunch	0.1 up to 1.0 nC
RMS beam radius	$80 \mu\text{m}$
RMS bunch length	$250 \mu\text{m}$
Bunch repetition rate	1 MHz
Macropulse rep. rate	up to 10 Hz
Macropulse length	up to $800 \mu\text{s}$

Table 2.1: TTF FEL phase I in numbers [2].

In phase II of the TTF FEL project the linac will be equipped with additional cryomodules, a second magnetic chicane for further bunch compression, and a two times longer undulator. The electron energy delivered by the linac is then upgraded to $E = 1.5$ GeV and the root-mean-square bunch length is compressed by a factor of five to $50 \mu\text{m}$. The completion of a VUV FEL user facility is planned for the fall of 2001 [2].

2.2 SASE FEL at the TTF

The operation of the FEL at the TTF is based on the SASE principle [5]. In the SASE process the spontaneous undulator radiation is amplified in the single pass

of an electron beam through an undulator. Because no optical cavity is needed for the operation, wavelength from VUV to hard X-rays are in reach for such a device.

The wavelength of the radiation is tunable by varying the electron beam energy. In phase I of the TTF FEL project the radiation band will cover wavelength from 120 to 40 nm for electron beam energies between 230 and 390 MeV, while in phase II, with a beam energy of 1 GeV and a longer undulator, wavelengths down to 6.4 nm can be reached.

2.2.1 SASE FEL Process

The SASE FEL process is based on the interaction between the electron beam and the radiation field emitted by the electron itself [6, 7]. The key element of the SASE FEL is an undulator which forces the electrons to move along a curved periodical trajectory. The undulator of the TTF FEL is formed by a sequence of dipole magnets with opposite polarity and produces a transverse magnetic field forcing the electrons to move along sinusoidal trajectories. Because a transverse velocity component exists the longitudinal velocity component of the electrons changes periodically. In consequence the electrons emit radiation with wavelength λ_r and higher harmonics, called undulator radiation, which is sharply peaked and confined in cone with small opening angle in the longitudinal direction of the electron motion. The radiation field is a plane electromagnetic wave with only transverse field components and a wavelength much shorter than the undulator wavelength. Now this radiation field and the undulator field \vec{H}_U act in tandem on the electrons. Energy is exchanged due to the transverse component of the electron velocity $\beta_x = v_x/c$ with a rate

$$\dot{\gamma} = \frac{e(\beta_x \cdot E_x)}{m_e c}, \quad (2.1)$$

where e and m_e are the charge and mass of the electron, respectively; γ the relativistic factor of the electron, $E_x = E_o \sin(k_r z - \omega_r t)$ the horizontal field of the electromagnetic wave with k_r and ω_r are the wave number and frequency respectively; and c the speed of light in vacuum. Both, the electron beam and the wave are propagating in z -direction. To achieve effective energy exchange between the electron and the wave, the scalar product $(\beta_x \cdot E_x)$ should be maintained to be constant during the undulator passage. This is given, when the wave slips against the electron with the relative velocity $(c - v_z) = c(1 - \beta_z)$ by one wavelength per undulator period as illustrated in Fig. 2.2, where the longitudinal electron velocity is β_z . This synchronism condition can be written like

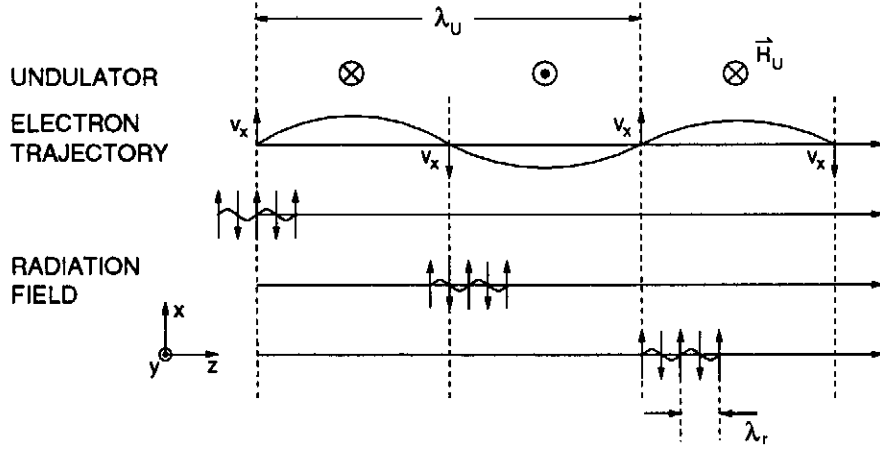


Figure 2.2: Illustration of the synchronism condition. The horizontal velocity component of the electron trajectory v_x is always continuously in phase with the radiation amplitude as experienced by the electron [8].

$$\beta_z = \frac{\omega_r/c}{k_r + k_U}, \quad (2.2)$$

i.e., the electron velocity equals the phase velocity of the ponderomotive wave, a wave with frequency ω_r but with a wavenumber $k_r + k_U$. The absolute value of the phase determines whether the electron gains or loses energy from the radiation field. This can be described in the longitudinal phase space of the electrons inside the undulator by two variables

$$\theta = (k_U + k_r)z - k_r ct \quad \text{and} \quad \eta = \frac{\gamma - \gamma_R}{\gamma_R} \quad (2.3)$$

where γ_R is the relativistic factor for the synchronized electron and θ describing the phase difference between the electron trajectory and the ponderomotive wave. The dynamics of the electrons in the ponderomotive potential of the undulator and radiation field is illustrated in Fig. 2.3. The separatrix region in Fig. 2.3a is the phase space surface which separates the bound and unbound motion. Any electron within the separatrix is trapped in the sinusoidal potential and oscillates around $\theta = 0$.

An analogous example is the motion of charged particles in the longitudinal phase space of the accelerating voltage in a RF cavity. Particles are either accelerated or decelerated depending on their phase with respect to the nominal phase.

Since the radiation field wavelength is much shorter than the electron bunch length, the initial phases of the electrons are almost uniformly distributed over 2π . Particles in the region $-\pi < \theta < 0$ gain energy from the radiation field

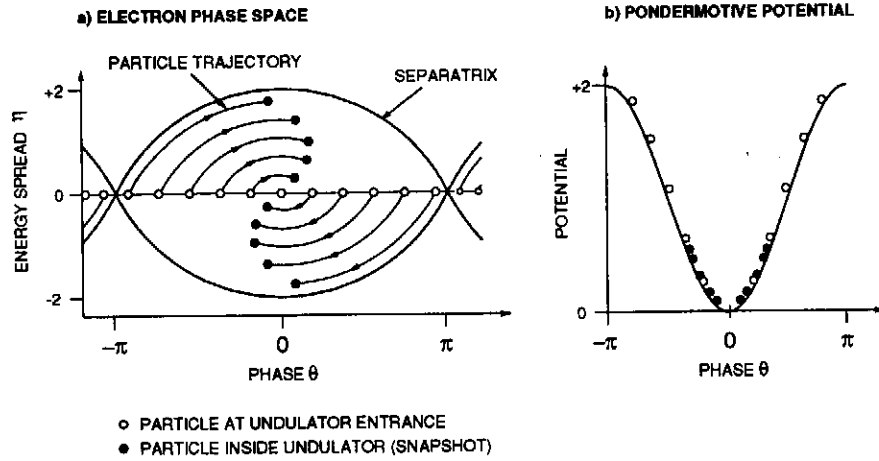


Figure 2.3: Longitudinal phase space representation of the electron motion in the radiation field potential. Injected particles are represented by empty circles, location of these particles after certain undulator length by filled circles.

while particles in $0 < \theta < +\pi$ are decelerated and loose energy to the field (see Fig. 2.3a). Electrons captured in the separatrix execute less than one oscillation in the ponderomotive potential during one pass through the undulator while performing hundreds of transverse oscillations. The amplitude of the radiation field depends on a number of FEL parameters including the period length and field strength of the undulator and the electron energy. The movement of the electrons in the potential well is illustrated in Fig. 2.3b. The energy released by the electrons increases the radiation field and consequently lowers the minimum further. Conversely, electrons moving away from the potential minimum up the potential well decrease the radiation field.

In consequence the electrons start to bunch at a certain radiation phase as illustrated in Fig. 2.4. For a bunched beam the radiation emitted is in phase and the total intensity can be strongly enhanced. The stronger radiation field pushes the electrons to bunch even faster and the coherent emission is enhanced even further. The change of the electron energy and the emission of coherent radiation is the source of a collective instability resulting in a collective bunching on a resonant frequency and a strong amplification of the radiation field. In the last picture of Fig. 2.4 this process is saturated, the electron beam is completely bunched and the field amplitude is at maximum. After this maximum the electrons start to debunch and the field amplitude decreases.

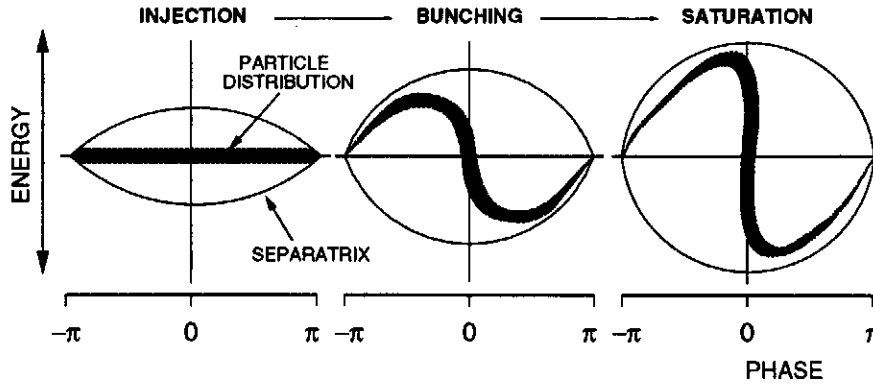


Figure 2.4: Longitudinal phase space representation of the bunching process in a high gain FEL amplifier.

2.2.2 Electron Beam Requirements

The SASE process imposes strong conditions on the quality of the electron beam delivered by the linac such as a small transverse emittance and a low energy spread. Essential for the operation is the overlap between the electron beam and the radiation field over the entire length of the undulator. If the electron trajectory deviates from the radiation field, an additional SASE field may be build up, while the output power of the former field would decrease. In consequence, the electron position has to be observed and corrected at several positions along the beamline. In Fig. 2.5 results from numerical calculations [9] are depicted for the decrease in output power caused by missing overlap. In order to keep the degradation due to missing overlap below 10%, the root-mean-square orbit deviation has to be kept under a level of $\Delta x_{rms} < 10 \mu\text{m}$ [10]. Thus electron beam position monitors with a resolution of a few μm and correctors together with electron beam alignment techniques are required to guarantee the operation of the SASE FEL at high power.

2.2.3 Undulator

The undulator is the most prominent FEL specific component. It provides the alternating magnetic field so that the FEL process can take place. In order to keep the transverse beam size small, the undulator has a superimposed quadrupole FODO¹ lattice [11]. The undulator is a planar hybrid type with soft iron pole

¹Each half cell of such a lattice period is composed of a focusing (F) and a defocusing (D) quadrupole with a drift space (O) in between.

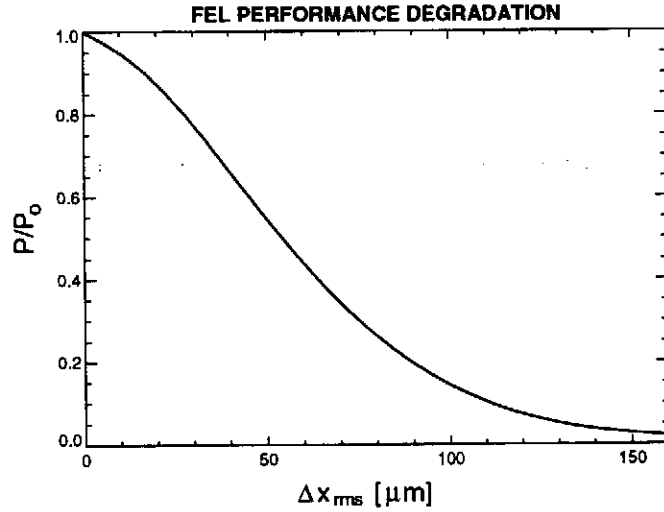


Figure 2.5: FEL output power close to saturation versus root-mean-square orbit deviation from a straight line. The output power is normalized to output power P_0 from a perfect aligned beam [9].

pieces in conjunction with permanent magnets. For the quadrupoles, the main magnets are retracted by 2 mm from the pole tips to get space for four additional focusing magnets per halfperiod. To simplify production and installation, the 15 m (30 m for phase II) long undulator is divided into 4.5 m long modules.

The complete undulator is illustrated in Fig 2.6. The entire setup consists of three modules separated by drift regions where diagnostic blocks and vacuum pumps are placed. In Tab. 2.2 undulator parameters are listed.

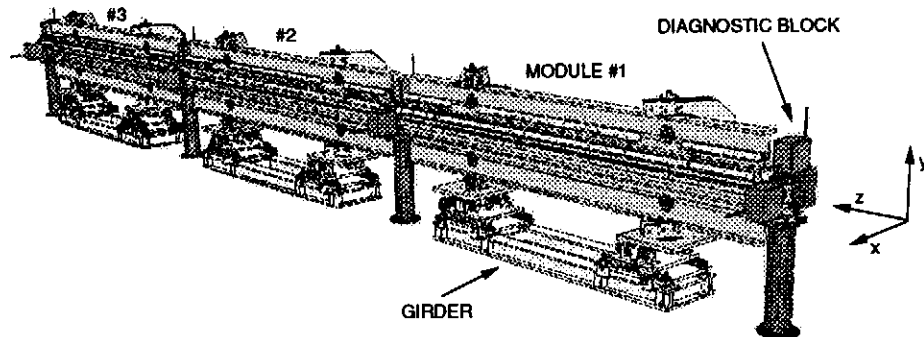


Figure 2.6: Three undulator modules with four diagnostic stations.

Complete length phase I	15 m
Complete length phase II	30 m
Module length	4.5 m
Inner chamber diameter	9.6 mm
Gap height	12 mm
Dipole period length	27.3 mm
Quadrupole gradient	12.5 T/m
Quadrupole length	136.5 mm
FODO period	955.5 mm

Table 2.2: TTF FEL undulators in numbers [2].

2.3 Electron Beam Diagnostics

In this section the general strategy is outlined for the alignment of the electron beam inside the undulator of the TTF FEL. In particular, position sensitive diagnostic devices in use and under development for this purpose are briefly described.

2.3.1 Strategy

Ten strong focusing quadrupoles are integrated per undulator module. Misalignments of these quadrupoles represent a source of beam trajectory distortions. Furthermore, orbit deviations are introduced by unknown, random dipole kicks, due to errors in the undulator structure.

Since the overlap between the electron beam and the radiation field determines the gain length and the spectral properties of the laser field, the beam has to be guided along a straight line through the entire undulator. The task of the diagnostic components and actuators is therefore to straighten the electron trajectory and to keep the root-mean-square deviation to this line within a limit of $\Delta x_{rms} = 10 \mu\text{m}$.

For the alignment of the electron beam along the undulator, different stages can be distinguished [12]:

Startup

At the beginning it is just needed to get the electron beam through the undulator. All BPMs can be used with a very rough calibration. The mean initial resolution,

determined by mechanical and electrical tolerances, of all components of a few hundred micro meter is sufficient for this. In order to protect the undulator against radiation, the steering will be done with a reduced bunch charge of $q = 0.1 \cdots 0.5$ nC. Beam loss monitors provide useful information on losses along the beamline during this stage.

Absolute Orbit Measurement at Fix Points

By using the wire scanners mounted together with the cavity monitors, the beam position can be fixed at the locations of the diagnostic blocks. The wire scanners define a reference axis through the entire undulator with an accuracy of better than $15 \mu\text{m}$. In a second step the cavity monitors can be calibrated with the wire scanners.

Beam Based Alignment

High resolution BPMs inside the undulator beam chamber are foreseen for relative orbit measurements at different energy levels. From dispersion measurements corrector settings may be calculated in order to keep the electron on a straight line.

2.3.2 Requirements for the Undulator BPM System

The requirements for a BPM system for the undulator gap of the TTF FEL can be summarized as following:

- Resolution around $100 \mu\text{m}$ for the startup phase and less than a few micro meter for the beam based alignment procedure.
- Compact size: the monitors must fit inside the undulator gap of 12 mm taking into account the inner beam pipe diameter of 9.6 mm.
- Must be compatible with the vacuum chamber built in one piece.
- The monitor stations should not waste too much of the total impedance budget.
- The monitor must operate in a high radiation environment with a beam of $0.1 \cdots 1.0$ nC (FEL operation) up to 8 nC (TTF linac operation) bunch charge and short bunch length.

2.3.3 Components

The backbone of the electron beam diagnostics at the TTF FEL is the wire scanner system. With four wire scanners equidistantly positioned along the beamline, the system provides high accuracy position measurements and spans out a reference axis for all further procedures. One drawback of the wire scanners is the fact that they disturb the electron beam. In consequence, these devices will only be used infrequently to calibrate the cavity monitors, which yield high resolution non-destructive beam position measurements.

In order to keep the electron trajectory straight inside the undulator one BPM and a corrector is required per FODO quadrupole magnet. In total, ten beam position monitors together with five horizontal and five vertical steerers are installed per undulator module. Two kinds of BPMs exist: Pickup-type BPMs were build for the first two undulator modules while the last module is equipped with a new waveguide-type BPM.

In addition, it is planned to supply a beam trajectory monitor for imaging a higher harmonic spontaneous undulator radiation.

Wire Scanner

Wire scanners for absolute beam position measurements were installed inside each diagnostic block within the undulator beamline [13]. These scanners are mounted horizontally and vertically to the diagnostic blocks, which also host the cavity monitors. The working principle is illustrated in Fig. 2.7. A carbon or tungsten wire with diameter small compared to the transverse bunch size is moved by a precision DC motor through the beam profile. As the electron bunch traverses the wire, bremsstrahlung photons are produced, while the scattered electrons will in many cases hit the inner beam pipe surface and create a shower. The bremsstrahlung photons emitted with small opening angle are detected some meters downstream by a lead glass detector. The intensity of the shower from the scattered electrons can be detected by a plastic scintillator paddle plus photomultiplier readout close to the diagnostic block in front of the downstream undulator module. If this signal plotted versus the wire position, beam position relevant information can be obtained. Another technique relies on secondary emission of wire material. The current in the wire, as a result of this process, can be measured versus the wire position. It is expected that the resolution of the wire scanner beam position measurement is in the order of $1\text{ }\mu\text{m}$ [14]. The wire scanners will be further used to calibrate the cavity-type BPMs, which are located inside the diagnostic block, too.

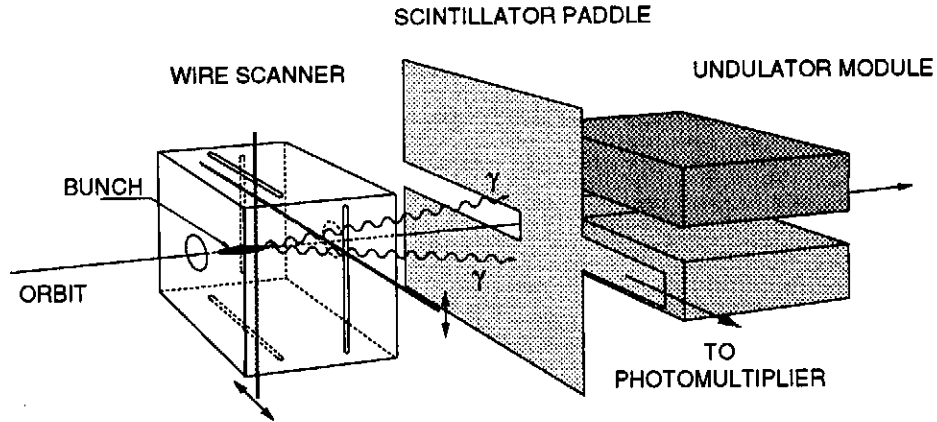


Figure 2.7: One wire scanner assembly with scintillator paddle to detect photons from shower electrons.

Cavity Type Monitor

Circular cavities excited in the first dipole mode by an off-axis beam (see Fig. 2.8) were chosen for the diagnostic stations because of the desired resolution of a about $5 \mu\text{m}$ and the available transverse space [15].

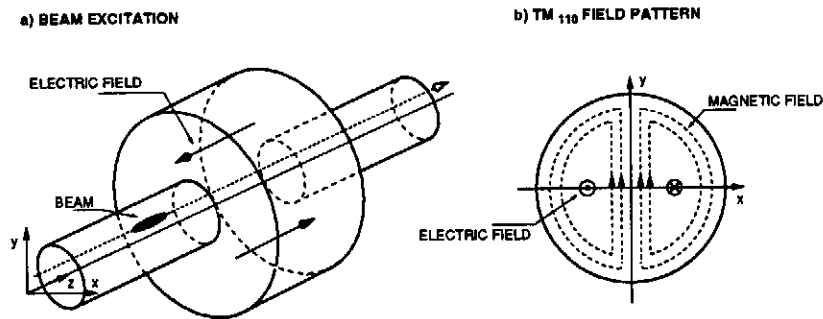


Figure 2.8: a) Beam excited TM_{110} -mode in a circular cavity. b) Field pattern of the horizontal polarization.

In resonant cavities the beam excites special field configurations resonating at defined frequencies. An electron beam moving on or parallel to the longitudinal beam axis excites Transverse Magnetic (TM)-modes in the cavity. The amplitudes of these modes depend on the cavity geometry, the bunch charge, the beam position, and the bunch spectrum [16]. Dipole modes TM_{110} (see Fig. 2.8) are used for position detection, since their amplitudes depend in first order linearly on the beam position and is zero for a beam in the electrical center of the cavity. The signals excited in the cavity are out-coupled by probe or loop antennae,

or by apertures in the cavity wall. These coupling ports span out a reference frame in which the beam position is measured. In Fig. 2.9b a cavity-type monitor with two opposite slot-waveguide pairs is depicted. For the detection of

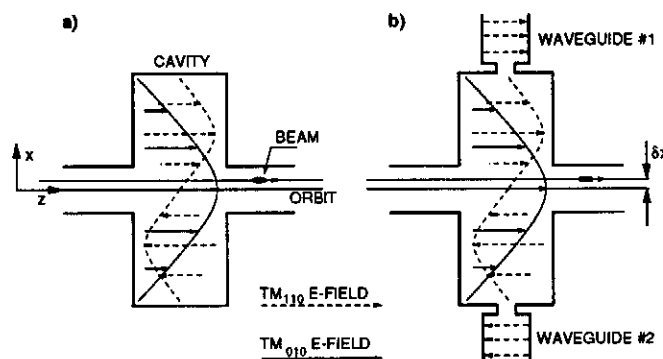


Figure 2.9: a) Excitation of the TM_{010} and the TM_{110} by an offset beam. b) Aperture coupling to the magnetic field with two waveguides.

both polarizations of the dipole mode, four slots have to be integrated into the cavity, or two cavities with two slots in each may be used. For the cavity-type BPMs inside the diagnostic stations, a solution with two cavities with a dipole mode at $f_{110} = 12$ GHz was favored. The choice of this frequency was driven by commercially available electronics components and by the fact, that the position resolution of a cavity-type BPM improves with f_{110} increasing [17]. By using two cavities separated in beam direction the isolation between the two polarizations of the dipole mode is significantly improved. The zero detection capability of a cavity-type BPM is limited because of the presence of the dominant TM_{010} common mode, which is excited by an on or off axis beam. In any case, because of the high sensitivity resonant monitors offer, they are the device of choice for high resolution position measurements. Calibrated with wire scanners, the cavity-type BPMs become also a high accuracy position measurement device.

Beam Trajectory Monitor

Behind the last undulator module it is planned to install a beam trajectory monitor (BTM) [18] to reconstruct the electron beam trajectory at several points inside the last undulator module. The setup for the BTM consists of a set of pinholes and a high resolution silicon position sensor. The operation principle is illustrated in Fig. 2.10. Electrons traversing the undulator emit synchrotron radiation. This radiation is imaged through small pinholes, one for the horizontal and one for the vertical direction, on an array of silicon pixel detectors with two

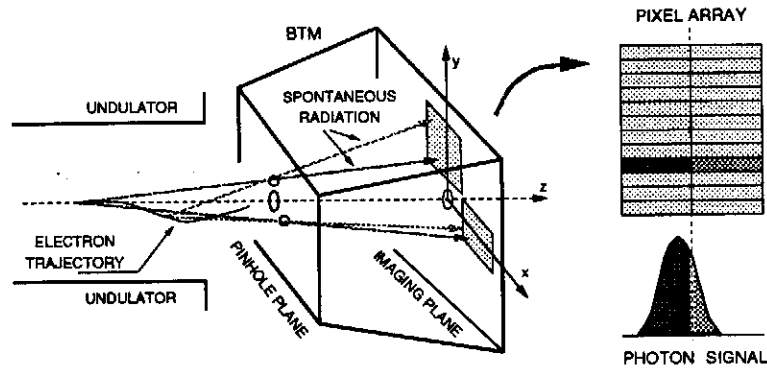


Figure 2.10: Operation principle of the beam trajectory monitor with a pinhole-type camera and position sensitive silicon pixel detectors.

columns of 12 pixels each. One passing bunch results thus in a streak onto the pixel array. The streak image for an offset beam is an angle, while that from a centered beam is parallel with respect to the pinhole axis. Thus, an image is created from the horizontal and vertical projections of the electron trajectory on a plane normal to the beam axis. At present, the silicon pixel detector has been successfully tested with a diode laser [19].

Problematic for the operation of the BTM is the high radiation environment of the accelerator. Electrons from dark current as well as mis-steered beams can lead to severe damage of the silicon detector.

Pickup Beam Position Monitor

The first and second undulator modules of the TTF FEL are each equipped with ten broadband electrostatic pickup BPMs [15]. These BPMs are designed to be in operation primarily in phase I of the TTF FEL project. Fig. 2.11 shows the cross-section of one plane of the electro-static pickup BPM. Each electrode

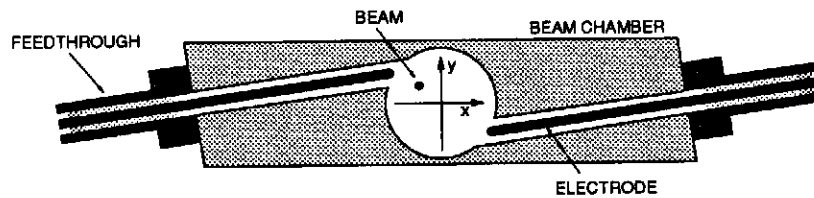


Figure 2.11: Cross-section of one detection plane of the electrostatic pickup.

consists of an open $50\ \Omega$ coaxial line. The extended vacuum feedthrough couples

to the electromagnetic field of the electron beam. The amplitude of the beam induced pulse signal depends on the bunch charge and the transverse beam position in terms of the beam-to-electrode distance. Four symmetrically arranged electrodes are needed to achieve a linear and beam intensity independent position measurement. Due to the size of the electrodes the arrangement for one BPM was split into two symmetric pairs, separated by $3/2$ of the undulator wavelength. Each pair consists of two opposing electrodes rotated by $\pm 30^\circ$ with respect to the horizontal plane. The vacuum feedthroughs used are commercially available SMA type from KAMAN Corporation with modifications of the center pin and flange-mounting. Each pin-end is spherical to reduce the local electric field strength preventing possible sparks by very short bunches. The pulsed signals are transferred via cables to the read-out electronics, where signals are processed by a squew difference over sum technique [20]. The beam-to-electrode transfer characteristics were measured using frequency domain S_{21} measurements. These measurements show the expected high-pass characteristics with a roll-off frequency of 4 GHz.

For the $\sigma_z = 250 \mu\text{m}$ long bunches of phase I of the TTF FEL project the pickup BPMs are believed to be safe and reliable. For shorter bunches, as envisaged in phase II with $\sigma_z = 50 \mu\text{m}$, these monitors may cause problems to the vacuum system, since the high electric potential difference between the chamber and the pickup might cause sparks, which would destroy the electrode.

Waveguide Beam Position Monitor

In the vacuum chamber of the third undulator module a new type of BPM has been installed and is presently in the testing stage. In contrast to the electrostatic pickups it uses coupling slots between the beam region and a waveguide to measure the electron beam position. Fig. 2.12 shows schematically one waveguide BPM with its four waveguides. A fractional part of the electromagnetic beam field is out-coupled by four slots arranged symmetrically around the beam pipe. Special ridge waveguides were designed to reduce their size and optimize the coupling. Each waveguide pair (S1/S3 and S4/S2 resp. in Fig. 2.12) is positioned at $\pm 34^\circ$ with respect to the horizontal axis. The cut-off frequency of the waveguide is at 8.99 GHz and the working frequency for the first read-out electronics element is $f_w = 12 \text{ GHz}$ being identical with that of the cavity monitors in the diagnostic blocks. At the end of each waveguide, a coaxial adapter with a vacuum feedthrough is flange-mounted to the beam chamber.

The waveguide BPM has large potential for its use in phase II of the TTF FEL

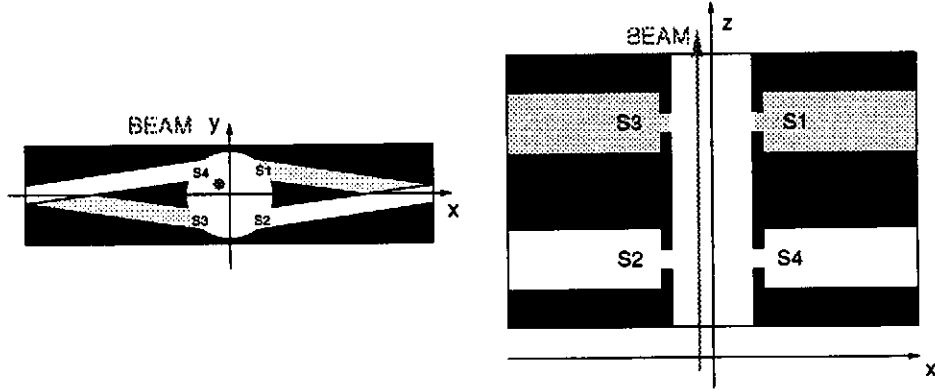


Figure 2.12: Schematics of one BPM head with four waveguides and four coupling slots (profile and top view).

project, when the bunch length will be reduced to $\sigma_z = 50 \mu\text{m}$. Tests under beam conditions as well as measurements in laboratory have proven the capability of this monitor type.

The detailed description of this new type of BPM, its operation principle, a discussion of experimental results obtained so far, and the development of a calibration scheme are the main objectives of this thesis.

Chapter 3

Microwave Characterization

Since the operation of the waveguide BPM is related to microwave concepts, a precise characterization of its microwave behavior is necessary to describe and optimize the system performance [21]. Analytical calculations and numerical simulations are presented for the coupling into the ridged waveguide as well as for the design of the matching transition. Finally, interactions with the electron beam in terms of wake fields are estimated by numerical simulations and by an analytical model.

3.1 Overview

One BPM unit consists of four four slot-waveguide pairs, which are spread uniformly around the beam chamber. Due to the vertical space limit of the undulator gap, these four elements are split into two groups in beam direction.

In Fig. 3.1 the basic constituents of one BPM channel are shown. A beam position related signal is coupled via a small aperture in the beam pipe into a waveguide. In order to match the impedance of the waveguide to a $50\ \Omega$ coaxial system, a matching section is necessary. A ultra-high vacuum feedthrough serves as connection to the outer world.

For the design, the whole structure was divided into two parts: The one which determines the coupling to the beam - and, hence, the induced signal strength - and the matching section to the $50\ \Omega$ vacuum feedthrough. Technological aspects were taken into account in all design steps.

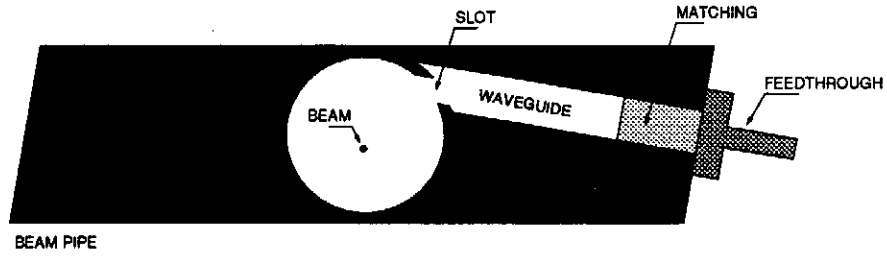


Figure 3.1: Schematic structure of one BPM channel.

3.2 Waveguide Design

Together with the slot, the shape and position of the waveguide behind the slot determines the induced signal amplitude. The operation frequency of the waveguide also fixes the working frequency of the first element of the signal processing electronics.

The aim of the waveguide design was to conceive an appropriate guiding of the waveguide fields to be parallel to the beam magnetic field. The connection port between waveguide and beam field is the coupling slot. The field pattern filling this aperture is a boundary condition for the orientation of the field lines in the waveguide at the location of the coupling aperture.

Since the electric field lines point transversely on the aperture, a coupling to the magnetic field lines, which run in parallel with the pipe circumference, was intended. For the waveguide design the coupling slot of the BPM can be regarded as a radiating magnetic dipole oriented parallel to the magnetic field lines of the beam co-propagating field.

To enable a sufficient coupling to the magnetic field inside the waveguide, the waveguide fields must be guided in a way that it has maximum overlap with the dipole field. Furthermore the waveguide structure must fit into the vacuum chamber, whereas some space around the waveguide is reserved for vacuum seals. The operation frequency of the waveguide f_w is in principle only limited by the cutoff frequency of the beam pipe treating it like a circular waveguide with $f_{pipe} = 17.94$ GHz (according to Eq. B.13). For $f_w \geq f_{pipe}$, fields generated by the interaction between the electron beam and its surroundings can couple into the waveguide and lead to interferences with the signal from an offset beam. The working frequency regime was determined to X-band ($8.2 \cdots 12.5$ GHz), because of commercially available signal processing components like filters, amplifiers, and mixers from satellite technology. In Fig. 3.3 the evolution history from standard a X-band waveguide to the T-ridge waveguide is illustrated. To enhance

field overlap between beam and waveguide magnetic field, a ridge with a T-bar is shaped out of the ridge end. With this procedure, the outer waveguide dimensions are reduced while keeping the working frequency constant. The dimensions of the T-ridge waveguide and slot are optimized for a coupling to the beam field of about 1% and for small size in order to fit inside the vacuum chamber. Because the working frequency of the waveguide is set to 12 GHz, the cutoff frequency of the fundamental mode should be around $8 \dots 9$ GHz, because waveguides are used for a frequency range of $1.2 \cdot f_c \leq f_w \leq 1.8 \cdot f_c$ where attenuation in the dominant mode is at minimum [22]. The cutoff frequency of the next higher mode should be well above the working frequency to avoid interferences.

By MAFIA¹ [24] 2D simulations the first two cutoff frequencies have been estimated to 8.99 GHz for the fundamental and 13.24 GHz for the next higher mode. In Fig. 3.2 field patterns for these modes as well as the waveguide dimensions are illustrated. The waveguide structure can be fabricated using Electrical (or electro) Discharge Machining (EDM) (see Appendix D for details). Fig. 3.4 shows the second prototype after the EDM process.

¹MAFIA is an interactive program package for the computation of electromagnetic field problems in user-defined geometries. The program is modular; divided in preprocessor, post-processor, and problem specific modules for different cases of the Maxwell equations. Solving modules exist for problems like static electromagnetic fields, solutions in time- or frequency-domain, and wake fields [23].

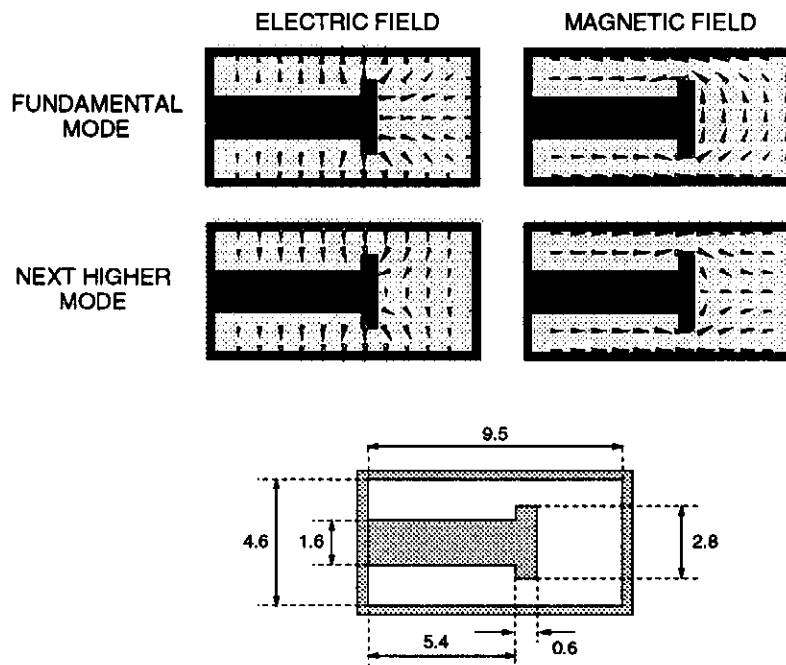


Figure 3.2: Field patterns for the first two modes of the T-ridge waveguide. The arrows indicate the direction of the electric and magnetic field at the center location of each arrow. In the bottom part of the figure the waveguide dimensions are given. All sizes are in units of [mm].

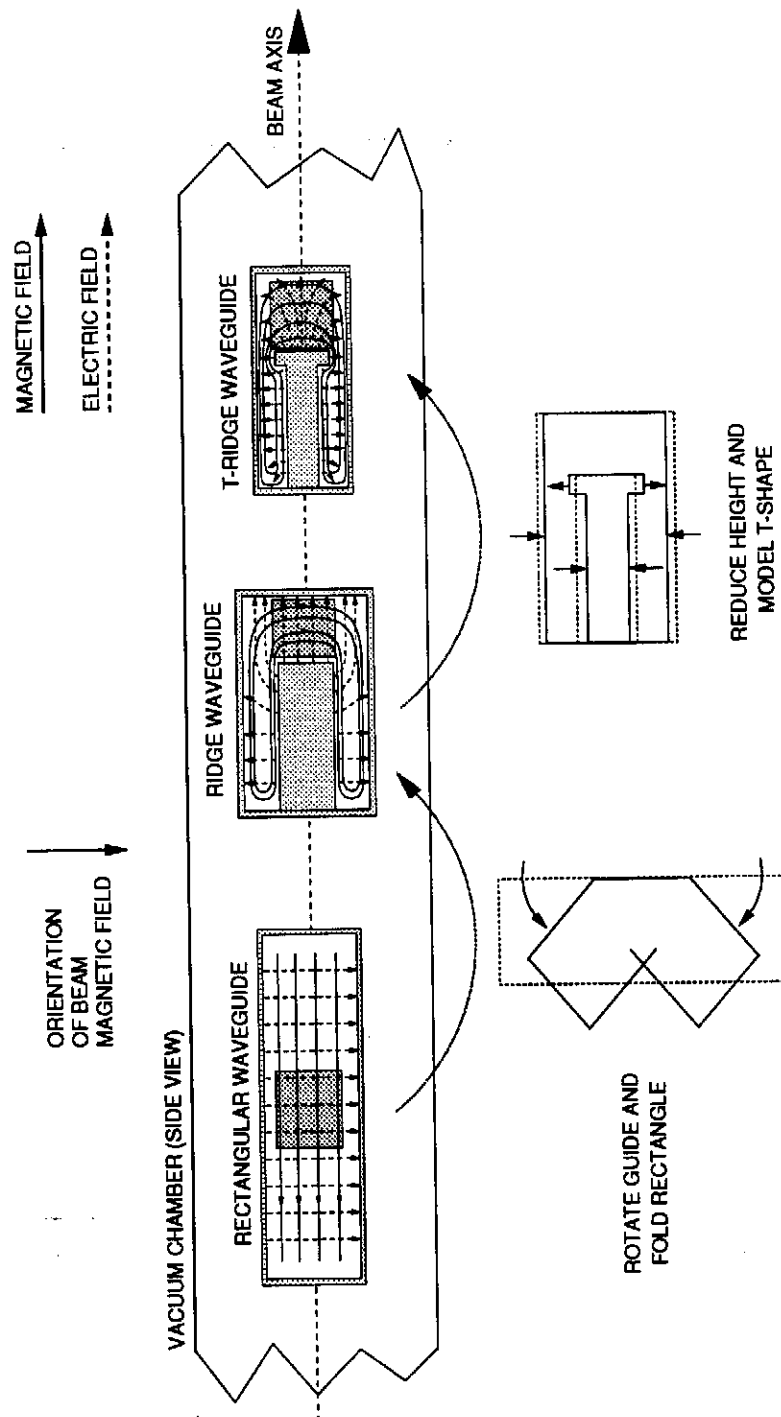


Figure 3.3: Evolution history of the T-ridge waveguide starting with a rectangular waveguide. Also the field pattern of the fundamental mode is sketched. The dark grey rectangle shows possible locations for the coupling slot enabling the coupling to the beam field.

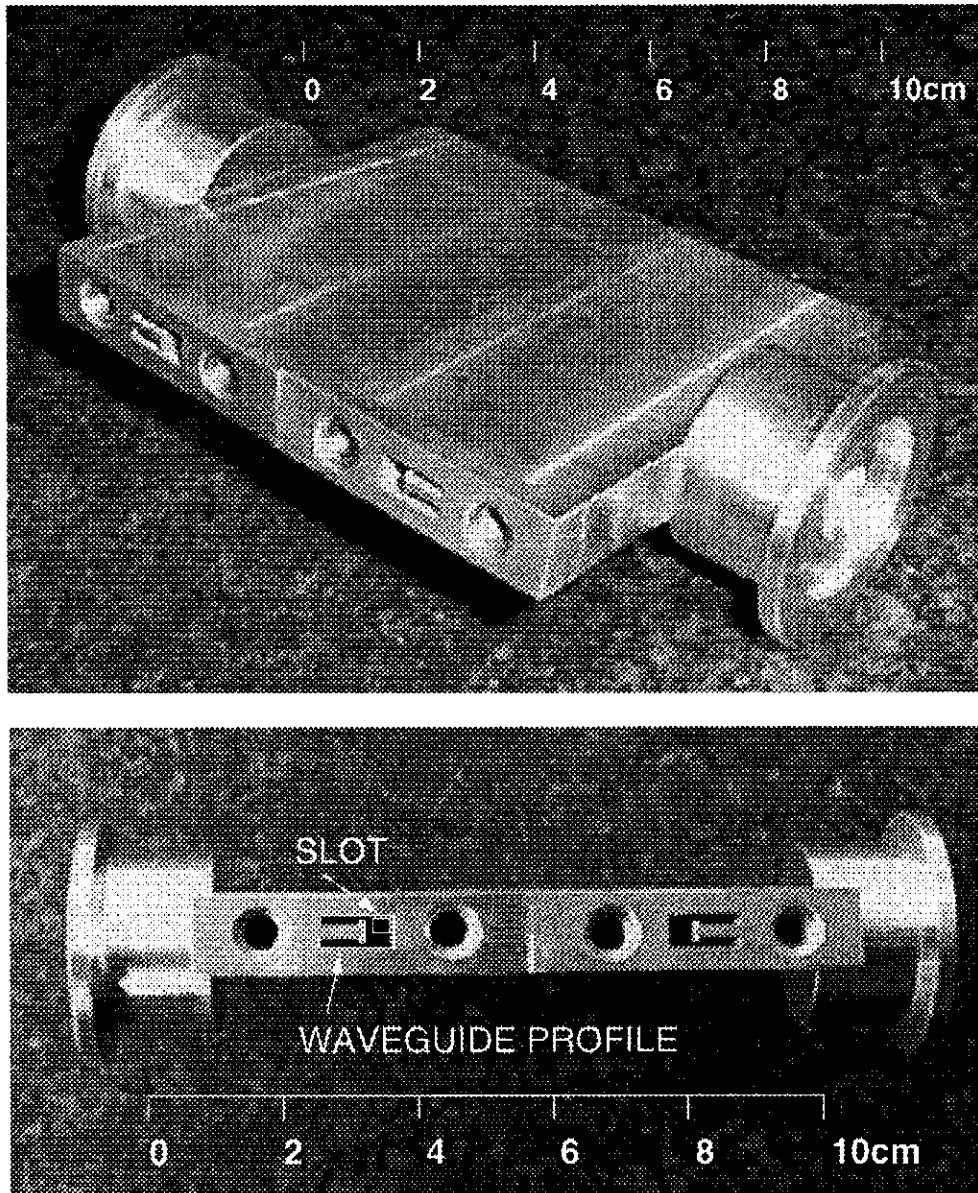


Figure 3.4: Photo of Prototype II. Top: Total view, bottom: view onto sidefront with two waveguide ports and round screwholes for mounting the vacuum feedthroughs.

3.3 Slot Coupling

Electromagnetic power transfer between two regions containing electromagnetic waves can be realized by different coupling methods, as there are

- probe antenna to couple capacitively to the electric field,
- loop antenna to extract inductively energy via the magnetic field, or
- aperture coupling for both fields.

Connections between coaxial transmission lines and waveguides are usually realized by the first two methods or by combinations of both. Waveguides are often coupled by small apertures of defined geometry in the common wall.

In case of the waveguide BPM, the waveguide is coupled by a small aperture to the beam region.

3.3.1 Introduction to the Problem

An aperture in a common wall between two waveguides can be regarded as a source of energy fed by fields on the incident side of the wall. With hole dimensions small compared to the wavelength of the regarded fields, it is possible to approximate the source by its lowest multipole moments. In most cases electric and magnetic dipole moments are sufficient. These moments can often be calculated from static fields [25].

To evaluate the coupling impedance analytically it is necessary to calculate the fields induced in a vacuum chamber for a given current distribution. First, one finds the fields produced by the current distribution without the slot (see Fig. 3.5a). Then, these fields are considered as an electromagnetic wave on the slot. In the next step it is obvious to find the fields diffracted by the slot into the waveguide (see Fig. 3.5b). These diffracted fields bear a resemblance with fields radiated by equivalent electric or magnetic dipoles, whose moments are proportional to the normal electric field and the tangential magnetic field of the incident wave (see Fig. 3.5c). The field radiated by this source into the two regions, together with the incident field and the scattered field represent a solution to the coupling problem. After comparing these fields one obtains the coupling impedance.

This approach, originally developed by Bethe [25] lacks in form of power conservation, since it relates the dipole moment only to the field of incident wave on the

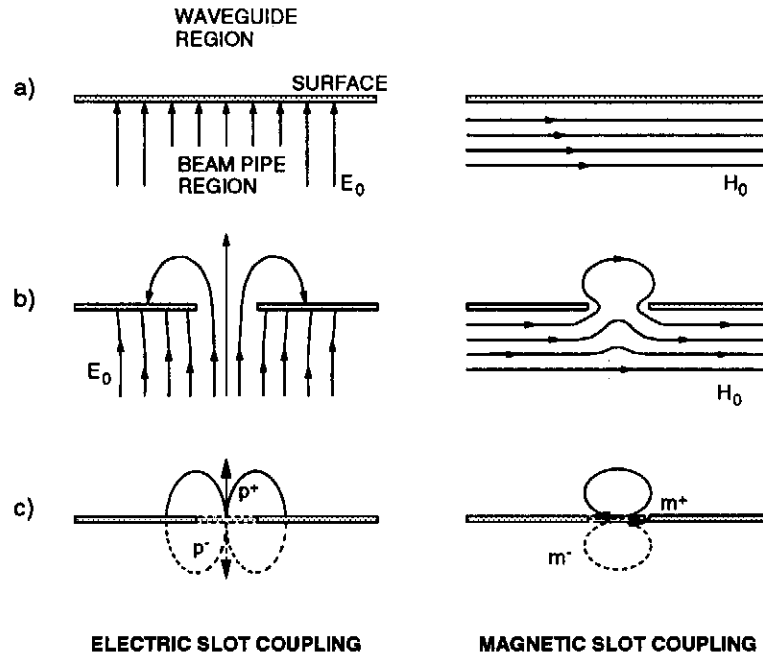


Figure 3.5: Route to compute an analytical expression for electrical and magnetic slot coupling.

aperture. Collin [26] modified Bethe's theory such that power conservation holds by introducing radiation reaction fields. By following this procedure allows one to use the static polarizabilities. The radiation reaction fields are the dominant mode fields produced by the magnetic and electric dipoles on both sides of the aperture evaluated at its center.

3.3.2 Coupling between Beam Field and Rectangular Waveguide

To illustrate the modified Bethe theory and to obtain simple scaling laws for the dependence of the coupling amplitude on the slot parameters a simple structure, where a rectangular waveguide is positioned with its longitudinal axis normal to a cylindrical beam pipe surface (see Fig. 3.6a) was investigated [27]. If a beam current I_b is moving in a circular, conducting beam pipe, then there is an electromagnetic field accompanying the beam. In the limit of a relativistic beam the field inside the beam pipe looks like a transverse-electric-magnetic (TEM) wave propagating down the beam pipe at the beam velocity. For a beam current I_b in the center of a circular beam pipe of radius b , the azimuthal magnetic field

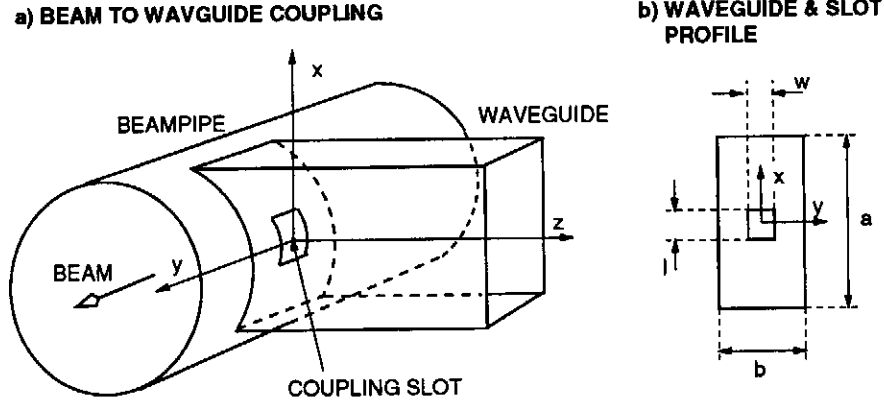


Figure 3.6: Geometry used for analytical calculations of the coupling impedance between a beam pipe and a rectangular waveguide. The waveguide is connected to the beam pipe with a small rectangular slot.

at the chamber surface is (see Appendix A for details):

$$H_o = \frac{I_b}{2\pi R}. \quad (3.1)$$

where R describes the beam pipe radius. The electric field E_o is connected to the magnetic field H_o according to $E_o = Z_o H_o$. The fundamental TE_{10} mode in the waveguide has transverse field components (see Appendix B)

$$H_x = \sqrt{\frac{4P}{ab}} \sqrt{\frac{k_z}{\omega\mu}} \cos\left(\frac{\pi}{a}x\right) \exp(-i(kz - \omega t)) \quad (3.2)$$

$$E_y = \sqrt{\frac{4P}{ab}} \sqrt{\frac{\omega\mu}{k_z}} \cos\left(\frac{\pi}{a}x\right) \exp(-i(kz - \omega t)) \quad (3.3)$$

for a wave propagating in z -direction in a reference frame with its origin in the aperture center as illustrated in Fig. 3.6b. The electric field inside the beam pipe is tangent to the beam pipe surface while the field of the TE_{10} mode inside the waveguide is parallel. Consequently E_o is perpendicular to E_x and can not couple. The magnetic field components in both regions H_o and H_y are parallel. Hence the two regions can only exchange energy via the magnetic field.

The magnetic field on the beam pipe wall will induce a magnetic current and a magnetic charge on the surface if the aperture is replaced by a magnetic wall. These sources produce a scattered field that can be expressed as the fields radiated by the dipole moments of the source distribution. In the first step the scattered fields may be expanded in terms of normal modal functions of the waveguide. In this case only the first order, the fundamental mode, has to be

taken into account, if the scattered field is only evaluated at the aperture center A . The scattered field H_s reads thus

$$H_s = c_{10} \cdot h_x \quad (3.4)$$

where h_x is the normalized magnetic field of the fundamental mode at the aperture center and c_{10} the expansion coefficient. The normalization $P = 1$ is necessary, because the amplitude of the scattered field is already given by c_{10} . It is thus the modal function of the fundamental waveguide mode

$$h_x = H_{xo} = \sqrt{\frac{4}{ab}} \sqrt{\frac{k_z}{\omega\mu}}. \quad (3.5)$$

The expansion coefficient c_{10} of the fundamental mode can be calculated according to [26]. For a small aperture, and with only magnetic fields involved, c_{10} represents the coupling to a magnetic dipole and a magnetic quadrupole. The quadrupole term can be neglected, since it represents a small quantity depending on the fourth power of the aperture dimension. It turns out, that c_{10} is proportional to the magnetic dipole moment M_x times the modal function h_x of the waveguide mode

$$c_{10} = \frac{i\omega\mu}{2} h_x \cdot M_x \quad (3.6)$$

The scattered field is the field of the propagating mode of the waveguide. Combining Eq. 3.4 and Eq. 3.6 leads to an expression for the magnetic field inside the waveguide excited by the magnetic dipole

$$H_{xo} = \frac{i\omega\mu}{2} h_x^2 M_x \quad (3.7)$$

The magnetic dipole moment M_x parallel to the incident field H_o and the waveguide field H_{xo} can be expressed according to Collin's modification of Bethe's theory. For the sake of power conservation the scattered field has to be added to the incident field giving

$$M_x = \alpha_m (H_o - H_{xo}) \quad (3.8)$$

at the aperture. The magnetic polarizability α_m depends on the aperture size and geometry. From Eq. 3.7 and Eq. 3.8 the magnitude of the magnetic field ratio can be derived to

$$\left| \frac{H_{xo}}{H_o} \right| = \frac{2\alpha_m \frac{k_z}{ab}}{\sqrt{1 + \left(2\alpha_m \frac{k_z}{ab} \right)^2}}. \quad (3.9)$$

To find the electric field ratio observe that in the beam pipe region the electric field is $E_o = Z_o H_o$ while in the waveguide $E_y = Z_F H_x$, where Z_F is the modal impedance of the TM_{10} mode. The effect of the coupling aperture thickness is included with the thick wall polarizability [28]. The thick wall polarizability is obtained from the normal polarizability multiplying by an exponential factor proportional to the wall width T that models the attenuation effect on the field transmitted through the aperture under cutoff. For an incident magnetic field normal to the aperture length the polarizability is

$$\tilde{\alpha}_m = 0.67 \cdot \alpha_m \exp\left(-\frac{\pi T}{w}\right). \quad (3.10)$$

This value $\tilde{\alpha}_m$ replaces α_m in Eq. 3.9. The normal magnetic polarizability of a rectangular slot is $\alpha_m = (\pi/16)lw^2$ [29]. If one expands the right-hand-term for the field ratio Eq. 3.9 in a series keeping the waveguide dimensions constant and with taking only the first order into account the field ratio is linearly proportional to $\tilde{\alpha}_m$.

For a configuration of a standard X-band waveguide ($a = 2b = 22$ mm) coupled to a beam pipe by a small slot ($l = w = 4$ mm) in a thin pipe wall ($T = 0.5$ mm) the analytical result was compared with results from numerical simulation with MAFIA. In Fig. 3.7 the field ratio according to Eq. 3.9 is plot-

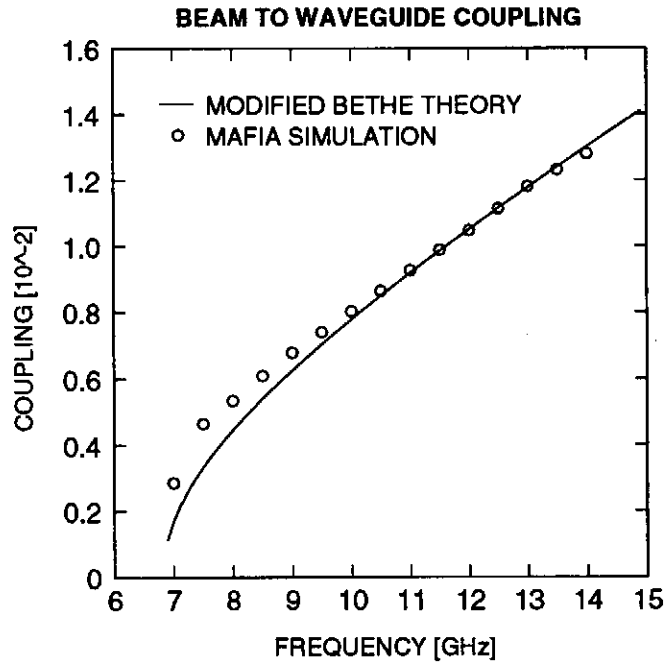


Figure 3.7: Coupling amplitude (or magnetic field ratio) according to Eq. 3.9. For comparison MAFIA simulated points are also plotted.

ted together with MAFIA results for frequencies above the cutoff of the X-band waveguide fundamental mode. The deviation between MAFIA simulation and analytical computation is less than 5% for frequencies close to cutoff and less than 1% for frequencies around 12 GHz. For the analytical formulation, only the magnetic coupling was taken into account, neglecting the effect caused by the electric coupling. In MAFIA, the coupling is determined with both types of fields. In the usable frequency range of the waveguide fundamental mode (11...13 GHz), the modified Bethe theory is an adequate description for the coupling between a rectangular waveguide and the beam induced field.

3.3.3 Simulation of the BPM Coupling

Because an analytical description for the field distribution of the BPM waveguide was not available, parameter studies were performed with MAFIA. Since the coupling parameter is the ratio of the waveguide field to the beam field, power transmission can be studied in terms of Scattering parameters (for example [30]). Scattering parameters (or S-parameters) are the reflection and transmission coefficients between incident and reflected waves of a microwave network. The S_{21} parameter relates the amplitude of the incident wave at the input port with the scattered wave at the output port. Adopted for one BPM channel S_{21} is equal to the coupling parameter. Fig. 3.8 shows the MAFIA preprocessor material distribution for a model BPM with two slot-waveguide combinations. The electromagnetic field distribution of an electron beam was simulated by a thin cylindrical conductor placed inside the BPM chamber forming a coaxial system together with the inner beam pipe surface serving as TEM input port. Into this setup a TEM wave was launched and S_{21} -parameters were calculated over

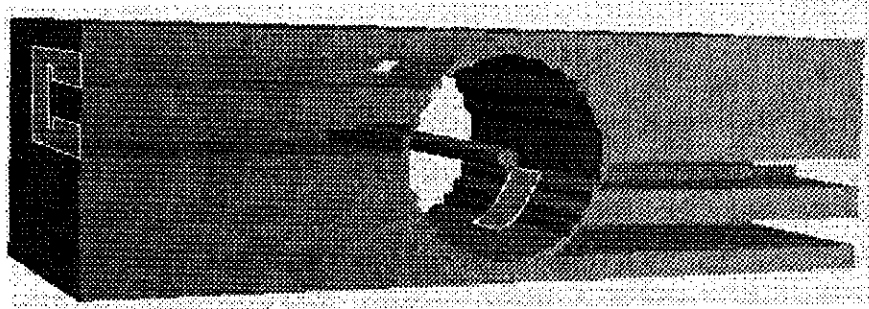


Figure 3.8: Material distribution used for MAFIA simulations. Modelled are two slot-waveguide combinations as well as a cylindrical inner conductor. Highlighted are the profile of the waveguide and one coupling aperture in the beam pipe.

a broad band around $f_w = 12$ GHz. Fig. 3.9 shows a result for the transmission parameter S_{21} as a function of frequency of the incident field reflecting the high-pass characteristics of the waveguide. The transmission at f_w is 0.01, thus the amplitude of the mode inside the waveguide is 1% of the amplitude of the beam accompanying field, or in logarithmic scale -40 dB.

The analytical calculation presented in the previous section delivered some scaling laws for the coupling amplitude k_s , depending in first order linearly on the

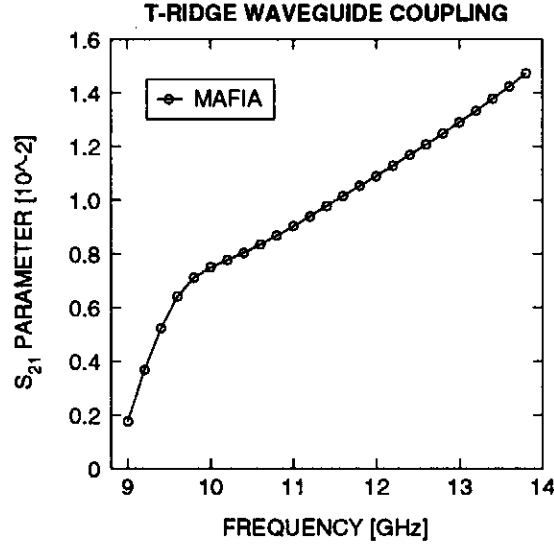


Figure 3.9: MAFIA result for the computation of S_{21} -parameter for frequencies above the cutoff frequency of the waveguide at 8.99 GHz.

polarizability of the aperture:

$$k_s \propto \tilde{\alpha}_m = 0.13 \cdot lw^2 \exp\left(\frac{\pi}{w}T\right) \quad (3.11)$$

To check this the dependencies on slot length l , width w , and depth T MAFIA simulations were performed. In Fig. 3.10 results from this simulations are gathered. The dependency of the slot length l can be modelled linearly reflecting the expectation from the analytical model. The behavior of the coupling amplitude regarding the slot width w is more complex. It turned out, that the coupling amplitude rises quadratically with strong damping caused by the exponential term in Eq. 3.11. As expected the effect of the coupling slot depth T can be described with the effect of waveguide damping below cutoff.

Furthermore mechanical tolerances were derived with these simulations. To keep the root-mean-square spread of the coupling amplitude among all channels under a level of 2% the tolerances are for slot width and height $\pm 50 \mu\text{m}$ and for the slot depth $\pm 100 \mu\text{m}$.

In addition to the slot parameters, the effect of varying waveguide dimensions were also studied with MAFIA simulations. In Fig. 3.11 results from this simulations are illustrated. Both effects can be modelled linearly in a small region around the design values. The impact of the waveguide height is stronger, because the effect on the cutoff frequency is dominant compared to the effect of the waveguide width.

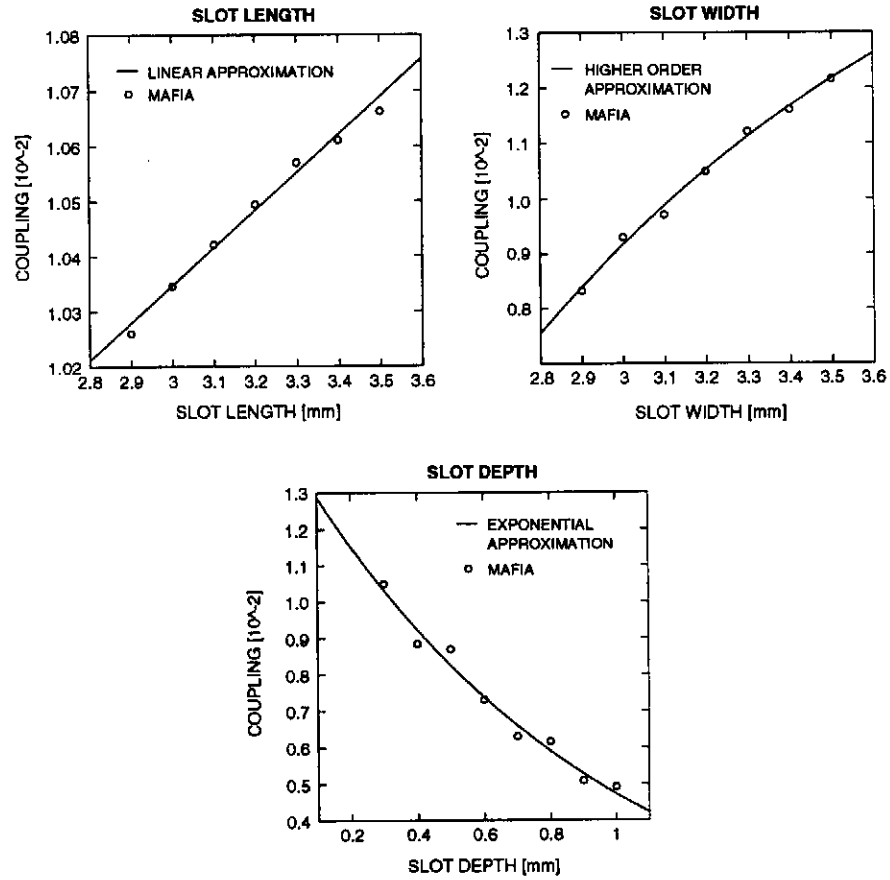


Figure 3.10: Evaluation of the coupling amplitude depending on slot width, length, and depth. Design values are 3.2 mm for slot width and length, and 0.3 mm for the slot depth. The points in each graph represent results from MAFIA simulations, the curves indicate approximations based on the results from the analytical calculations (Eq. 3.11).

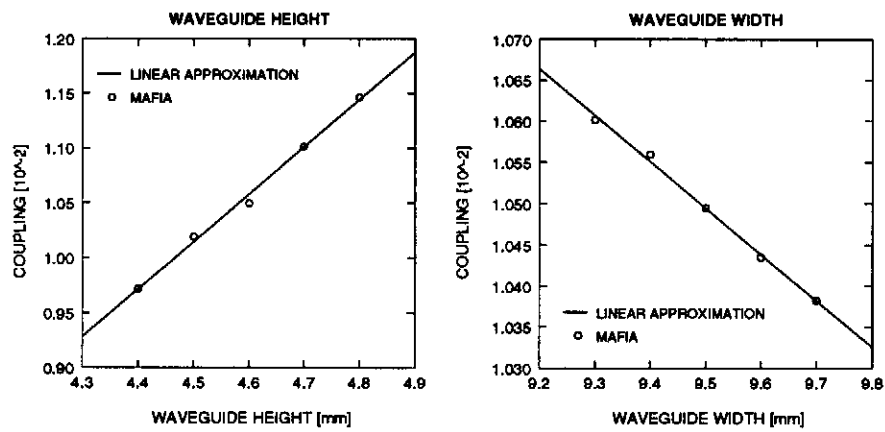


Figure 3.11: Tolerances for the outer waveguide dimensions. Design values are 9.5 mm for the waveguide width and 4.6 mm for the waveguide height.

3.4 Transition Step

The last element of one waveguide BPM channel is the impedance matching to $50\ \Omega$ and the vacuum transition. For the vacuum transition an ultra-high vacuum microwave feedthrough² was foreseen. This ultra-high vacuum feedthrough is small and is matched up to 20 GHz. For the design of prototype I, this

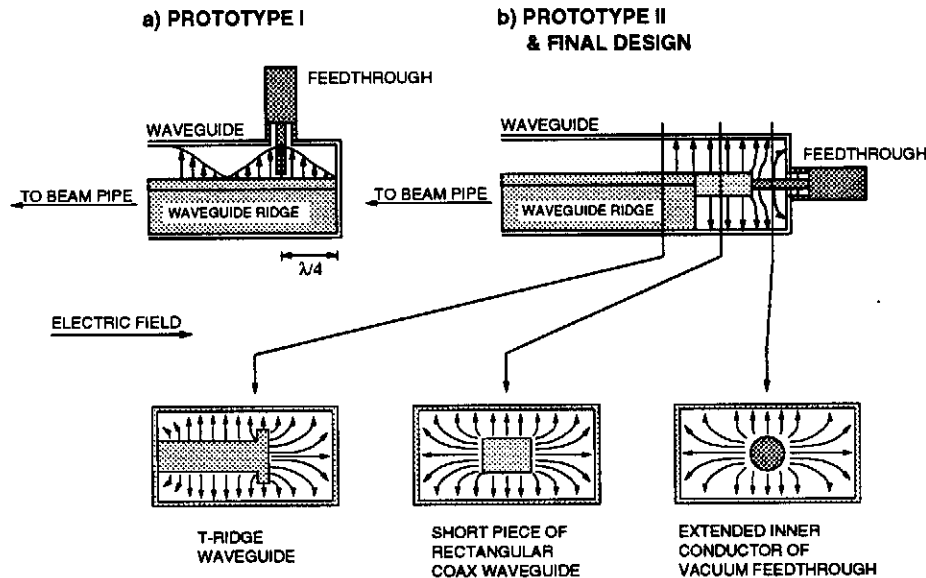


Figure 3.12: Transition steps between T-ridge waveguide and outer world coaxial system in development stages. Top left shows system used for prototype I, top right for prototype II. Below profile cuts for the three stages in prototype II are depicted .

feedthrough was equipped with an extended inner conductor and positioned $\lambda_w/4$ away from the closed wall of the waveguide to serve as an antenna coupling to the electric field of the fundamental mode (see Fig. 3.12a). To enhance the coupling to the electric field inside the waveguide, a pill was modelled around the tip of the extended inner conductor of the feedthrough. The resulting adapter was very narrowband, difficult to be tuned to $f_w = 12\ \text{GHz}$, and the welding into special flanges caused problems. In a new design (prototype II) a smooth transition from the waveguide into the feedthrough has been realized by a $\lambda/4$ -transformer, formed by a rectangular coaxial line (see Fig. 3.12b). This new design resulted in a closer spacing of both planes in beam direction, because all elements are now perpendicular with respect to the beam axis. Furthermore, the second design

²by KAMAN Corp.

has larger bandwidth (no tuning problems), and is better for fabrication and installation. In Fig. 3.13 results from MAFIA simulations for reflection parameter

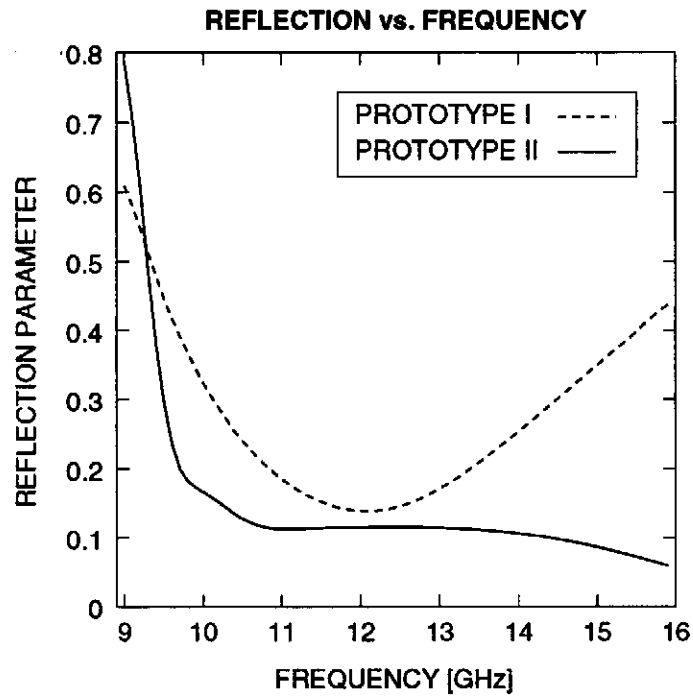


Figure 3.13: Results from MAFIA simulations for reflection parameter studies of both types of vacuum and field transition.

studies of both types of vacuum and field transition are shown.

3.5 Wake Field Estimation

Interferences in terms of wake fields can lead to a degradation of the FEL performance. For the TTF-FEL an electron beam with small energy spread of less than 0.1% is required to drive the SASE process. During the passage of the electrons through the undulator beamline wake fields are generated, which introduce an additional energy spread in the beam. The longitudinal wake fields due to the resistivity and roughness of the inner beam pipe surface are estimated in [31]. The effect of these wake fields on the FEL performance is investigated in [9]. These simulations show that the impact of wake fields for TTF-FEL Phase I with an electron bunch length of $250\ \mu\text{m}$ is negligible, while for TTF-FEL Phase II a reduction of the saturation power of 30% was simulated including wake field effects. The saturation length remains the same. Compared to simulations of the undisturbed amplification, where wake fields are not applied, the degradation is up to 50%, which is tolerable regarding the overall gain of more than 10^7 [32].

3.5.1 Wake Field Quota

For the wake field budget of all components of the TTF-FEL beamline (cavities, pumping slots, BPMs, wire scanners, and beam pipe surface) numerical and analytical studies have been performed [31]. The impact of the waveguide BPMs was studied with MAFIA simulations and with the diffraction model. Fig. 3.14 shows the wake potentials for the two bunch length for TTF-FEL Phase I and II caused by one BPM slot and waveguide combination as simulated with MAFIA. As it can be seen in Fig. 3.14, the wake field generated by the waveguide BPM will lead to an energy loss of those particles following the head particles inside the bunch. For the MAFIA computation, numerically reliable results can only be obtained, if the structure is modelled with high precision on a 3D grid with grid spacing in the direction of propagation of $\sigma_z/10$. For bunch length down to $\sigma_z = 50\ \mu\text{m}$ and a complete structure length of several mm this causes an undesirable long computation time. To limit the computing time, the peak wake potential was calculated for few bunch length values between $500\ \mu\text{m}$ and $50\ \mu\text{m}$ and the systematic between both is investigated. Since the bunch length is much shorter than the beam pipe radius, the diffraction wake field model [33] can be applied to estimate the peak wake potential for the waveguide BPM units. Inside the model every discontinuity is regarded as a pill-box cavity with a radius larger than the beam pipe radius. In the region upstream the cavity-like discontinuity the beam accompanying field is given by a plane wave with the same time-

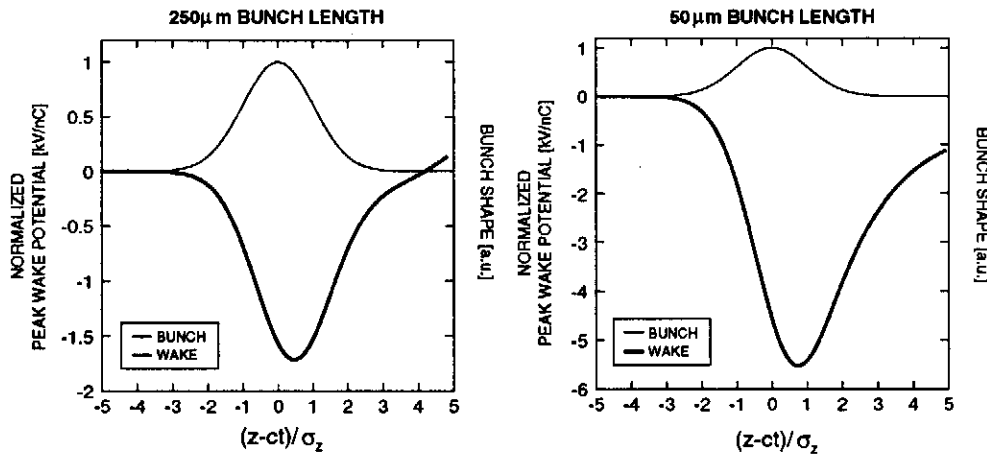


Figure 3.14: Normalized peak wake potential for two bunch lengths: 250 μm (Phase I) and 50 μm (Phase II). The head of the bunch passing the BPM structure is to the left of the horizontal axis, the tail to the right. Different scaling of the two vertical axis is applied. .

dependency as the beam current. As the beam enters the cavity, this plane wave is diffracted by the entrance edge as sketched in Fig. 3.15. The energy loss and thus the longitudinal wake field effect is given by the energy contained in the diffracted field. The depth of the cavity d is assumed to be larger than the

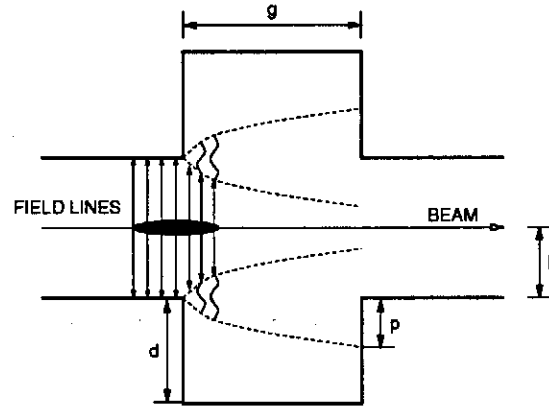


Figure 3.15: Diffraction model for the wake field of a cavity-like discontinuity in a beam pipe. The region between the dashed curves indicate the region where the fields are pertubated by diffraction.

penetration depth p of the diffracted field like

$$d > p = \frac{1}{2\pi} \sqrt{\frac{\lambda g}{2}} \quad (3.12)$$

for wavelength $\lambda \gg \sigma_z$. As the wave is diffracted, half of the diffracted field energy goes into the shadow region, while the other half is diffracted toward the pipe region and propagates down the pipe with the beam. The diffraction model applies for the longitudinal peak wake field W_z^{peak} [34]

$$W_z^{\text{peak}} = \frac{\Gamma(1/4)}{4\pi^{5/2}} \frac{Z_0 c}{b} \sqrt{\frac{g}{\sigma_z}} \quad (3.13)$$

with $\Gamma(1/4) \approx 3.63$. The root-mean-square wake field is then $W_z^{\text{rms}} = 0.4 \cdot W_z^{\text{peak}}$. The peak wake field amplitude scales with $W_z \sim \sigma_z^{-1/2}$. If the MAFIA results for different bunch length reflects this scaling, the diffraction model is useful to estimate the wake field effect of a BPM channel. Fig. 3.16 shows MAFIA

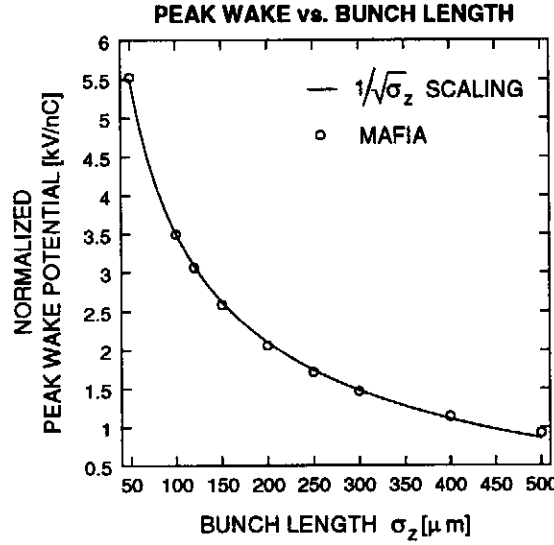


Figure 3.16: Peak wake field amplitudes computed by MAFIA fitted to the diffraction model.

simulation results together with the $W(\sigma_z) \propto \sigma_z^{-1/2}$ model. As can be seen in Fig. 3.16 the diffraction model describes sufficiently the wake field dependency for different bunch length and can hence be used to calculate the effect of the waveguide BPMs. In Tab. 3.1 the effect of the waveguide BPMs and the other objects is summarized. Including all objects, the effect of the waveguide BPMs is small (20% for Phase I and 10% for Phase II where the number of BPMs is doubled). The overall energy spread due to wake field effects is rather tolerable for Phase I, while for Phase II special care must be taken in order to decrease the total wake field. Since also for Phase II the impact of waveguide BPMs is small compared to the other elements in the undulator beamline, the design of the coupling slot can be kept for this phase of the project.

Object	Phase I	Phase II
	Peak Wake	[kV/nC]
Undulator pipe:		
Resistive wall	64	778
Oxide Layers	0.4	16.8
Surface roughness	24	1620
Inside modules:		
BPMs	45	309
Diagnostic stations:		
Cavities, wire scanners	85	380
Pumping slots	12	234
Sum (all objects)	231	3337
Sum (w/o surface roughness)	207	1716
Energy spread:		
All objects	0.06	0.33
w/o surface roughness	0.054	0.17

Table 3.1: Summary of the peak wake potential for several objects in the TTF-FEL undulator beamline for Phase I and II [31].

Chapter 4

Measurements

In this chapter different measurements on the two prototypes of the waveguide BPMs are discussed. In the first part, a laboratory setup is described enabling measurements of specific BPM parameters. Furthermore measurements under real beam conditions at the CLIC Test Facility 2 (CTF2) and S-Band Test Facility (SBTF) are reported. These measurements also served as tests for possible signal processing electronics.

4.1 Measurements in Laboratory

Laboratory measurements are useful to confirm predictions by simulations and to study specific monitor parameters under idealized conditions. Furthermore calibration methods can be tested. To check matching stages, observe cut off frequencies, and to look for trapped resonances in the waveguides, broadband measurements were performed. Once the transfer characteristics of the waveguide BPM was clear, mapping scans at the working frequency were carried out.

One of the main difficulties is to conceive an appropriate method to simulate the electromagnetic field distribution of an offset beam.

4.1.1 Simulating an Electron Beam

The electromagnetic field propagating with a relativistic electron beam is similar to the TEM-mode of a coaxial system (see Fig. 4.1a and Appendix A for more details). Such a system can be created by placing a cylindrical conductor like a wire or an antenna inside the BPM beam pipe. In Fig. 4.1b an assembly of

such a coaxial system consisting of the inner vacuum chamber and a rigid cable is sketched. At the end of the extended inner conductor the field radiates out

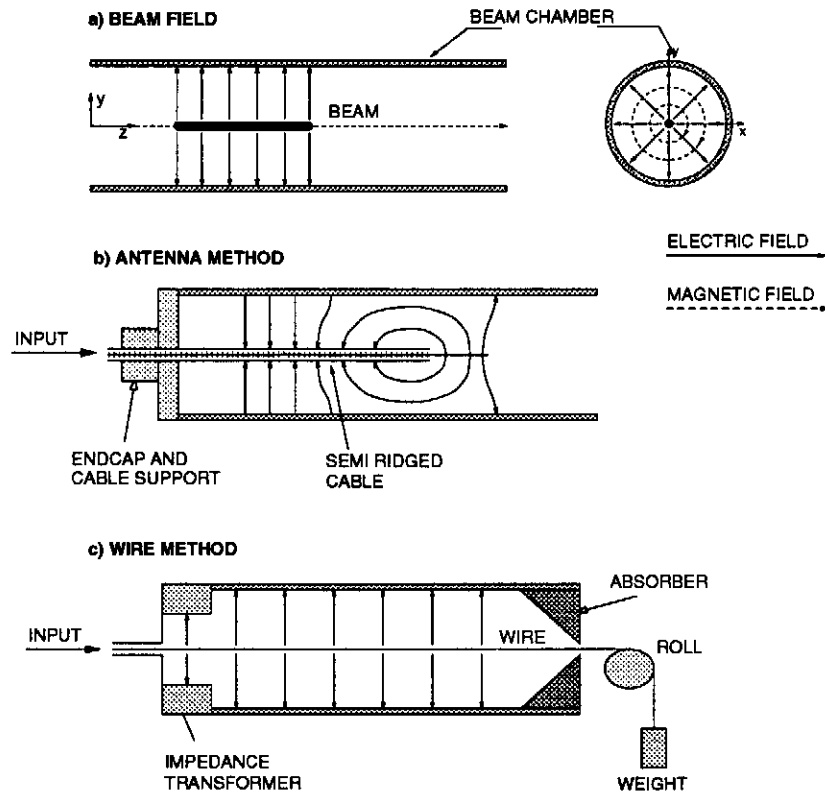


Figure 4.1: a) With beam co-propagating electric field; b) Field distribution simulated using an antenna; c) Field distribution created by a coaxial system of wire and inner surface of vacuum chamber.

of the coaxial cable and bends until it reaches the inner vacuum surface. Two electromagnetic waves are excited, one propagates to the left building up the TEM characteristic field distribution, and one going to the right in tube direction (see Fig. 4.1b). The wave going to the right will be damped because the driving frequency is below the cut off frequency of the vacuum pipe. The wave going to the left builds up the characteristic TEM-mode with the metallic tube for the inner conductor and the beam pipe as the outer conductor. If the coupling window of the BPM is located sufficiently away from the tip of the antenna, the signals of this device should match those of a relativistic electron beam. The back plate with integrated absorber prevents the electromagnetic wave from being emitted out into the environment.

In Fig. 4.1c an alternative setup is depicted. The beam field will be simulated by a coaxial system consisting of a wire stretched through the BPM structure

and the inner surface of the vacuum chamber. At the input side, an impedance transformer has to be inserted, because otherwise electric power will be reflected at the transition step between the coax cable coming from the signal source and the pipe-wire system. At the end of the path, the electric power has to be dumped inside an absorber to prevent reflected power to travel back and produce standing waves inside the BPM chamber.

The antenna method has the advantage to be mechanically simple and only one support stage is needed. Major drawbacks are the finite size and the straightness of the ridged cable. A straight line is easier achieved with a stretched wire. Furthermore wires made from good conductors are available in sizes which meet the root-mean-square transverse bunch size of the TTF FEL electron beam. Thus a test bench with a stretched wire was planned for prototype tests.

The generation of a sharply peaked signal simulating the pulsed signal from a 1 ps long bunch with 1 nC charge with a pulse generator is a demanding task and not realizable with the wire setup envisaged for prototype tests. In consequence frequency domain measurements are confined to frequencies up to 20 GHz, realizable with a vector network analyzer (NWA). For monitor parameter measurements, a signal generator delivering a continuous wave with 12 GHz is sufficient, because any other unwanted frequencies will be filtered by the first stage of the signal processing electronics.

4.1.2 Testbench Description

For test measurements a setup as sketched in Fig. 4.2 was constructed and built. In order to avoid high frequency oscillations from a moving wire and because of the low weight of the prototype the BPM itself is moved with respect to the wire. For this, the prototype is sandwiched between two steel plates fixed to an assembly of two positioning stages¹. In unidirectional mode, the manufacturer specifies the repeatability to 0.3 μm . The frame supporting the stretched wire consists of two pairs of support rests, one pair at each end of the BPM. On the input side, the rest pair is housing an N-connector with inserted wire fixing. The end of a 250 μm diameter copper-beryllium wire is soldered to the extended inner conductor of the N-connector, then the wire is guided through a Teflon cylinder impedance matching. The flange housing the impedance transformer is not fixed to the BPM flange. To provide electrical contact, a RF-spring is mounted to the flange. On the other side of the BPM a flange containing an absorber is

¹Aerotech ATS0300

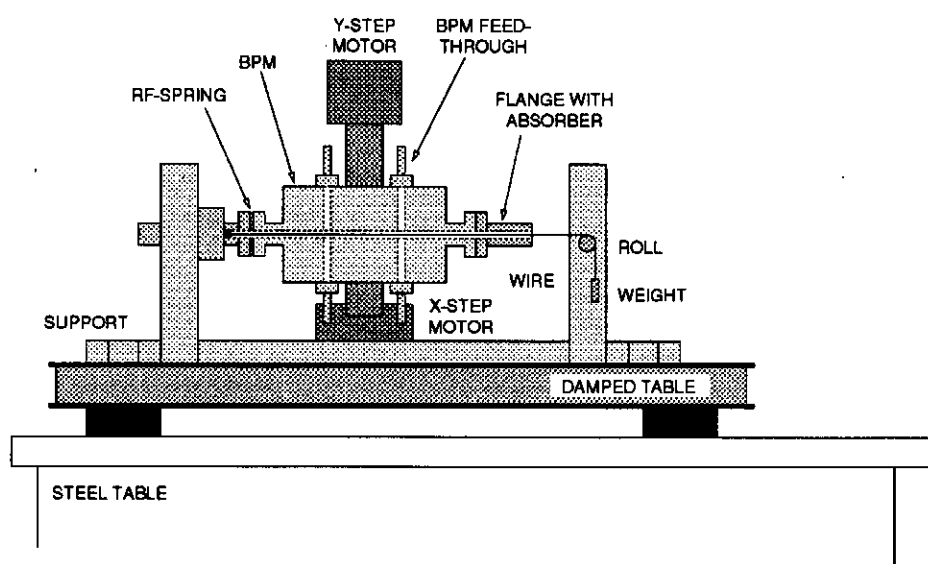


Figure 4.2: Schematics of the mechanical facet of the BPM prototype testbench.

screwjoint to the second flange. The wire is guided to a role fixed and stretched with an attached weight. The whole setup, the supporting rests constructed from aluminum elements² as well as positioning stage assembly is mounted onto a damped table³.

For narrowband measurements the test signal is created by a signal generator⁴ set at 12 GHz delivering a continuous wave signal with 14.8 dBm power feeding the wire-BPM coaxial system (see Fig. 4.3). Signals excited in the waveguides are transferred via lowloss microwave cables (damping 1 dB/m at 12 GHz) to a an electronics box, were signals are first filtered at 12 GHz with a bandwidth of 730 MHz and then amplified by 20 dB. Because the signal detecting powermeter⁵ has only two input ports, the filtered and amplified signals have to pass a relay cascade. Via an IEEE 488 interface, the powermeter is read out by a PC running a data acquisition application⁶. This application also controls the stepping motor control box⁷ and reads out two step sensors monitoring the stepping motor movements.

²from MicroTec Corp.

³from Newport Corp.

⁴Rhode and Schwarz SMP 02

⁵Gigatronics 8542 C

⁶realized with Labview

⁷Unidex 11

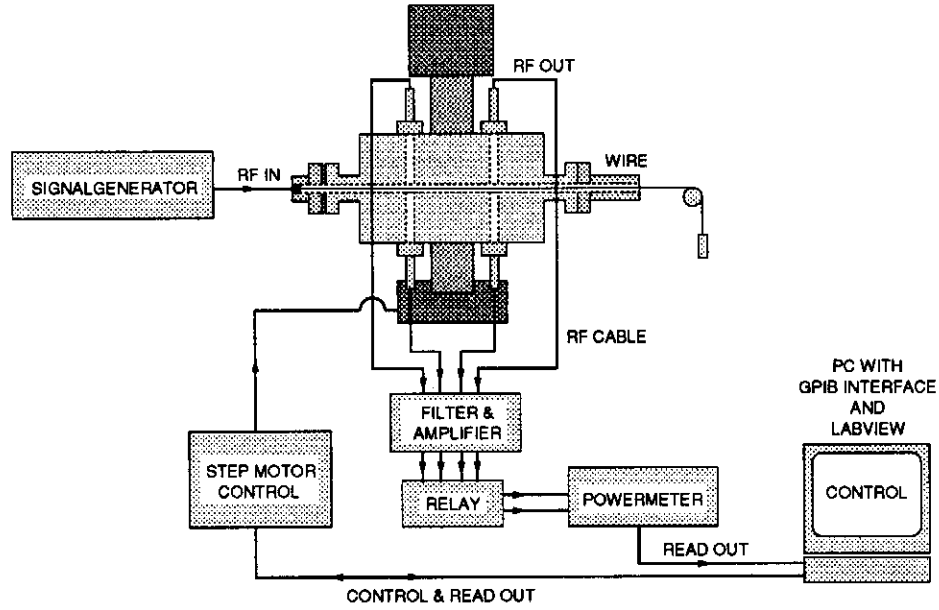


Figure 4.3: Schematics of the electrical facet of the BPM prototype testbench.

Impedance Matching

Due to the low coupling of a BPM channel to the input signal, special care is necessary to avoid reflections and standing waves in the experimental setup, here in the microwave transmission line from input port to absorber. For this a two-stage $\lambda/4$ -transformer was placed at the input side of the BPM as sketched in Fig. 4.4a. Task of this transformer is to match the impedance of the N-connector ($Z_N = 50 \Omega$) to that of the inner beam pipe surface wire coaxial system, which has an impedance of $Z_C = 263 \Omega$. A transformation impedance of $Z_T = \sqrt{Z_N \cdot Z_C} = 115 \Omega$ was split up in two stages with $Z_{T1} = 76 \Omega$ and $Z_{T2} = 174 \Omega$. The first stage can easily be created by extending the inner conductor

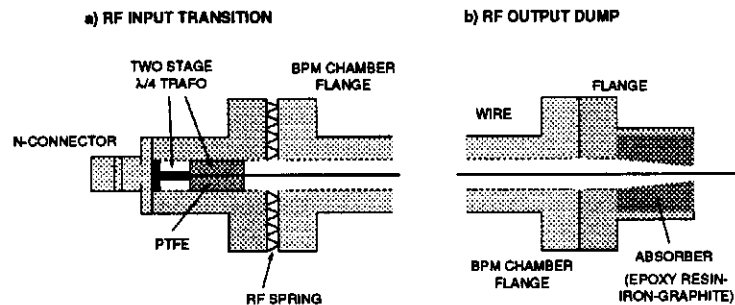


Figure 4.4: Detail sketch of RF input and output ports of the testbench.

of the N-connector into the beam pipe. For the second stage, a modification of the space between wire and inner beam pipe is obvious by means of inserting a dielectric medium. To create an impedance of $Z_{T2} = 174 \Omega$ with the wire and the inner beam pipe surface, PTFE (Polytetrafluoroethylene) with a dielectric constant of $\epsilon_r = 1.6$ serves this purpose. At the output side an absorber was placed to avoid reflections from the incoming wave and thus different amplitudes of the input signal at the two detection planes. Absorber for microwaves can be mixed⁸ by adding a mixture of graphite and iron powder to epoxy resin.

Wire Adjustment

Before starting with measurements of specific monitor parameters the wire has to be centered inside the BPM with respect to the mechanical center of the beam pipe.

After an initial empirical alignment with a survey tool it is possible to increase the alignment accuracy with measurements of the transmission characteristics of the coaxial system of wire and beam pipe [35]. Moving the wire out of the center of the beam pipe will change the impedance according to [36]

$$Z_L = \frac{Z_0}{2\pi\sqrt{\epsilon_r}} \operatorname{arcosh} \left(\frac{D^2 + d^2 - 4e^2}{2Dd} \right) \quad (4.1)$$

with dimensions as in Fig. 4.5a and $Z_0 = 377 \Omega$ for the vacuum impedance. The variation of the characteristic impedance can be measured with a network analyzer as the S_{11} reflection parameter of a two-port network, with S_{11} defined as

$$S_{11} = \frac{Z_C - Z_L}{Z_C + Z_L} \quad (4.2)$$

and $Z_C = 263 \Omega$ the impedance of the system with centered inner conductor. This method only works if the end of the coaxial system is matched in the sense of the impedance, because otherwise reflections at the end of the signal line will cause perturbations of the reflection parameter. For a testbench as described in the previous section this is no problem, because all power will go into the absorber placed at the end of the setup. With such a testbench measurements with both prototypes were performed to estimate BPM parameters like coupling amplitudes, gain factors, angle of the sensitive slot center, and the sensitivity.

⁸The recipe for the absorber used here reads: 1 part graphite powder, 2 parts iron powder mixed with even parts of resin and hardening additive

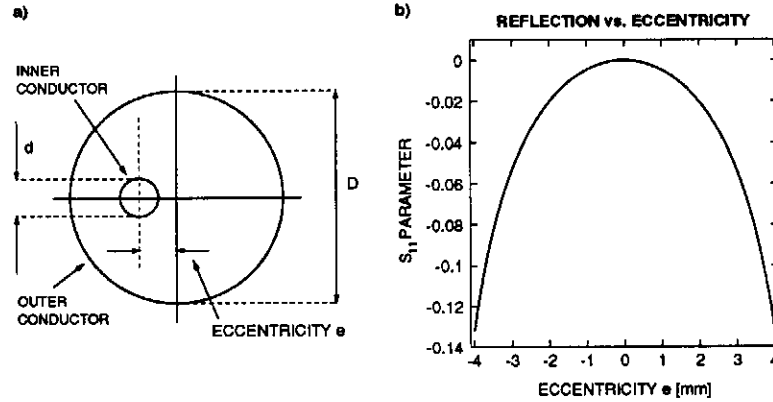


Figure 4.5: a) Profile of a coaxial system with eccentric inner conductor, b) Reflection parameter for an eccentric inner wire with $d = 125 \mu\text{m}$ in a beam chamber with $D = 9.5 \text{ mm}$.

4.1.3 Transfer Characteristics

The transfer characteristic of each BPM channel was measured with the wire test bench by measuring the S_{21} transmission parameter for a broadband frequency up to 16 GHz with a Network Analyzer (NWA). In Fig. 4.6 the experimental setup is shown. The device under test, in this case the BPM, is connected to

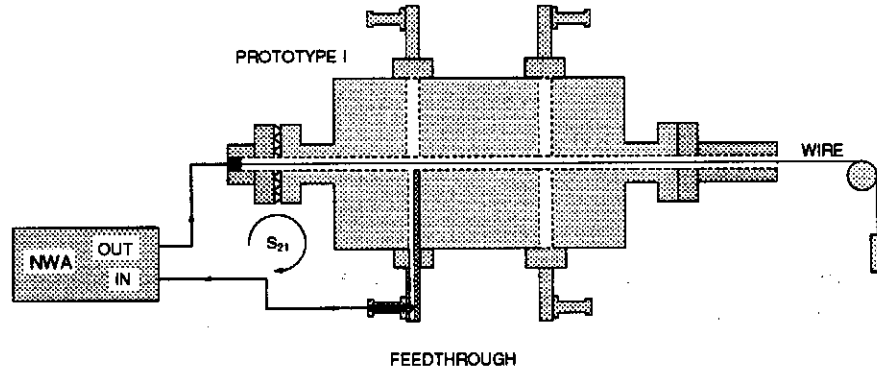


Figure 4.6: Experimental setup for measurements of the transfer characteristics of the BPM channels.

the ports of the NWA. For a broadband spectrum from 50 MHz to 16 GHz the transmission coefficient is measured and displayed. With this setup, the cut off frequency of the waveguide and interferences in this frequency range were analyzed.

Prototype I

A result for the transfer characteristics of one channel of prototype I is shown in Fig. 4.7. As expected from MAFIA simulations the transmission is rather

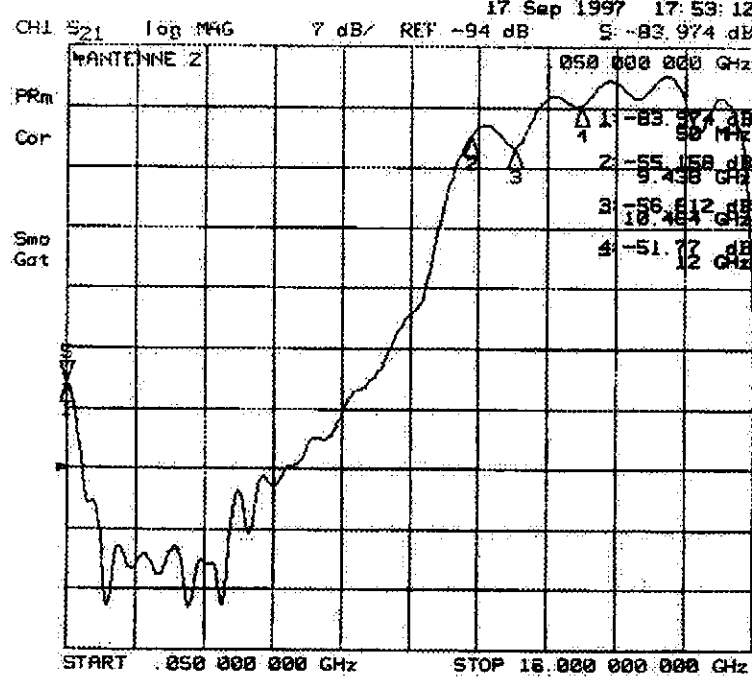


Figure 4.7: S_{21} parameter measured for one channel of prototype I. Above cut off transmission rises to -42 dB at 12 GHz with respect to -94 dB reference. This corresponds to 0.8 % coupling amplitude at 12 GHz.

low until the cut off frequency of the waveguide is reached. From there on, the transmission coefficient rises as a function of the frequency until 9.5 GHz with the high-pass characteristics of the waveguide. Beginning with this frequency trapped resonances are visible as peaks at defined frequencies. Waveguides of length l , which are not perfectly matched at both ends in direction of wave propagation, have q longitudinal resonances above cut off f_c according to

$$f_r^2 = f_c^2 + \frac{c^2}{4} \left(\frac{q}{l} \right)^2. \quad (4.3)$$

The length of the waveguide is here $l = 98.4$ mm with tolerances. So each waveguide will exhibit a different resonance pattern. This may be turned into a measurement technique to evaluate the length of each waveguide inside the

BPM chamber. Regarding the coupling, these resonances cause coupling amplitude differences among the four channels as visible in Tab. 4.1, where coupling amplitude measurements at 12 GHz for all four channels are listed. The ampli-

	Coupling [%]
CH1	0.44
CH2	0.57
CH3	1.51
CH4	0.64

Table 4.1: Coupling at 12 GHz for prototype I.

tude varies by a factor of three among all channels. Shifting any resonance by length variation to 12 GHz will alter the coupling amplitude by around 6 dB. Another reason for the strong distinctions are tolerances in the position of the antenna, which realizes the coupling to the electric field inside the waveguide. This antenna had to be welded very precisely perpendicular to the waveguide at a distance of $\lambda_w/4 = 6.25$ mm away from the shorted end of the waveguide. A shift of ± 200 μm for the feedthrough position along the waveguide longitudinal axis causes a variation of the coupling frequency of ± 0.5 GHz. Tuning stubs for the waveguide were not foreseen, since stubs or screws can cause problems on the vacuum compability of the device. The left photo in Fig. 4.8 shows the mechani-

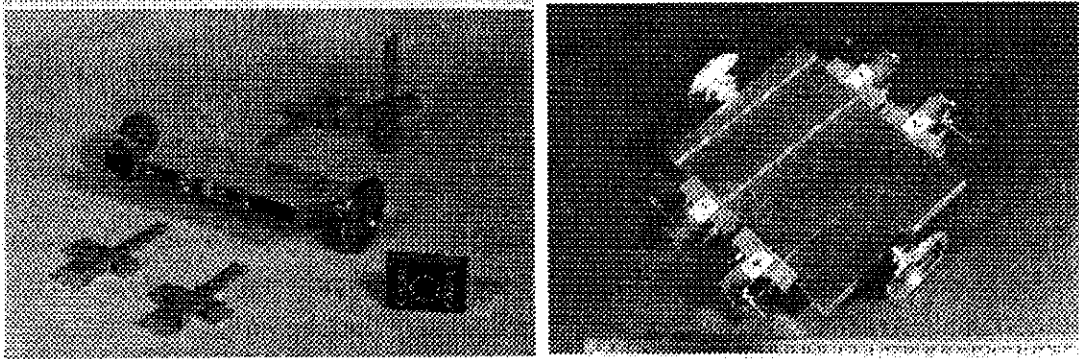


Figure 4.8: Prototype I before (left) and after (right) welding of feedthroughs and vacuum cleaning.

cal parts of prototype I. The waveguide ridge is integrated into the flange, which is put into the extruded rectangular waveguide structure in the BPM chamber. If the length of the inner ridge deviates from the length of the structure inside the beam pipe, contact between the end of the ridge and the vacuum chamber is

not guaranteed. A shorter ridge results then in a poorer electrical contact, which in turn will decrease the coupling amplitude.

Prototype II

Since for prototype II a more broadband transition between waveguide and vacuum feedthrough was designed, variations of the coupling amplitude among channels should be quite lower than at prototype I. Another advantage of the broadband transition to the vacuum feedthrough is the fact, that resonances will obey a smaller quality factor and in consequence will not spoil the coupling amplitude.

For prototype II, the inner conductor of the rectangular coaxial conductor was brazed to the inner conductor of the vacuum feedthrough. Problematic was the electrical contact between waveguide ridge and the rectangular block. For the final design of the waveguide transition for the BPMs in the undulator module, the transformer was fabricated in one step together with waveguide ridge structure by EDM. After that, a hole with the size of the extended inner conductor of the feedthrough was drilled into the inner transformer block, used to host the end of the inner conductor of the feedthrough. By this technique, sufficient electrical contact as well as correct positioning of the elements is provided [37].

Due to the lack of time, broadband measurements with NWA are not available for display. After completion of the mechanical parts of prototype II, it was quickly moved into the beamline of SBTF for tests under beam conditions. These tests will be described later in this chapter.

4.1.4 Gain

The discrepancy between an ideal and a real BPM is described by the gain factor. This factor summarizes all mechanical imperfections and imbalances among the four channels of one BPM unit are summarized. Determination of the gain is thus the first step to calibrate each BPM unit. In the following a measurement technique is described to evaluate the gain factor with narrowband wire testbench measurements.

Definition

As mentioned above the gain factor is needed to describe the difference between a real and an ideal BPM channel. The response of an ideal BPM channel can

be calculated using image charges as described in Appendix A by

$$S_i = \frac{b^2 - r^2}{b^2 + r^2 - 2br \cos(\phi_i - \theta)} \quad (4.4)$$

for a slot at (b, ϕ_i) responding to a beam at position (r, θ) . Due to the individual transfer characteristics of each channel the measured voltage for each channel depends on the ideal response function S_i modified with the channel gain g_i to

$$V_i = q \cdot g_i \cdot S_i \quad (4.5)$$

where q is a factor describing the amplitude of the input signal. Normalized with the input amplitude q in the electrical center of the BPM all signals should have equal amplitude. Hence the gain of one particular channel is the inverse transmission parameter at 12 GHz normalized to the amplitude induced for a centered wire.

Measurements

Gain parameters can be estimated by measuring the induced voltage $V_{i,j}$ for $j = 1 \dots n$ wire positions in the BPM aperture and fit this measurements to a model $M_{i,j}$ for the i th coupling channel

$$\begin{aligned} M_{i,j} &= g_i \cdot \frac{b^2 - r_j^2}{b^2 + r_j^2 - 2br_j \cos(\phi_i - \theta_j)} \equiv M(i, j; \mathbf{a}) \\ i &= 1 \dots 4 \quad \text{and} \quad j = 1 \dots m \\ \mathbf{a} &= (g_1, g_2, g_3, g_4). \end{aligned}$$

To obtain different $V_{i,j}$ the wire was moved on a grid with side length $L_x = L_y = 1$ mm and step width $\Delta x = \Delta y = 20$ μm in the central region of the BPM. At each point the position (r_j, θ_j) was measured using the stepping sensors and written into a table. See section 4.1.2 for a complete description of the setup. Induced signals have been filtered, amplified, and then measured using a powermeter. To exclude effects from the imbalance among amplifiers, cables, and filters, detected voltages were divided each by their amplification factor. Then these values were also written into a table.

Results

Results for measurements with both prototypes are listed in Tab. 4.2. The Result for prototype I reflects expectations from broadband measurements of the

	Prototype I	Prototype II
g_1	1.0000 ± 0.0018	1.0000 ± 0.0018
g_2	0.5609 ± 0.0011	0.9054 ± 0.0017
g_3	0.3273 ± 0.0006	1.0668 ± 0.0017
g_4	0.6922 ± 0.0014	1.0094 ± 0.0019

Table 4.2: Derived gains normalized to $g_1 = 1$.

transfer characteristics. Variations by a factor of three are also visible here. For prototype II the situation is much more balanced. The broadband matching with the transformer reduces the amplitude of trapped modes dramatically, such that the gains are much closer to the design value with a small root-mean-square spread.

Furthermore the image current model proved to be a sensible description of the BPM response to an offset beam. To further enhance the precision of the description of the prototype BPMs, estimates concerning the sensitive center of each coupling slot were carried out. This is one of the problematic points of this model, since the model assumes a point-like coupling slot. Hence in the following an analysis is presented, covering the estimation of the angle of the sensitive center of each coupling slot.

4.1.5 Coupling Slot Angle

In first order approximation this slot can be assumed to be point-like. The more one wants to analyze beam offsets far away from the center of the BPM, the more the size of the slot plays an important role for the response function. Keeping this mind in following the slot is assumed to be point-like, which is valid if one restricts the analysis to beam offset with radius $r \leq b/2$ [38].

Measurement

To estimate the center of each coupling slot, a complete array of data values was recorded for prototype I while the wire was moved on a grid as sketched in Fig. 4.9a, with dimensions $L_x = L_y = 1$ mm and steps of $\Delta x = \Delta y = 20$ μm . The measured values for $i = 1 \dots 4$ coupling channels can be arranged into a matrix $V_{i,j}$ with $j = 1 \dots m$ set wire positions. In extension to the analysis above here the measured voltages are normalized with the estimated gain factors

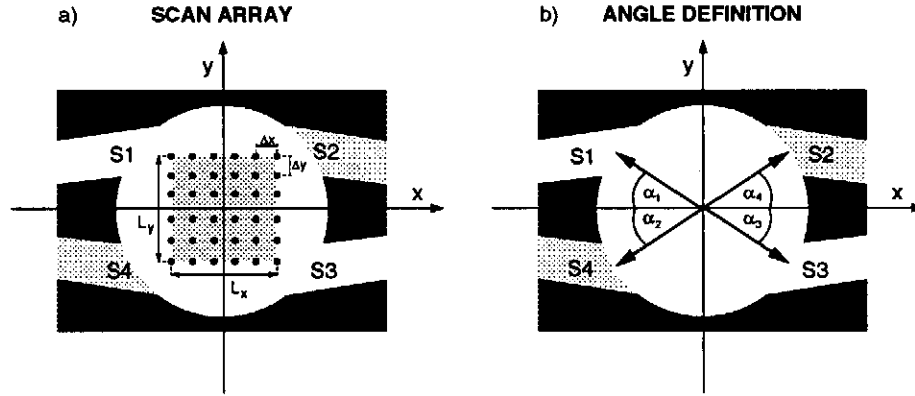


Figure 4.9: Schematics of the array for angle estimation.

for each channel. For each of this points the induced voltage can be modelled with

$$M_{i,j} = \frac{b^2 - r_j^2}{b^2 + r_j^2 - 2br_j \cos(\alpha_i - \theta_j)} \equiv M(i, j; \mathbf{a})$$

$$i = 1 \dots 4 \quad \text{and} \quad j = 1 \dots m$$

$$\mathbf{a} = (\alpha_1, \alpha_2, \alpha_3, \alpha_4).$$

This model can be fitted in a least square sense to the data values collected in $V_{i,j}$, allowing to vary the coupling slot angle α_j of each slot center with the horizontal axis (see Fig. 4.9b for definition). The chi-square to be minimized can then be written to

$$\chi_i^2 = \sum_{j=1}^m \frac{(V_{i,j} - M_{i,j})^2}{\sigma_j^2} \quad (4.6)$$

with σ_j^2 reflects the squared error for each induced voltage measurement. Since this error will not vary with time, it can be assumed to be constant.

Results

Results for the coupling slot angles are listed in Tab. 4.3 for both prototypes. Two angles for prototype I (α_2, α_3) agree with the design value of $\alpha = 35.51^\circ$ while two differ by more than 2° . The EDM manufacturer stated, that two EDM channels were not produced according to specifications with no further information. These channels may be identified with (α_1, α_4).

For prototype II there is also a systematic deviation between design and derived values. Two angles (α_1, α_3) are bigger than the design value while two (α_2, α_4)

	α [deg]	
	Prototype I	Prototype II
CH1	33.42 ± 0.10	35.94 ± 0.13
CH2	35.79 ± 0.06	33.46 ± 0.09
CH3	35.58 ± 0.02	35.92 ± 0.14
CH4	32.34 ± 0.31	34.20 ± 0.13

Table 4.3: Coupling slot angles for both prototypes as derived from a fit with the wire testbench.

are smaller. Since they come in pairs of cross facing waveguides which run along parallel, a possible explanation would be, that the complete chamber is tilted inside the testbench. At closer look this assumption sounds more sensible, if one compares the difference between the average of the parallel angle values. This would result in a tilt of 1° between the reference frame of the BPM and the test bench system.

4.1.6 Sensitivity

The sensitivity of a BPM describes the change of the induced signal amplitude for a given beam offset. It is therefore a figure of merit for the dynamic range which the signal processing electronics have to cope with.

Definition

Assume a beam position monitor with linear response in the central region. Thus the relationship between induced signals and beam position offset is given by ⁹

$$x = b_x \cdot F_x \quad \text{and} \quad y = b_y \cdot F_y \quad (4.7)$$

where F_x and F_y are the signalfunctions derived from normalized differences of the induced voltages according to (for the horizontal direction)

$$F_x = \frac{L - R}{L + R} = \frac{(S_1 + S_4) - (S_2 + S_3)}{S_1 + S_4 + S_2 + S_3}. \quad (4.8)$$

Analog for the vertical direction. The monitor constants b_x and b_y depend on the monitor geometry. The sensitivity $S_{x,y}$ is defined as the slope of signalfunction

⁹In section 5.6 a more complete treatment on this subject is given

with respect to beam offset

$$S_x = \frac{\partial F_x}{\partial x} \quad \text{and} \quad S_y = \frac{\partial F_y}{\partial y} \quad (4.9)$$

and is thus the inverse of the monitor constant. The dimension of the sensitivity is usually given in $[S_{x,y}] = \frac{1}{\text{mm}}$. To derive the sensitivity of a BPM in terms of $\frac{\text{dB}}{\text{mm}}$, one has to combine Eq. 4.7 and 4.8 for the horizontal direction to

$$\frac{x}{b_x} = \frac{L - R}{L + R} \quad (4.10)$$

and rewrite it to

$$\frac{L}{R} = \frac{1 + x/b_x}{1 - x/b_x}.$$

or in decibels

$$20 \log \left(\frac{L}{R} \right) = 20 \log \left(\frac{1 + x/b_x}{1 - x/b_x} \right) = \frac{20}{\ln(10)} \ln \left(\frac{1 + x/b_x}{1 - x/b_x} \right). \quad (4.11)$$

To get a more convenient expression, the next step is to expand the term on the right side into a Taylor series. Taking only the first order into account

$$20 \log \left(\frac{L}{R} \right) = \frac{40}{\ln(10)} \cdot \frac{x}{b_x} = x \cdot S_x \quad (4.12)$$

results in an expression in terms of the monitor constant b_x and in the log-ratio of the induced voltages.

Measurements

Measurements of the sensitivity were performed with both prototypes mounted on the wire testbench. The wire was moved on both axes within a range of $L_x = L_y = \pm 500 \mu\text{m}$ with a step width of $\Delta x = \Delta y = 10 \mu\text{m}$ as sketched in Fig. 4.10. Induced signals for all channels were filtered, amplified, and finally displayed on a powermeter which was read out by a PC. The relative error for each powermeter value is 0.25 % according to manufacturers specifications. At each measurement point, values for horizontal and vertical wire positions and all four induced powers were written into a table. From the power values induced voltages were calculated by $V_{ind} = \sqrt{P_{ind} \cdot R}$, with $R = 50 \Omega$ for the input load of the signal processing electronics. Induced voltages were then normalized with the amplification and damping factors of each signal processing line. In the next step virtual signalfunctions L and R for the horizontal direction were calculated

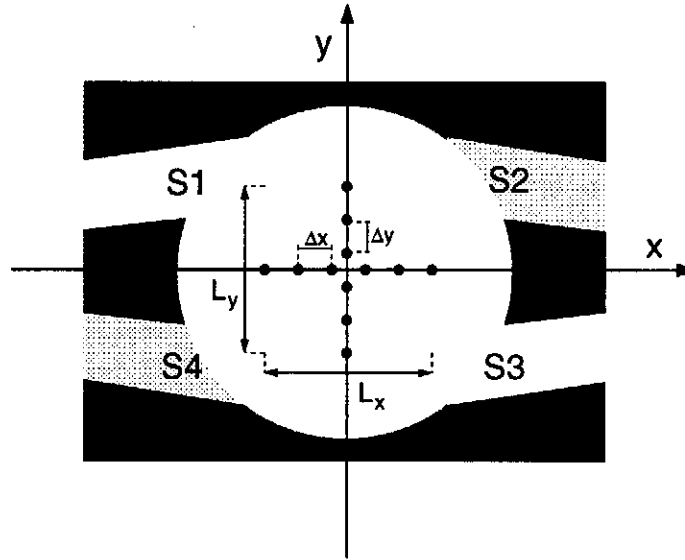


Figure 4.10: Schematics of array for cross scan measurements .

according to Eq. 4.8 and analog for the horizontal direction. The sensitivity S_x for the horizontal and S_y for the vertical direction is then the slope between set positions x (or y) and the logarithmic ratio of L and R (or U and D)

$$x \cdot S_x = 20 \cdot \log \left(\frac{L}{R} \right) \quad \text{and} \quad y \cdot S_y = 20 \cdot \log \left(\frac{U}{D} \right) \quad (4.13)$$

Results

In Fig. 4.11 values for the log-ratio are plotted against wire position values. Resulting sensitivities for both prototypes are listed in Tab. 4.4. The slot posi-

	Prototype I	Prototype II
S_x [dB/mm]	5.597 ± 0.078	5.786 ± 0.037
S_y [dB/mm]	3.815 ± 0.077	4.102 ± 0.036

Table 4.4: Sensitivities for both prototypes as derived from measurements with the wire testbench. Errors are derived from the systematic errors of the testbench and from the statistical error from the linear regression.

tioning is the main reason for the moderate improvement of the sensitivities for prototype II compared to prototype I. In prototype II the slot is closer located to the T-ridge bar of the waveguide enabling a better coupling to the beam field.

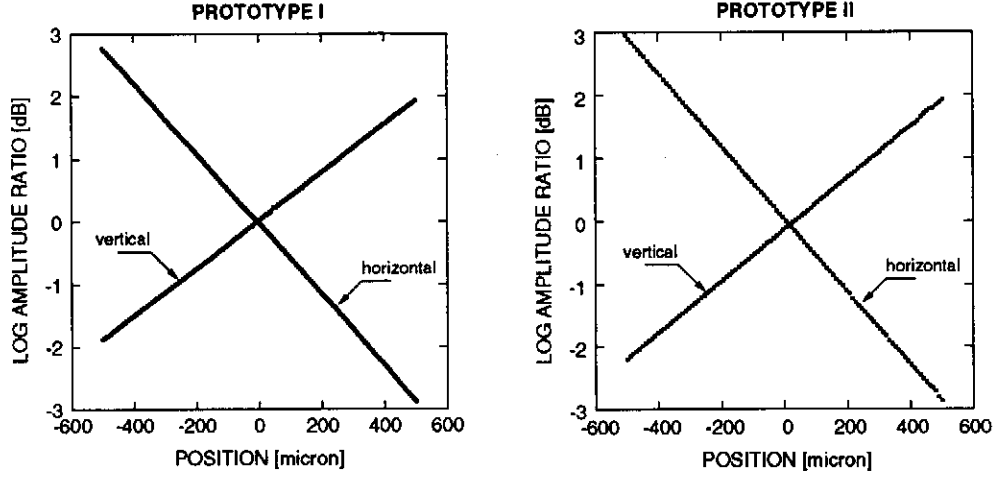


Figure 4.11: Sensitivity plots for both prototypes I and II. Mean errors for log-ratio values are for prototype I: 0.219 dB for the horizontal log-ratio values, 0.221 dB for the vertical; for prototype II: for the horizontal 0.107 dB and 0.106 dB for the vertical values.

The sensitivity was also simulated numerically with MAFIA S-Parameter computation and analytically with the wall current model. With MAFIA, transmission parameter were calculated for different positions of the inner conductor like described in previous section 3.3.3. In Tab. 4.5 results for simulations are gathered together with results from measurements

	$S_x \left[\frac{dB}{mm} \right]$	$S_y \left[\frac{dB}{mm} \right]$
Prototype I		
MAFIA simulation	5.41	4.25
Wall current model	5.67	3.89
Wire test bench	5.60	3.82
Prototype II		
MAFIA simulation	5.78	3.88
Wall current model	5.78	4.33
Wire test bench	5.79	4.10

Table 4.5: Comparison chart of sensitivities measured and calculated.

Both prototypes offer linear performance in a region $|x|, |y| \leq 500 \mu\text{m}$ around the center of the BPM. The relationship between induced voltages and beam offset is here simply given by the monitor constant.

4.2 Measurements with Beam at CTF2

First tests of prototype I with beam were performed at the CLIC (Compact Linear Collider [39]) Test Facility (CTF2 [40]) at CERN. The CTF2 was built to study the feasibility of the two-beam acceleration principle [41] with beam parameters close to those proposed for CLIC.

4.2.1 Measurement Setup

The CTF2 consists of two beamlines as illustrated in Fig. 4.12, a drive beam line to feed a probe beam line with energy. The drive beam accelerator structure can be subdivided into three sections: First an accelerating part based on normal conducting cavities working at 3 GHz able to accelerate the beam to an energy of 62 MeV, secondly a matching section to optimize the beam optics for the final transfer structures, where power is extracted from the beam and transferred by waveguides to the probe beamline. The prototype BPM was installed into the drive beamline as sketched in Fig. 4.12 behind the bunch compressor and matching quadrupole triplets.

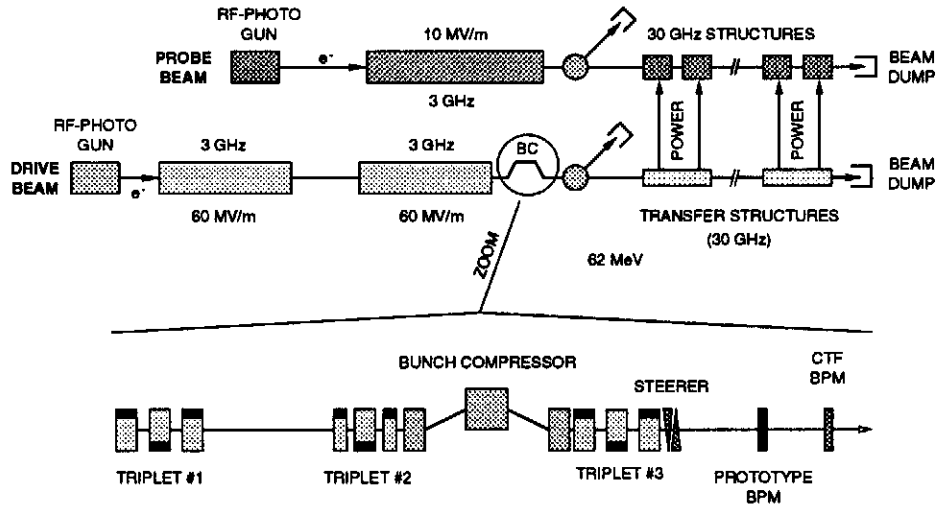


Figure 4.12: Schematic layout of the CTF2. In the bottom part of the figure the location of the prototype BPM in the drive beamline is zoomed.

Beam optics calculations with the purpose to find parameters suitable for BPM tests were carried out. The optics elements of the matching section were used to

focus the beam at the prototype's location. Using the software package WINAGILE [42] an optimized setup for the quadrupoles of the matching section was evaluated to get a small and round beam with root-mean-square transverse bunch dimensions of 1 mm in the region of the BPM. With these optic settings 99% transmission of electrons through the BPM region was reached.

4.2.2 Measurements

First measurements under real beam conditions were aimed at an experimental proof of the operation principle of the BPM. Furthermore, the coupling of the BPM to the beam field at 12 GHz was measured to compare with expectations from testbench measurements and calculations.

Beam parameters

Several beam parameters were measured to ensure correct steerer calibration and a center beam position at the BPM location. Energy measurements were performed using a spectrometer magnet located between the matching section and the transfer structures. Afterwards the beam was centered in quadrupoles positioned before and after the BPM with quadrupole scans. Beam parameters obtained and used during BPM measurements are listed in Tab. 4.6. Compared

Energy	E	51.2 MeV
Repetition rate	f_r	5 Hz
Bunch charge	q	3 nC
Bunch length	σ_z	10 ps

Table 4.6: Beam parameters during measurements with the prototype BPM.

to TTF FEL design parameters, the bunch charge at the CTF2 is by a factor of three higher and spread on a ten times longer bunch. A position jitter of at least 50 μm was observed at the CTF BPM located directly behind prototype BPM. Furthermore, intensity fluctuations of around 10% of the mean bunch charge were measured by toroid signals. Since no fast signal processing electronics were available, measurements were averaged over many bunches resulting in a large error for the estimated position of at least 100 μm .

Signal line

Each element in the signal processing line was characterized with respect to its loss parameters to enable an accurate estimate of the signals induced into the BPM channels. In Fig. 4.13 a block diagram of the signal processing elements is shown. The damping of the induced signals caused by losses in cables are in the

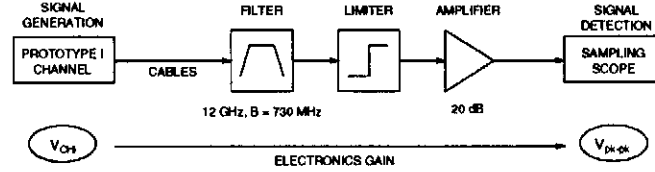


Figure 4.13: Block diagram of tested prototype I electronics.

order of $L = (32 \pm 1)$ dB for all cables including connectors. For the distance between accelerator tunnel and control room lowloss cables of 0.5 m length with damping coefficient of $D = 1$ dB/m at 12 GHz were used for the first part of the way. These were the same cables as used with the wire testbench. For the rest way, 10.7 m long cables ($D = 10$ dB/m at 12 GHz) were utilized. An additional damping element with $L = 20$ dB was first installed to protect the amplifier from high signal amplitudes. This results in an electronic gain factor a_i which is unique for each channel.

Coupling

A digital sampling oscilloscope¹⁰ was used to display signals. Fig. 4.14 shows an example of measured amplitudes in the time-domain. Detected peak to peak voltages $V_{pk-pk,i}$ have to be transformed into root-mean-square voltages $V_{rms,i}$ with $V_{rms,i} = V_{pk-pk,i}/2\sqrt{2}$. Using the known characteristics of the signal carrying and processing elements the induced voltage V_i at the vacuum feedthrough of the i th channel can be computed using

$$V_i = a_i \cdot V_{rms,i}. \quad (4.14)$$

From this, the coupling parameter k_i for this channel can be determined as

$$k_i = \frac{V_i}{Z \cdot B_e \cdot q}. \quad (4.15)$$

In Tab. 4.7 these values are compared with values obtained under laboratory conditions with the wire testbench. There is a good agreement between both data sets within error margins.

¹⁰Tektronix 11801B

118018 DIGITAL SAMPLING OSCILLOSCOPE
 date: 25-NOV-97 time: 17:55:08

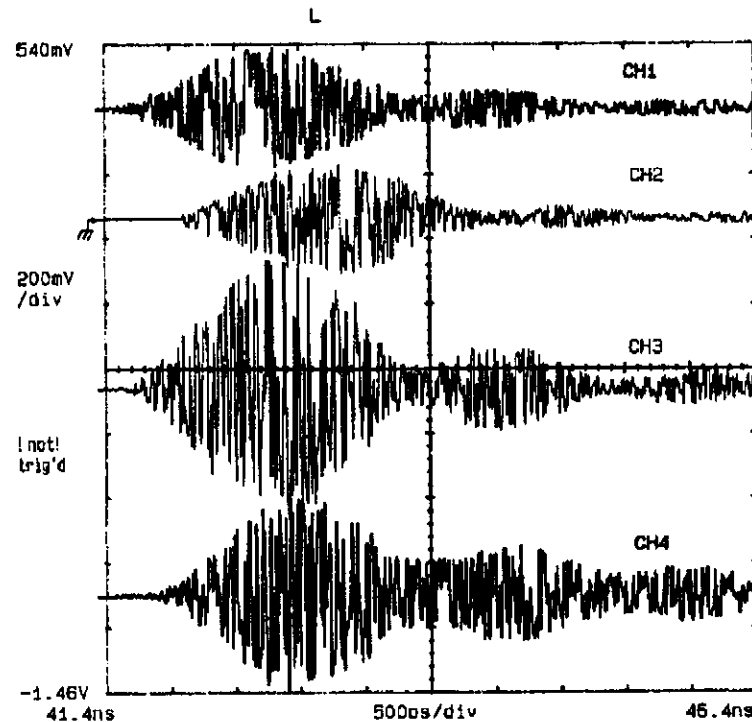


Figure 4.14: Signals of all channels measured using a digital sampling oscilloscope. Transduced signals were filtered and amplified. The peak to peak voltage values for the different channels are, from top to bottom: CH1: 364 mV, CH2: 334 mV, CH3: 804 mV and CH4: 588 mV. Note that the scaling is different for each signal.

Steering

Steering experiments have been performed with the CTF2 electron beam. Using a pair of correction coils the beam was moved in both transverse directions. Before beginning of steering the beam was centered with quadrupole scans. Then the beam was steered in x and y direction perpendicular to the beam axis, and output signals were detected with the digital sampling scope. In accordance with the coupling parameter measurements these output signals were traced back to the transducer. From a data table containing the induced voltages for every channel per beam position affiliated beam positions were calculated using a beam based model fit technique¹¹.

¹¹This technique will be discussed in chapter 5 dealing with calibration techniques.

	Coupling k_i	
	CTF2	Lab
CH1	1.00 ± 0.10	1.0000 ± 0.0018
CH2	0.56 ± 0.06	0.5609 ± 0.0011
CH3	0.30 ± 0.03	0.3273 ± 0.0006
CH4	0.63 ± 0.06	0.6922 ± 0.0014

Table 4.7: Coupling parameters obtained at CTF2 and with the wire testbench. Values are normalized to the channel 1 amplitude.

First results revealed a systematic offset between set and measured values (see Fig. 4.15a. This offset is $x_{off} = (-515 \pm 20) \mu\text{m}$ for the horizontal and $y_{off} =$

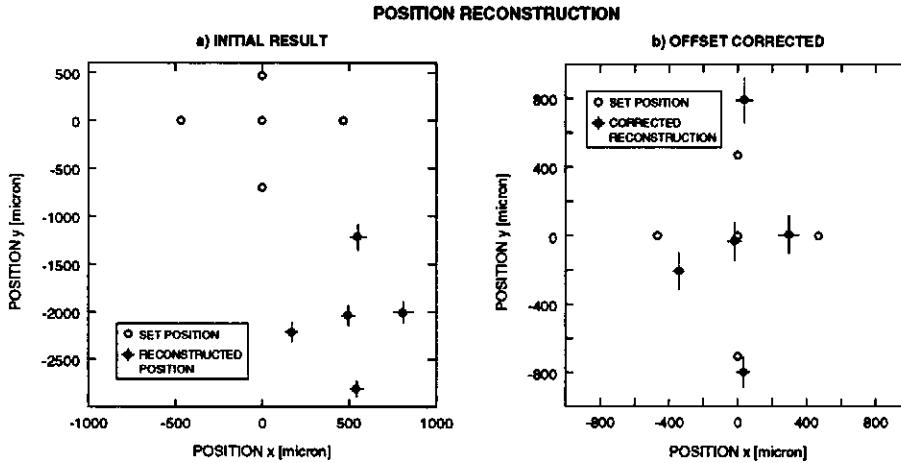


Figure 4.15: Comparison between set beam position and reconstructed beam positions. a) Uncorrected reconstruction results are plotted together with set positions. b) Corrected reconstruction results and set beam positions.

$(2011 \pm 40) \mu\text{m}$ for the vertical direction with statistical errors. Fig. 4.15b shows for this offset corrected position values. This indicates that the BPM was not well aligned in the beamline. The remaining difference between set and reconstructed position is still in the order of a $\pm 200 \mu\text{m}$. This is due to the finite size of the beam in transverse plane exceeding the linear range of the BPM.

Taking only difference measurements into account for estimating the sensitivity, this results in values close to those estimated with the wire testbench as shown in Tab. 4.8.

	CTF2 Beam	Wire Testbench
S_x [dB/mm]	5.58 ± 0.09	5.597 ± 0.078
S_y [dB/mm]	3.86 ± 0.12	3.815 ± 0.077

Table 4.8: Comparison between sensitivities obtained at CTF2 and in lab at Zeuthen.

Measurements with the CTF2 electron beam and with the wire testbench are consistent regarding the coupling amplitude and the sensitivity of the BPM. They also agree with estimates from analytical calculations and from MAFIA simulations.

4.3 Measurements with Beam at SBTF

To reduce the number of systematic error sources and to move the BPM in well-defined stepwidth a setup with two stepping motors was planned for prototype II tests at the S-Band Test Facility (SBTF) [43].

4.3.1 Setup and Preparatory Work

The SBTF was a teststand for a linear electron-positron collider based on normal-conducting cavities working in the S-Band ($2.60 \dots 3.95$ GHz) with a resonant frequency of the accelerating mode in a cavity of 2.99 GHz [4]. The accelerator design is based on well known and proven technology, with focus on the generation [44] and transport [45] of RF power in the S-Band, as well as on Higher Order Modes (HOM) issues [46].

The BPM prototype II was installed in the SBTF beamline in a drift region between two quadrupole triplets as illustrated in Fig. 4.16. In the injector complex

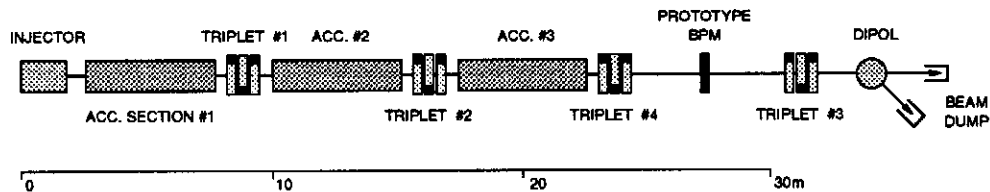


Figure 4.16: Layout of the S-Band Test Facility (as in 9/98) with indicated location of the BPM prototype II .

an electron beam with the desired time structure and energy is generated to be accelerated by three adjacent accelerating sections, each 6 m long and composed by copper cavities. The prototype II BPM was installed between the third and fourth quadrupole triplets, at a location where the beam envelope should be equal for the horizontal and vertical plane. The BPM was fixed to a two-dimensional stepping motor frame enabling the movement of the BPM in a plane normal to the beam axis. In order to catch up mechanical stress on the beam pipe and on the BPM, two pairs of bellows were installed in front and after the BPM as shown in Fig. 4.17. In Tab. 4.9 SBTF beam parameters relevant for the BPM

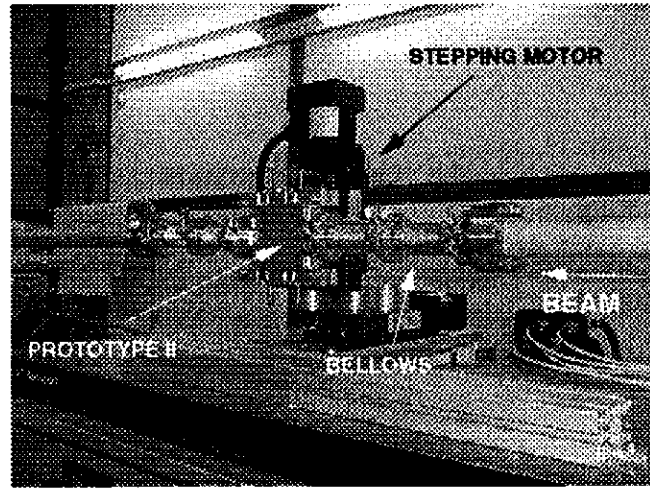


Figure 4.17: Photo of the direct neighborhood of the BPM prototype II in the SBTF beamline.

Energy	E	46.7 MeV
Repetition rate	f_r	1 Hz
Bunch charge	q	0.2 nC
Bunch length	σ_z	4...5 mm
Bunch size	$\sigma_{x,y}$	~ 1 mm

Table 4.9: SBTF beam parameters during measurements with prototype II.

tests are summarized. After centering the beam with quadrupole scans, first measurements were performed by simply displaying beam induced signals on a digital sampling scope.

4.3.2 Measurements

Raw BPM Signals

For first measurements, the induced signals were displayed directly on a digital sampling oscilloscope (see Fig. 4.18a). For the scope trigger, a beam related signal was taken from a stripline BPM in the second quadrupole triplet. In order

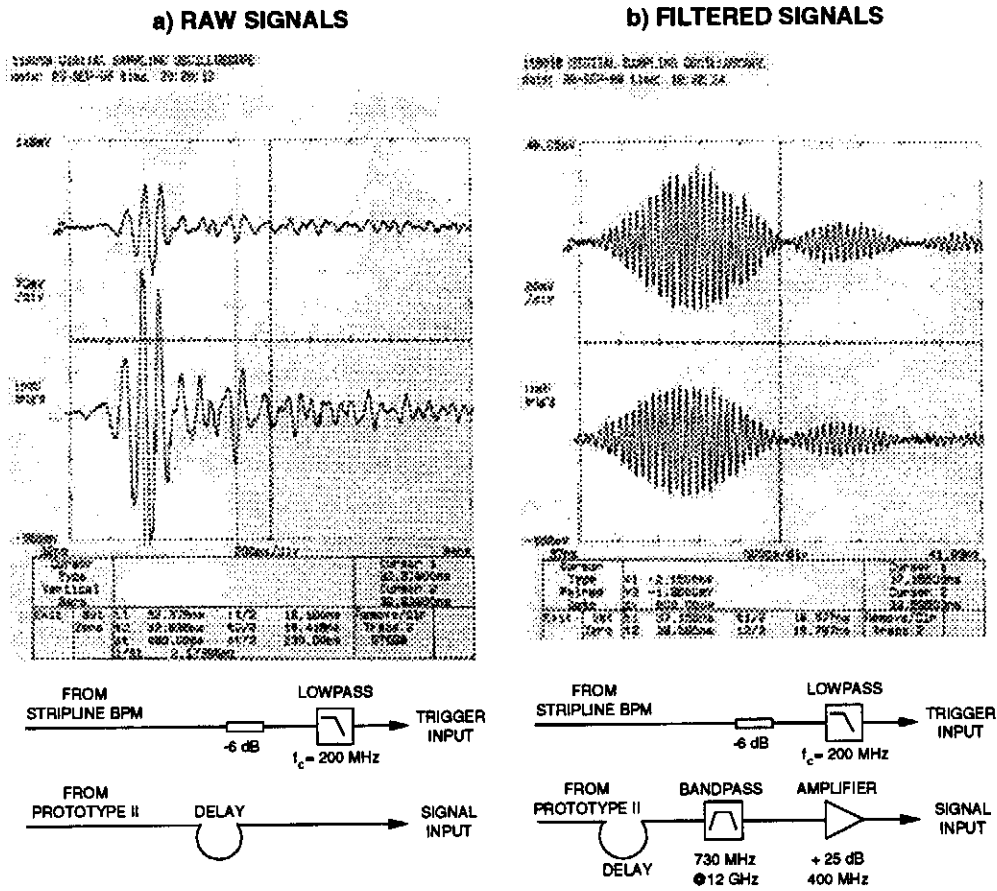


Figure 4.18: Measurements with a digital sampling scope. a) Raw signals for two BPM channels. b) Two BPM signals filtered and amplified at 12 GHz.

to shift the prototype II signal in time after the trigger signal, a delay had to be incorporated. To filter out unwanted frequencies, a filter element was placed in the signal line before the input port of the the sampling scope (see Fig. 4.18b). With this setup, the 12 GHz component of the beam position related induced signal at the BPM was clearly visible. Hence the trigger signal from the stripline BPM proved to be very stable in time and amplitude. Encouraged by this it was

planned to build a simple signal processing electronics by commercially available elements, since the recording of one BPM channel signal took around 10 min which is too long for steering experiments, as beam position jitter and intensity fluctuations add up during this time.

Utilizing Signal Processing Electronics

With the next step it was planned to record down-converted BPM signals enabling measurements with a fast oscilloscope for all channels simultaneously. The down-conversion from 12 GHz to DC was realized using a RF mixer. The filtered amplified signals coming from the waveguide BPM were fed into the RF-port of a mixer. For down-conversion a local oscillator signal (LO) signal is needed with constant amplitude, a frequency of 12 GHz, and which is phase-locked to the beam. Since the operation frequency of the SBTF is $f_{HF} = 2.99$ GHz the fourth harmonic of this frequency, stabilized in amplitude, should be sufficient for this purpose. A fourth harmonic at 12 GHz was found in the spectra of the stripline-monitor that was used to trigger the sampling scope. After filtering out any unwanted frequencies the LO-signal was amplified to a level of $U_{LO} = \pm 1$ V. A block diagram is sketched in Fig. 4.19. Electronics of this kind were built for each of the four channels providing the opportunity to measure all four signals at the same time. The resolution of the BPM is here only limited by the resolution of the oscilloscope analog-to-digital converter (ADC). Transforming the 8 bit resolution into position resolution results in a minimal measurable offset of $30 \mu\text{m}$.

Steering

With the electronics described in the previous section, beam offset measurements with respect to the BPM center were performed in a transverse reference frame spanned out by the two stepping motors. Scans along the vertical axis were impossible due to a system failure of one stepping motor. After correcting for gain and damping factors, the signalfunction S_x for the horizontal plane was calculated with the sum-over-difference method. In Fig. 4.20 S_x is plotted versus the transverse beam position for a rough scan with stepwidth $\Delta x = 500 \mu\text{m}$ and a fine scan around the BPM center with $\Delta x = 50 \mu\text{m}$. The trend of the broad scan data can be described with a theoretical model based on the image charge calculation (see Appendix A for this model). From data values obtained from the fine scan, confined inside the linear region of the BPM, the horizontal sensitivity

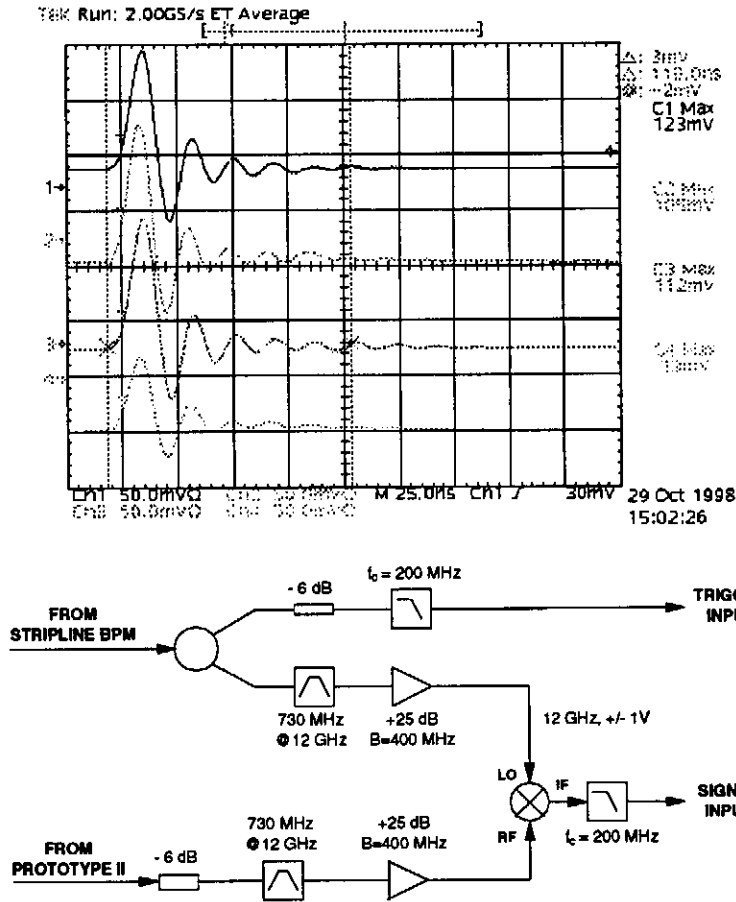


Figure 4.19: Top: Induced and down-converted BPM signals for all four channels. Bottom: Block diagram for one channel signal processing electronics.

can be derived using a linear fit resulting in a sensitivity of

$$S_x = (5.27 \pm 0.14) \text{ dB/mm.}$$

Compared with the value measured with the wire testbench of

$$S_x = (5.786 \pm 0.037) \text{ dB/mm,}$$

the sensitivity measured at SBTF under beam conditions is lower. This can be explained by the fact that the beam size is larger than the linear region of the BPM, so that a fractional part of the transverse beam profile will lap into the saturation regime of the BPM, giving a lower signal than expected from an extrapolation of the linear region. This behavior is illustrated in Fig. 4.21 where signal functions derived from the image charge model and the linear approximation are compared.

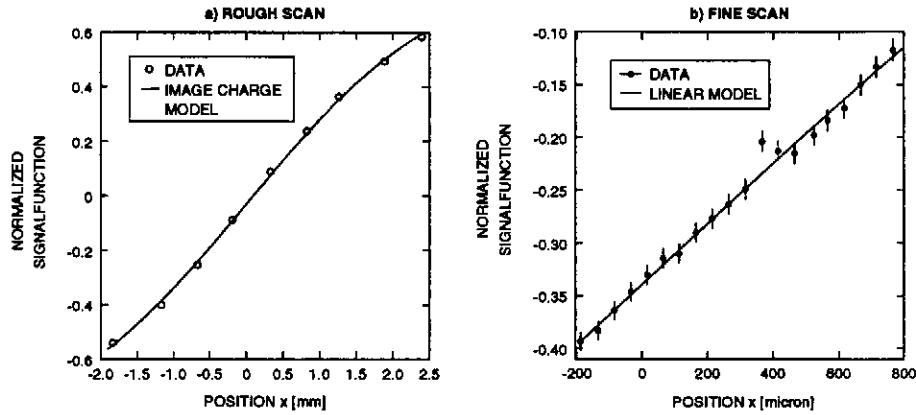


Figure 4.20: a) Relative signalfunction for the horizontal plane for a broad scan with stepwidth $\Delta x = 500 \mu\text{m}$. b) For a narrow scan with stepwidth $\Delta x = 50 \mu\text{m}$. From the right plot the sensitivity for the linear region was derived. Excluded for this analysis were three values around $400 \mu\text{m}$ offset because strong position jitter occurred due to machine problems.

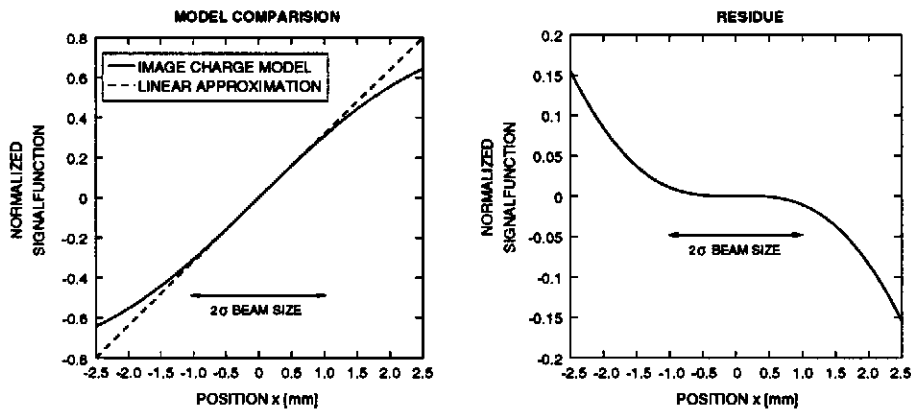


Figure 4.21: Comparison between signalfunctions derived with the image charge model and with the linear approximation. Also illustrated is the 2σ beam size in the transverse plane.

Chapter 5

Calibration Techniques

There are ten waveguide type beam position monitors installed in the third undulator module of the Tesla Test Facility FEL. Due to mechanical tolerances and manufacturing aspects each of the 40 BPM channels has unique properties affecting the performance of them. Therefore each BPM head as well as each BPM channel is object to calibration in order to establish a defined relationship between induced signals and beam position [47]. This chapter summarizes different calibration methods, feasible in lab or with beam under operation conditions. Furthermore concepts are evaluated to calculate beam position from induced voltages.

5.1 Motivation

Each BPM head as well as each BPM channel has specific properties which have to be determined in order to establish the relationship between induced signals and the absolute beam position with respect to a nominal orbit.

Absolute calibration requires several steps during machine operation and should be repeated regularly to overcome drifts due to changes in the accelerator environment. The steps required to relate the measured positions with respect to a nominal orbit defined by a global survey are:

- Measure and correct for attenuation of the signals through cables, connectors, passive and active electronics elements.
- Establish the electrical center of the BPM with respect to a the geometrical center as discussed in the section 5.3.

- Determine the offset of the electrical BPM center with respect to its associated quadrupole axis using a method described in section 5.4
- Align the beam in a straight line through undulator structure by using BPM information and defined corrector settings obtained with a technique described in section 5.5.

5.2 Modelling BPM Output Signals

A practical model is proposed to describe the response of a BPM channel, and define the geometrical monitor center by assuming that each coupling channel has its ideal position response function. This model also assumes that the real output from a coupling channel is proportional to its response function by a constant factor, called its gain, and that the gain is independent of the beam position.

5.2.1 Recalling the Image Charge Model

The response of an ideal BPM channel according to design specifications can be modelled using a model based on the calculations of image charge from offset beam currents (see Appendix A for details.)

The closed form expression for the local transverse magnetic field amplitude H_t for a beam current I_b at (θ, r) detected by a slot centered at (ϕ, b) in a beam pipe with radius b reads

$$H_t = H_o \cdot \frac{b^2 - r^2}{b^2 + r^2 - 2br \cos(\phi - \theta)}. \quad (5.1)$$

Divided by the magnetic field for a centered beam

$$H_o = \frac{I_b}{2\pi b} \quad (5.2)$$

one yields an expression for the relative position response function of the i th BPM channel with

$$S_i = \frac{b^2 - (x^2 + y^2)}{b^2 + (x^2 + y^2) - 2(x_s x + y_s y)} \quad (5.3)$$

in a cartesian reference frame. Beam and slot coordinates are transformed with

$$\begin{aligned} x &= r \cdot \cos(\theta), & x_s &= b \cdot \cos(\phi), \\ y &= r \cdot \sin(\theta), & y_s &= b \cdot \sin(\phi) \end{aligned}$$

from cylindrical to cartesian coordinates.

5.2.2 From Ideal to Real BPM Heads

Because of mechanical tolerances and possible errors during the production process of the BPM heads, each channel will have its own individual transfer characteristics. Furthermore, each BPM channel will be connected to its own chain of signal processing electronics elements, cables, and connectors. Thus the above mentioned position response for an ideal BPM channel will differ from the response of a real BPM channel. Assuming a linear relationship between the real and the ideal response, all effects can be summarized in a gain factor g_i which is unique for each channel. The characteristics of each BPM head can be specified by four gain factors, which are object of intrinsic BPM calibration. Fig. 5.1

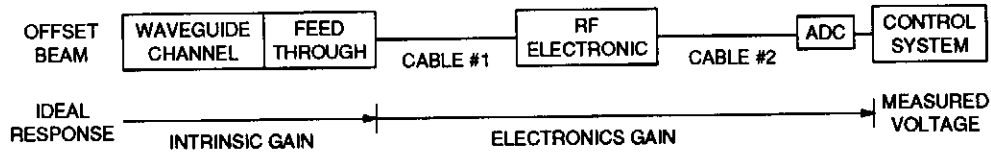


Figure 5.1: The ideal response due to an offset beam will be modified according to intrinsic and electronic gain factors.

describes schematically the modification of the ideal response with gains. One can subdivide the gain factor g_i into intrinsic and electronics gain factor, because the electronics gain can be measured separately without beam by using a precise and well defined signal source and a precision voltmeter. With such a setup time-varying changes and drifts inside the electronics chain can be detected and corrected for. Moreover, in the following the gain g_i refers to the overall gain. Thus the measured voltage V_i for each channel depends on the ideal response function S_i modified with the channel gain g_i and on the bunch charge q to

$$V_i = q \cdot g_i \cdot S_i. \quad (5.4)$$

The gains g_i are in the following object of calibration.

5.3 Beam Based Model Fit

In this section a method is discussed to find the geometrical center of a BPM from its beam signals and thus calibrate the BPM for the imbalance between its gain factors.

5.3.1 Assumptions

The analysis is based on two assumptions. One is that the response function S_i for a particular channel will not change in time and is known by calculation. The second assumption is that all effects determining the coupling gain of one channel can be summarized by a gain factor g_i [48]. Measured independently are parameters for the signal processing electronics.

5.3.2 Gain Detection

Considering $j = 1 \dots m$ different measurements of four induced voltages with different beam positions measurements, for example by steering. Then, the measured voltage of the i th channel at the j th measurements is given by

$$V_{ij} = g_i \cdot q_j \cdot S_i(x_j, y_j) \quad (5.5)$$

where S_i is the response function for an ideal BPM channel for an electron beam at the position (x_j, y_j) :

$$S_i(x_j, y_j) = \frac{b^2 - (x_j^2 + y_j^2)}{b^2 + (x_j^2 + y_j^2) - 2(x_s x_j + y_s y_j)} \quad (5.6)$$

Because only the relative imbalance between all gains are of interest for calibration, g_1 can be set to 1. So there exist only three unknown parameters g_2 , g_3 , and g_4 . Beside this, for each measurement m a set of 3 unknown parameters (q_j, x_j, y_j) exists while four quantities $(V_{1j}, V_{2j}, V_{3j}, V_{4j})$ are measured. For $m = 3$ measurements the system of equations has a unique solution, for $m \geq 4$ the number of known parameters exceeds the number of unknowns because of

$$4m > 3 + 3m \quad \text{for} \quad m \geq 4 \quad (5.7)$$

Using a nonlinear multi-parameter chi-square method the unknown parameters, including the gains, can be estimated. The present nonlinear model can be rewritten as

$$\begin{aligned} V_{ij} &= g_i \cdot q_j \cdot S_i(x_j, y_j) \equiv V(i, j; \mathbf{a}) \\ i &= 1 \dots 4 \quad \text{and} \quad j = 1 \dots m \\ \mathbf{a} &= (g_2, g_3, g_4, q_1, x_1, y_1, \dots, q_m, x_m, y_m) \end{aligned}$$

where \mathbf{a} is an array of the parameters to be fitted. The unknowns can be estimated by minimizing the chi-square defined as

$$\chi^2(\mathbf{a}) = \sum_{i=1}^4 \sum_{j=1}^m \frac{[V_{ij} - V(i, j; \mathbf{a})]^2}{\sigma_{ij}^2} \quad (5.8)$$

where σ_{ij}^2 is the data error of the i th channel at the j th measurement and is assumed to be equal for all measurements and thus can be neglected.

5.3.3 Simulation of the Method

For simulations a data field was generated using the closed-form expression for the signal function as in Eq. 5.5 with reasonable set values for the gains as well as for the beam charge and displacement. The relative gains (g_2, g_3, g_4) are typically in an interval $0.5 < g_i < 1.5$. Furthermore noise was added to the simulated data points in form of a flat distribution simulating noisy measurements. A set of beam positions was fixed using a random walk through the monitor plane in a square region around the monitor center with a side length of 2 mm. Estimation of the gains and beam positions were carried out, based on the generated data, by minimizing the chi-square defined in Eq. 5.8 with a Marquat-Levenberg-Minimization techniques [49] implemented into the MATLAB [50] programming package. With this algorithm convergence was always reached in a few iterations and the results coincided with the set values.

5.3.4 Test with Measured Data

The method described above was also tested with a data field obtained during wire measurements with the testbench setup for the second prototype. From a square data field with side length of $L_{x,y} = 1.2$ mm and step width of $\Delta x, y = 20$ μm 5, 9, and 12 points randomly selected measured voltage values for this points were extracted and sent to the solving algorithm. In total 30 seeds were tested in this way, and convergence in the minimization procedure was always reached. Also there was no relationship found between start values for the algorithm and solutions.

As illustrated in Fig. 5.2, a systematic offset occurs between estimated and set values for the wire positions. This offset is $x_{off} = (118 \pm 19)$ μm for the horizontal and $y_{off} = (15 \pm 11)$ μm for the vertical direction. The reason for this systematic deviation is the way the reference frame for the set values was determined. Due to the lack of a precise survey instrument, the wire position at the BPM center was zeroed empirically. This causes an offset between the real and the set reference frame. Assuming that the fit algorithm estimates wire positions in a real reference frame, the set values can be corrected. Fig. 5.3 shows results for an 8 and 12 point randomly drawn from the data field. The mean difference between corrected reconstruction and set position is $\bar{\sigma} = 8$ μm and the mean error for the offset

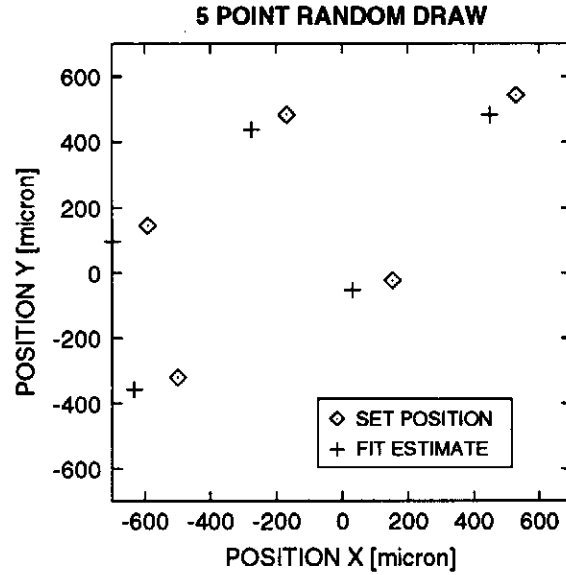


Figure 5.2: Fit result and set values for a 5 point random walk; the fit estimation for wire position were not corrected by the offset of the reference frame.

estimation is $\bar{d} = 15 \mu\text{m}$. This leads to a error of $\bar{\sigma}_{tot} \geq 17 \mu\text{m}$ for directions. The results for the estimated gain factors and charge are listed in Tab. 5.1 The

Quantity	Value		
g_2	1.1920	\pm	0.0143
g_3	0.7684	\pm	0.0115
g_4	0.9705	\pm	0.0059
q	88.7	\pm	0.6

Table 5.1: Results for the gains g_i and the bunch charge parameter q .

errors are less than 2%. Tests with simulated data fields as well as with measured values taken from testbench measurements show that the fit procedure is useful to describe the real BPM heads with only a few parameters where more than five measurements at different beam positions are taken into account.

5.4 BPM Offset Determination

Beam based alignment techniques as described in the following section 5.5 eliminate the need for a high accuracy pre-alignment of the BPMs in the order of

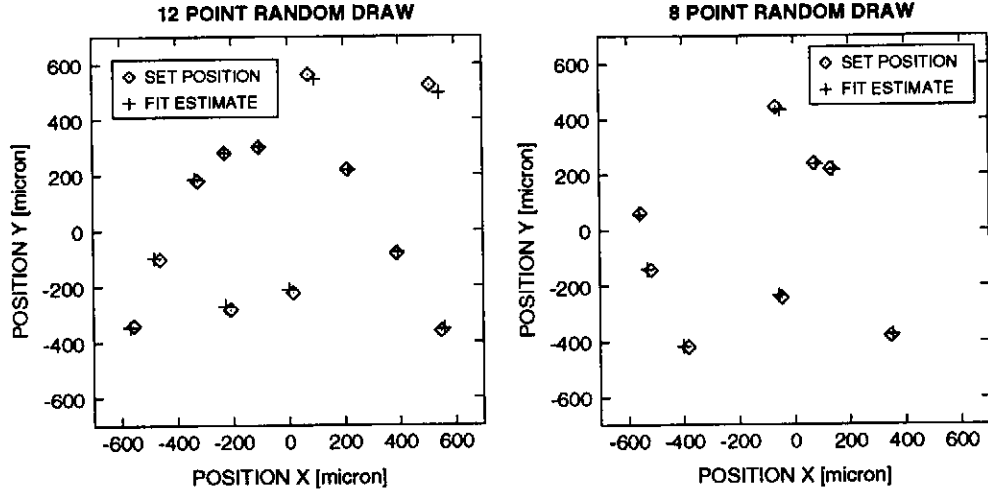


Figure 5.3: Fit estimate and set values for a 8 and 12 point random draw. In both cases corrections for reference frame offset were applied.

a few μm . Despite that an absolute BPM measurement accuracy of a few ten μm after initial BPM offset determination is desired to reduce the beam based alignment time and to achieve FEL gain at low electron energies without that procedure. Therefore the offset between the geometrical center of each BPM with respect to its associated quadrupole has to be determined.

Parameters influencing the position measurement accuracy are misalignments of quadrupoles and the beam chamber (with its BPMs), and mechanical tolerances of the extruded central aperture. The undulator is a permanent magnet structure with a gap of 12 ± 0.2 mm, the height of the vacuum chamber is 11.5 mm with negligible tolerances [37]. The quadrupoles can be aligned with a precision of ± 0.05 mm [51]. For the horizontal plane, additional errors arise from the wander of the extruded central aperture of ± 0.3 mm and from the horizontal alignment of the vacuum chamber in the order of ± 0.5 mm [52]. Combining all factors results in a root-mean-square deviation between quadrupole and BPM center of $d_{rms} = 0.63$ mm, which is also the initial accuracy. In the following a method is reviewed improving this initial accuracy. The method utilizes orbit measurements at different energy levels [53] aiming at minimum local dispersion at each BPM. This offset information is then the base for an improved trajectory correction [54].

5.4.1 Local Orbit Correction

In case of the FEL the aim is to keep the electron beam on a straight line in order to maximise the interaction between photon and electron beam. This straight line is defined by the beam parameters (x_o, x'_o, y_o, y'_o) at the entrance of the undulator. As a dominating source for orbit kicks misaligned quadrupoles are expected, while dipole field errors are considered to be significant smaller. Since all dipole as well as the quadrupole magnets are made of permanent magnets, only the corrector magnets and the beam energy can be changed, making BPM offset detection schemes [55] using variable quadrupoles [56] impossible.

In Fig.5.4 the situation at the first half FODO-cell of the undulator is illustrated. The beam position x_1 at the BPM located in the next quadrupole center can be

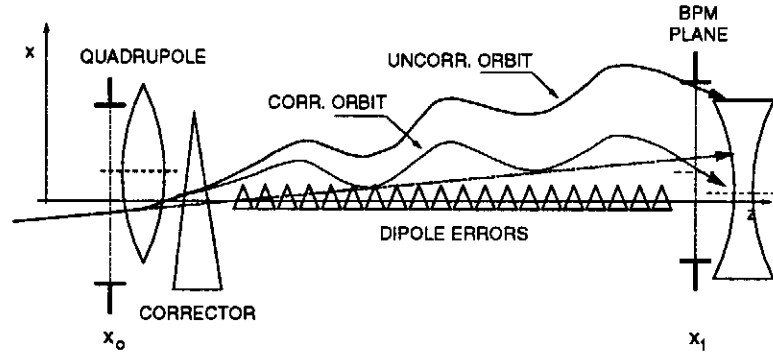


Figure 5.4: Sketch of corrector compensation of the beam deflection due to quadrupole and dipole field errors. BPMs are located at the center of quadrupoles.

expressed in the thin lens approximation for the horizontal plane by

$$x_1 = x_o + x'_o \cdot z + \frac{K_q}{p} \cdot z_q + \sum_i \frac{D_i}{p} \cdot z_i + \frac{C}{p} \cdot z_c \quad (5.9)$$

where (x_o, x'_o) are the initial beam conditions, K_q the kick generated by the misaligned quadrupole, D_i the kicks caused by dipole errors, and C the kick produced by the corrector. The beam momentum is denoted with p and z , z_q , z_i , and z_c indicate the position of the beamline elements with respect to the BPM at z_1 . To bring the beam onto a straight line with $x_1 = x_o + x'_o \cdot z$, the sum of all kicks has to be zero. This is the case when the measured beam position at the z_1 is energy independent or in other words dispersion-free. To determine the required excitation of the corrector to cancel the effects of all field errors one needs to measure the beam position x_1 as a function of the excitation for two different

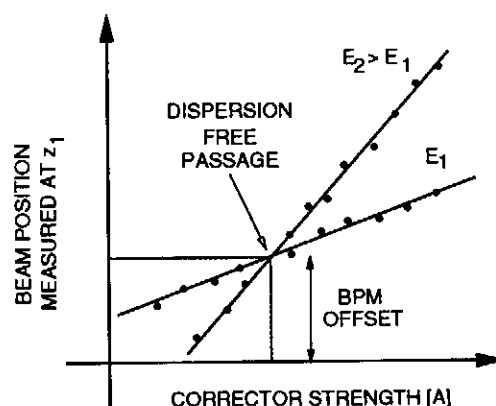


Figure 5.5: Schematics for two different orbit measurements at two different beam energies.

energies with typically 10 % energy variation [57]. Then the BPM readout x_1 has to be plotted versus the excitation current of the corrector as illustrated in Fig. 5.5. A linear regression gives two lines describing the dependence of the beam position for different corrector settings. This plot gives valuable information: The intersection of the two regression curves indicates the working point for a dispersion-free passage of the electron through the beamline. The projection onto the corrector setting axis reveals the correct setup for this element, while the projection onto the BPM readout axis shows the offset of the electrical BPM center with respect to the quadrupole center in the horizontal direction. The method works similar for the vertical direction.

5.5 Beam Based Alignment

In addition to the technique discussed above working with a point-to-point steering an orbit alignment method using global dispersion minimization [58] is briefly reviewed here. This method utilizes BPM readout information and corrector settings from all elements along the undulator beamline. While quadrupole misalignments and undulator field errors not only deflect the beam they also introduce dispersion. The idea behind global dispersion minimization is that a dispersion free trajectory is in first order a straight line.

5.5.1 Global Dispersion Correction

The dispersion orbit is obtained as the difference between two orbit measurements at different energy level (E and $E - \Delta E$) of the electron beam. With subtracting these two measurements one gets a so-called dispersion orbit which describes the energy-dependence of the particle trajectory. This difference measurement is independent of the absolute BPM alignment, since only relative beam offsets are taken into account for the analysis. The problem here is to find a set of corrector settings which corrects to zero the dispersion observed at all BPMs. This can be expressed as the following system of linear equations

$$d_i + \sum_{j=1}^{N_{\text{corr}}} a_{ij} c_j = 0 \quad \text{for} \quad i = 1, \dots, N_{\text{mon}} \quad (5.10)$$

where N_{mon} denotes the number of BPMs and N_{corr} the number of correctors. The vector c_j represents the corrector strengths to be evaluated and the vector d_i is given by the measured dispersion at the i th BPM. The correction matrix a_{ij} is calculated as

$$a_{ij} = \left. \frac{Dx_i(E - \Delta E) - x_i(E)}{\Delta E/E} \right|_{c_j=1} \quad (5.11)$$

where x_i is the beam displacement due to the corrector c_j and ΔE is the energy change used for the dispersion measurement. The Micado [59] algorithm is used to find a set of *best correctors* which minimizes the chi-square defined as

$$\chi^2 = \sum_{i=1}^{N_{\text{mon}}} \left(d_i + \sum_{j=1}^{N_{\text{corr}}} a_{ij} c_j \right)^2 \quad (5.12)$$

Both location and resolution of the BPM system are key parameters for the efficiency of the correction scheme. It has been concluded from simulations [60] that the last three BPMs inside the last undulator module are needed to reduce the root mean square orbit deviation to a level of $\Delta x_{\text{rms}} = 11 \mu\text{m}$. Furthermore the performance of the correction scheme is related to the BPM resolution. For a larger ΔE the effect of position measurement resolution is reduced. For example with 300 MeV beam energy and $1 \mu\text{m}$ BPM resolution the energy shift has to be in the order of $\Delta E/E = 0.20$. If the BPM resolution is around $3 \mu\text{m}$, the required energy shift increases to $\Delta E/E = 0.30$.

5.6 Beam Position Determination

In this section combinations of response functions of the four coupling channels are investigated to obtain an algorithm to determine the beam position in units of μm from induced voltages.

5.6.1 Normalized and Skew Differences

Fig. 5.6a shows that by measuring only the response of one channel, S_1 (also denoted as UR^1) for example, and normalizing it to the beam intensity, one only knows that the beam position is on a given curve in the (x, y) -plane. By combining two signals in a well defined way, like in Fig. 5.6b, one gets a signal proportional to the offset in the vertical direction, but which has however an up-down ambiguity. In order to get rid off all ambiguities, it is necessary to combine all four signals in both horizontal and vertical directions to extract relevant beam position information. The most obvious combination of the four channel signals

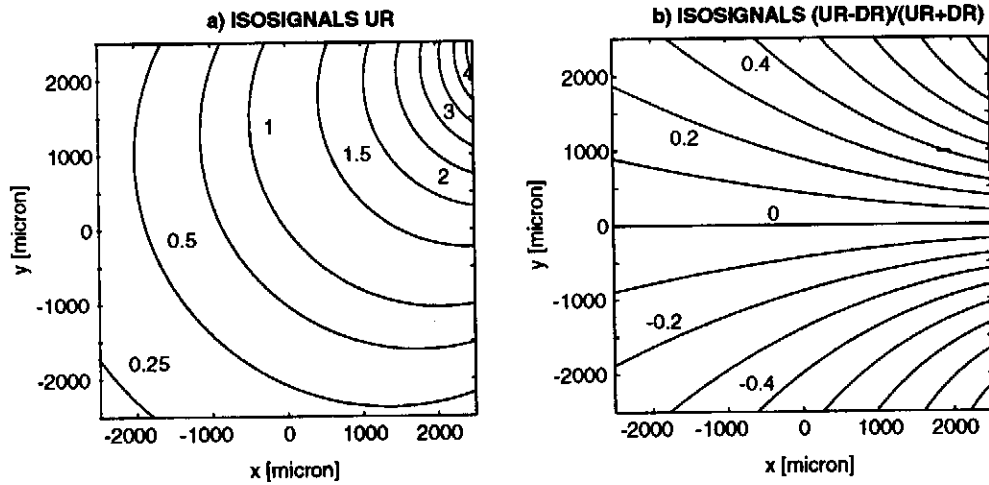


Figure 5.6: a) Isosignal curves for one coupling channel, here S_1 (UR).
b) Difference of two signals useful to derive position information in the vertical direction.

to extract the beam position is to use combined Up and Down, respectively, Left and Right signals

$$\begin{aligned} L &= UL + DL, & R &= UR + DR, \\ U &= UL + UR, & \text{and } D &= DL + DR. \end{aligned}$$

¹This notation is introduced because the BPMs installed in the FEL are named according to this convention.

The signalfunctions for the x and y -direction are then defined as

$$F_x = \frac{R - L}{R + L} \quad \text{and} \quad F_y = \frac{U - D}{U + D} \quad (5.13)$$

In Fig. 5.7a the signalfunctions F_x and F_y are shown for a region of $\Delta x = \Delta y = 2.5$ mm around the BPM center. Another possibility to combine response functions created by combinations of the diagonal signals like

$$P = \frac{UL - DR}{UL + DR} \quad \text{and} \quad S = \frac{UR - DL}{UR + DL} \quad (5.14)$$

and to form the skew differences

$$D_x = S - P \quad \text{and} \quad D_y = P + S \quad (5.15)$$

Isosignal curves for D_x and D_y are illustrated in Fig. 5.7b. The slope of the signalfunctions obtained using skew differences is higher, thus indicating a higher sensitivity of these signalfunctions and in consequence a higher robustness against fluctuations in the induced signals caused by gain variations of signal processing elements. This is illustrated in Fig. 5.8. The slope of the signalfunction calculated with skew differences is higher than the slope of the curve for normalized differences .

5.6.2 Linearization of Signalfunctions

In order to reconstruct the beam position from signalfunctions generated by normalized or skew differences several methods have been studied. Short computation time and low error margins are boundary conditions for a reconstruction algorithm.

One possibility is to use a polynomial of higher order to describe the relationship between signalfunction and beam position. For a first approximation, a linear fit in a region $|x|, |y| \leq 500 \mu\text{m}$ results to first order coefficients $b_{x,y}$ and $c_{x,y}$ relating the signalfunctions to beam positions according to

$$\begin{aligned} x_1 &= b_x \cdot F_x & \text{or} & & x_1 &= c_x \cdot D_x, \\ y_1 &= b_y \cdot F_y & \text{or} & & y_1 &= c_y \cdot D_y \end{aligned} \quad (5.16)$$

with

$$\begin{aligned} b_x &= 2.9559 \text{ mm} \\ b_y &= 4.0684 \text{ mm} \\ c_x &= 1.4779 \text{ mm} \\ c_y &= 2.0342 \text{ mm}. \end{aligned}$$

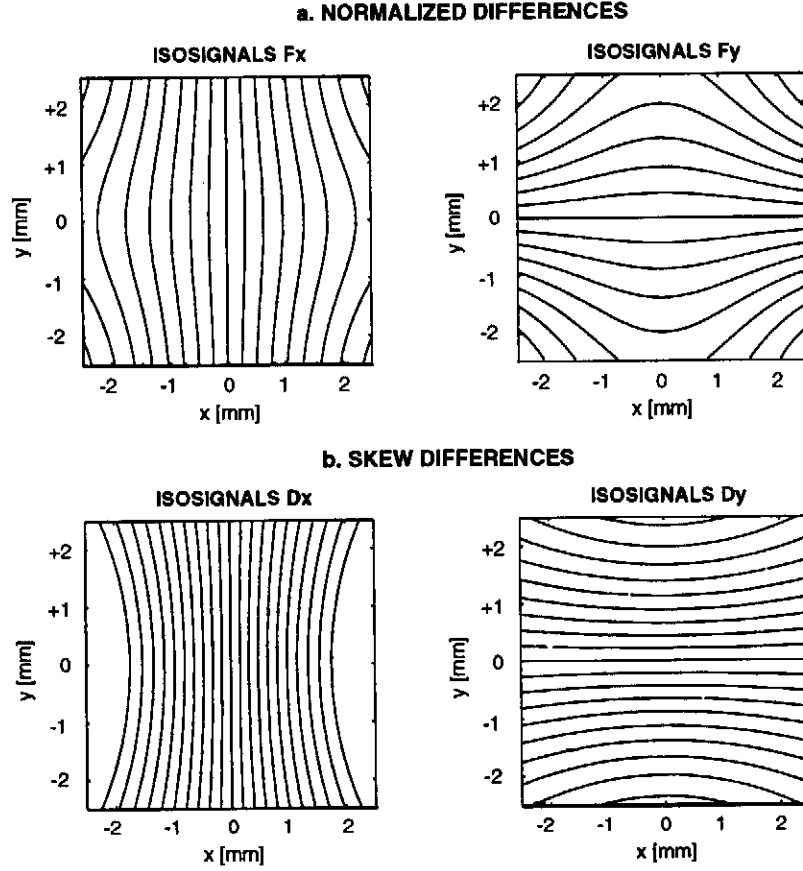


Figure 5.7: a) Signalfunctions for a quadratic array using normalized differences. b) Signalfunctions for the same array using skew differences. The amplitude difference between two isosignal lines is in any plot $\Delta F = \Delta D = 0.1$.

The base data of this analysis was calculated analytically for a model BPM fulfilling the design specifications. The maximum error for the reconstructed beam position is $\sigma_{x,y} = 2 \mu\text{m}$ inside the region of $|x|, |y| \leq 500 \mu\text{m}$. To measure beam offsets outside the linear region, a correction term has to be added to x_1 and y_1 :

$$x_2 = x_1 + K_x(x_1, y_1) \quad \text{and} \quad y_2 = y_1 + K_y(y_1, x_1) \quad (5.17)$$

A polynomial utilizing the odd symmetry in the primary variable and even symmetry in the secondary can serve this purpose [61]. After testing several trials a polynomial with six free parameters turned out to provide a sufficient error margin. Hence the beam position can be calculated with

$$\begin{aligned} x_2 &= a \cdot x_1 + b \cdot x_1^3 + c \cdot x_1 \cdot y_1^2 + d \cdot x_1 \cdot y_1^4 + e \cdot x_1^3 \cdot y_1^2 + f \cdot x_1^5 \\ y_2 &= A \cdot y_1 + B \cdot y_1^3 + C \cdot y_1 \cdot x_1^2 + D \cdot y_1 \cdot x_1^4 + E \cdot y_1^3 \cdot x_1^2 + F \cdot y_1^5. \end{aligned} \quad (5.18)$$

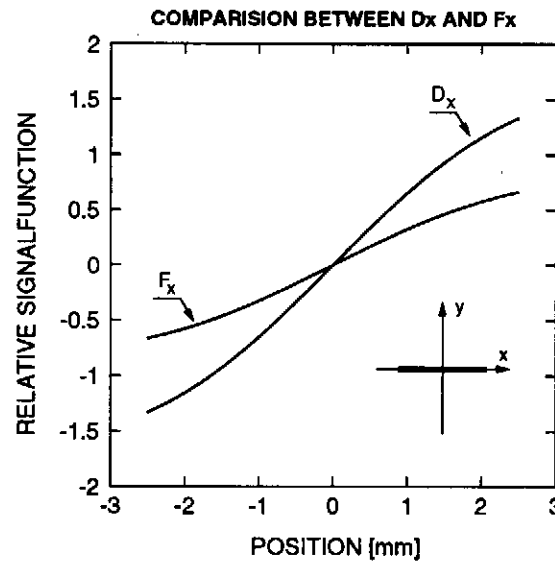


Figure 5.8: Relative signalfunctions calculated with normalized (F_x) and skew (D_x) differences for beam positions along the x -axis.

The coefficients ($a, \dots, f; A, \dots, B$) can be resolved by a least-square fit of the polynomials in Eq. 5.18 to BPM data.

It seems necessary to divide the task into two steps with different boundary conditions. For first orbit measurements the effective range should be quite big ($|x|, |y| \leq 2.5$ mm) so that most of the BPM profile is covered. Requirements on resolution are here relaxed and may exhibit a few hundred μm . For accurate beam orbit measurements, in particular required for the beam based alignment procedure, the resolution should be in the order of a few μm . Such measurements have to be performed in a smaller effective range of $|x|, |y| \leq 1$ mm. For both scenarios fit parameters were estimated under the assumptions that the measured voltages are gain calibrated and that each BPM has slot center angles as designed. In Tab. 5.2 fit parameters for horizontal and vertical beam positions are summarized. The maximum error for each direction caused by the fit is $\sigma_{max} = 100 \mu\text{m}$ close to the periphery of the effective range of $|x|, |y| \leq 3$ mm while for the smaller range of $|x|, |y| \leq 1$ mm the maximum error goes down to $\sigma_{max} = 0.2 \mu\text{m}$. The mean error for the bigger range is $\sigma_{mean} = 10 \mu\text{m}$ and for the smaller array $\sigma_{mean} = 0.1 \mu\text{m}$.

These fit errors will increase dramatically if the model is not a sensible description of the BPM with respect to slot angles, beam pipe diameter, and gains. An erroneous evaluation of the slot angles by $\pm 0.2^\circ$ will increase errors by one order of magnitude. A false estimation of the gains by ± 0.005 will increase the errors by

	$ x , y \leq 3 \text{ mm}$		$ x , y \leq 1 \text{ mm}$	
	ND [mm]	SD [mm]	ND [mm]	SD [mm]
a	0.992967	1.106868	0.992759	0.993415
b	0.010500	- 0.053104	0.044221	0.042422
c	- 0.040048	- 0.101595	-0.073736	0.042094
d	0.000159	0.034727	0.002924	0.005358
e	- 0.004176	0.065327	0.007251	0.010508
f	0.016065	0.024018	0.003897	0.005043
A	0.908604	1.106844	0.992539	0.993393
B	0.060473	-0.110667	0.044683	0.042419
C	-0.110667	-0.101597	-0.178980	0.042095
D	0.005681	0.034730	0.013092	0.005359
E	-0.020281	0.065325	0.000163	0.010507
F	0.008516	0.024015	0.003702	0.005042

Table 5.2: Fit parameters to reconstruct the horizontal and vertical beam position from signal functions obtained by normalized (ND) and squew differences (SD).

a factor of five which is tolerable for the smaller region. In consequence, the model describing the response of each individual BPM channel should be characterized with high accuracy and iterative until the desired precision is reached.

Chapter 6

Conclusion and Outlook

A new type of waveguide beam position monitor (BPM) has been developed for the use at the TESLA Test Facility Free Electron Laser (TTF FEL). Tests in laboratory on a testbench as well as under beam conditions have proven the functionality of the design.

The operation principle of the waveguide BPM is based on the coupling to the electromagnetic field co-propagating with the electron beam providing a high resolution and non-destructive position measurement. A fractional part of the beam field is decoupled through four slots arranged symmetrically around the beam pipe. The slot coupling can be described with model derived from a modified Bethe theory. Special T-ridge waveguides were used to reduce the waveguide size and to enhance the coupling. Because of the limited space in vertical direction, each BPM unit is split into two symmetric pairs of ports, separated by $3/2$ undulator wavelength in beam direction. At the end of each waveguide, a coaxial adapter is flange-mounted to the beam chamber. The cutoff frequency of the waveguide is at 8.99 GHz, the working frequency of the first step in the read-out electronics at 12 GHz. Simulations using the MAFIA package were performed in order to optimize the coupling to a level of 1% for a centered beam. The response of the BPM for an offset beam can be modeled by image charge calculations. Based on the image charge model, a calibration technique was developed providing intrinsic BPM parameters from a small number of position measurements. In particular, a beam based technique enables a precise characterization of each BPM channel: gain, coupling slot angles, and local beam pipe diameter can be evaluated with methods tested and found to be in accord with testbench measurements. The image charge model is adjustable to real BPMs with only a few parameters describing the complete BPM response. With iterative measurements and customization of the model, improvements of BPM characteristics

can be achieved and hence more precise orbit measurements are possible. With beam based alignment procedures global and local orbit minimization methods are under development.

Improvements of the BPM system are possible at theoretical level as well as in hardware designs. The modelling of the BPM response was done so far under the assumption of a point-like coupling slot. Including a finite size of the slot in the model would significantly improve the accuracy for the response of beam displacements far off-center. Up to now, the description for beam offsets is only valid in a circular region with $r \leq b/2$, where b is the beam pipe.

A redesign of the waveguide aiming at a lower working frequency would make easier the development of signal processing electronics and reduce their costs. A possible solution would be the use of rectangular coaxial waveguide with a working frequency around 6 GHz instead of the T-ridge waveguide. First design studies are promising regarding the coupling and functionality of such a design.

Appendix A

Beam Field Distribution

In this section a closed form expression for the electromagnetic field distribution of a round beam in a circular beam pipe is derived. This is of particular interest because the waveguide BPM senses the magnetic field of the beam.

If an electron beam is moving in a circular, conducting beam pipe, then there is an electromagnetic field accompanying the beam and an equal magnitude, opposite charge, beam current density on the inner wall of the beam pipe. In the limit of a relativistic beam the field inside the beam pipe looks like a transverse-electric-magnetic (TEM) wave propagating down the beam pipe at the beam velocity. If the beam is centered in the beam pipe, the field as well as the wall current density is uniformly spread around the beam. For an offset beam, this uniformity is disturbed. The waveguide BPM senses the magnetic field perturbation and the determination of the beam position is possible with the analysis of the relative amplitude of the induced signals.

For a beam current I_b in the center of a circular beam pipe of radius b , the azimuthal magnetic field at the chamber surface is

$$H_o = \frac{I_b}{2\pi b}. \quad (\text{A.1})$$

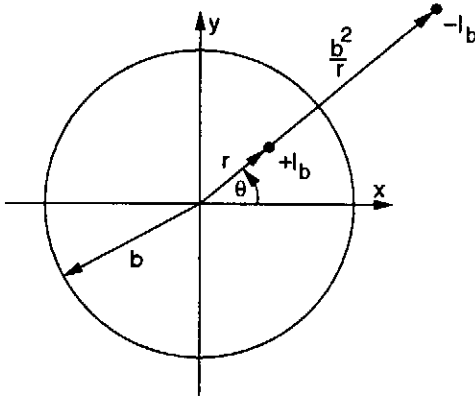
For a beam with offset r from the center the tangential magnetic field H_t can be calculated by an image current $-I_b$ as illustrated in Fig. A.1

$$H_t = H_r \cos \beta. \quad (\text{A.2})$$

The beam magnetic field H_r can be calculated with Biot-Savart's law according to

$$H_r = \frac{I_b}{2\pi d} \quad (\text{A.3})$$

a) IMAGE CHARGE



b) TANGENTIAL MAGNETIC FIELD

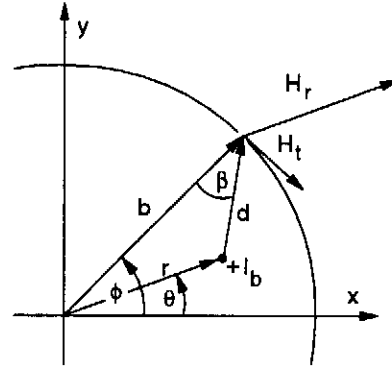


Figure A.1: a) Beam current I_b and associated image current $-I_b$ for an offset beam. b) Notation for the determination of the tangential magnetic field at the coupling slot location for an offset beam.

where d is the beam to slot center distance, if the slot center is located at (b, ϕ) . The problem can be regarded as an electro-static 2D problem in a cylindrical reference frame. The tangential magnetic field amplitude at the location of the coupling slot center can be derived from the field induced by the beam current I_b and by its image current $-I_b$. The field induced by the beam current I_b is given by

$$H_t = \frac{I_b \cos \beta}{2\pi d}. \quad (\text{A.4})$$

The aim of the following computation is to express H_t in beam offset coordinates (r, θ) and slot coordinates (b, ϕ) rather than in beam-to-slot distance d and beam-to-center angle β . Using trigonometric identities β can be expressed with

$$r^2 = b^2 + d^2 - 2bd \cos \beta \quad \Leftrightarrow \quad \cos \beta = \frac{b^2 + d^2 - r^2}{2bd}. \quad (\text{A.5})$$

The beam-to-slot distance d can be expressed as

$$d^2 = b^2 + r^2 - 2br \cos(\phi - \theta). \quad (\text{A.6})$$

Dividing Eqs. A.5 and A.6 and then inserting the result in Eq. A.4 gives the tangential field amplitude of the beam current at the slot center

$$H_t^+ = \frac{I_b}{2\pi b} \frac{1}{2} \left(1 + \frac{b^2 - r^2}{b^2 + r^2 - 2br \cos(\phi - \theta)} \right). \quad (\text{A.7})$$

The computation for the magnetic field induced by the image current $-I_b$ runs similar giving

$$H_t^i = \frac{I_b}{2\pi b} \frac{1}{2} \left(-1 + \frac{b^2 - r^2}{b^2 + r^2 - 2br \cos(\phi - \theta)} \right). \quad (\text{A.8})$$

The total tangential field H_t is the superposition of H_t^+ and H_t^- and reads as

$$H_t = H_o \cdot \frac{b^2 - r^2}{b^2 + r^2 - 2br \cos(\phi - \theta)}. \quad (\text{A.9})$$

Normalized with H_o this leads to an expression for the relative signal amplitude S_i as sensed by a coupling slot at (b, ϕ_i) for a beam at (r, θ)

$$S_i = \frac{b^2 - r^2}{b^2 + r^2 - 2br \cos(\phi_i - \theta)}. \quad (\text{A.10})$$

The right hand term in Eq. A.10 can be expressed in cartesian coordinates with

$$S_i = \frac{b^2 - (x^2 + y^2)}{b^2 + (x^2 + y^2) - 2(x_s x + y_s y)} \quad (\text{A.11})$$

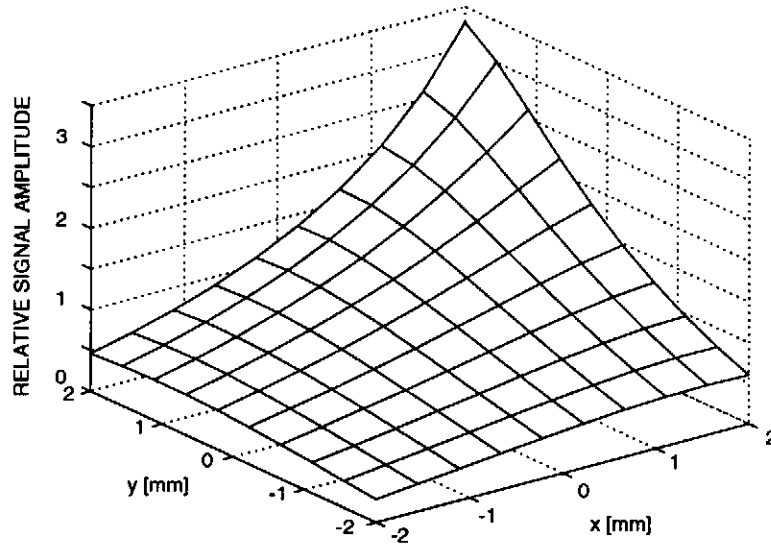
for a beam at (x, y) detected by a slot centered at (x_s, y_s) . In Fig. A.2a the relative signal amplitude S_1 is plotted according to Eq. A.10 for a square region in the BPM plane for a coupling slot with center located at $\phi_1 = 36^\circ$ with the horizontal axis. When the beam current moves in the BPM plane on one of the curves illustrated in Fig. A.2b the signal sensed by the coupling slot will not change. Therefore these curves are called isosignal curves.

The right hand term in Eq. A.9 describing the magnetic field of a bunch current can be expanded into an infinite series

$$H_t = H_o \left[1 + 2 \sum_{n=1}^{\infty} \left(\frac{r}{b} \right)^n \cdot \cos[n(\phi - \theta)] \right]. \quad (\text{A.12})$$

The field distribution of a bunch current can be approximated with its multipole terms with angular dependency. The electric field E_r is connected to the magnetic field H_t according to $E_r = Z_o \cdot H_t$ where Z_o is the wave impedance.

a) RELATIVE SIGNAL AMPLITUDE



b) ISOSIGNAL CURVES

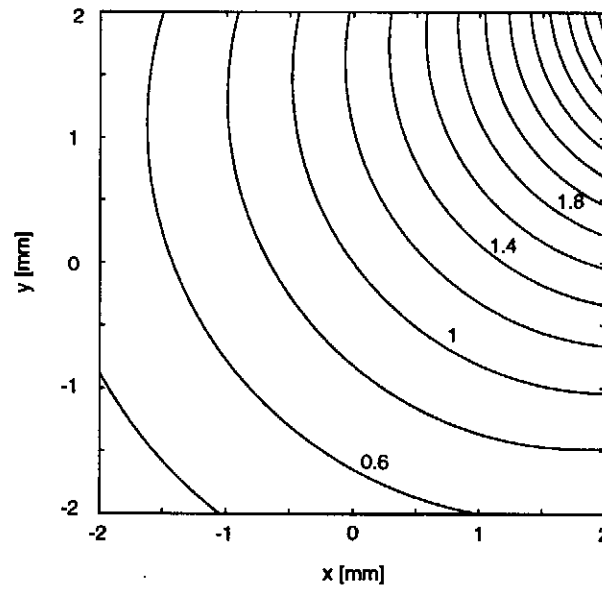


Figure A.2: a) Relative signal amplitude sensed by a coupling slot with center at $\phi_1 = 36^\circ$ according to Eq. A.10. b) Isosignal curves for the same region.

Appendix B

Guided Waves in Rectangular Structures

Waveguides are used for lowloss and routable transfer of high frequency electromagnetic waves through space. Basically a waveguide consists of a hollow tube with a cross-section that is uniform along the direction of propagation. In Fig. B.1 such a situation is illustrated. Conducting walls in the parallel to z -

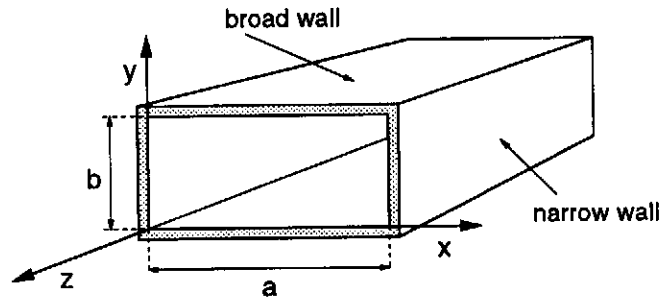


Figure B.1: Rectangular waveguide.

axis introduce boundary conditions to the field describing equations such that solutions are in the form of a propagating wave in z -direction like

$$f(x, y) \cdot \exp(i(kz - \omega t)) \quad (\text{B.1})$$

where k is the wavenumber and ω the frequency of the wave, respectively. The amplitude function $f(x, y)$ will be determined in the following. The boundary conditions for the electric \vec{E} fields and magnetic \vec{H} fields are due to the fact that there can not exist an electric field component inside the perfect conducting walls. Therefore the transverse field components of \vec{E} must vanish. The normal

component of the magnetic field can only be continuous and perpendicular to the electric field. Hence also the normal component of \vec{H} vanishes, and the boundary conditions can be written like

$$\begin{aligned} E_y = E_z = H_x = 0 & \quad \text{for} \quad x = 0 \quad \text{and} \quad x = a \\ E_x = E_z = H_y = 0 & \quad \text{for} \quad y = 0 \quad \text{and} \quad y = b. \end{aligned}$$

The following ansatz for the particular field components follows from the application of Maxwell's equations with free parameters:

$$\begin{aligned} E_x &= A \cos\left(\frac{n\pi x}{a}\right) \sin\left(\frac{m\pi y}{b}\right) \exp(i(kz - \omega t)) \\ E_y &= B \sin\left(\frac{n\pi x}{a}\right) \cos\left(\frac{m\pi y}{b}\right) \exp(i(kz - \omega t)) \\ E_z &= C \sin\left(\frac{n\pi x}{a}\right) \sin\left(\frac{m\pi y}{b}\right) \exp(i(kz - \omega t)) \\ H_x &= A' \sin\left(\frac{n\pi x}{a}\right) \cos\left(\frac{m\pi y}{b}\right) \exp(i(kz - \omega t)) \\ H_y &= B' \cos\left(\frac{n\pi x}{a}\right) \sin\left(\frac{m\pi y}{b}\right) \exp(i(kz - \omega t)) \\ H_z &= C' \cos\left(\frac{n\pi x}{a}\right) \cos\left(\frac{m\pi y}{b}\right) \exp(i(kz - \omega t)) \end{aligned}$$

with m and n positive integer. Any solution for the field equation must also fulfill the wave equation for any field component $g(\vec{r}, t)$ of \vec{E} and \vec{H} :

$$\left(\Delta - \frac{1}{c^2} \frac{\partial^2}{\partial t^2}\right) g(\vec{r}, t) = 0. \quad (\text{B.2})$$

This condition is fulfilled if

$$\left(\frac{n\pi}{a}\right)^2 + \left(\frac{m\pi}{b}\right)^2 + k^2 = \frac{\omega^2}{c^2}. \quad (\text{B.3})$$

For guided waves k is only real if

$$\omega \geq \omega_{nm} \quad \text{with} \quad \omega_{nm} = c \sqrt{\left(\frac{n\pi}{a}\right)^2 + \left(\frac{m\pi}{b}\right)^2}. \quad (\text{B.4})$$

The cutoff frequency of a particular mode in a waveguide is ω_{nm} , waves with frequencies $\omega \geq \omega_{nm}$ can propagate inside the waveguide in this mode while waves with $\omega < \omega_{nm}$ are damped. For waveguides with $a > b$ below the ω_{10} no propagation is possible.

In the next step the parameters A , A' , B , B' , C , and C' are determined. For

this the ansatz equations are inserted into Maxwell's equations:

$$\vec{\nabla} \vec{E} = 0 \Rightarrow A \frac{n\pi}{a} + B \frac{m\pi}{b} = ikC \quad (\text{B.5})$$

$$\vec{\nabla} \vec{H} = 0 \Rightarrow A' \frac{n\pi}{a} + B' \frac{m\pi}{b} = -ikC' \quad (\text{B.6})$$

$$\vec{\nabla} \times \vec{E} = -\frac{1}{c} \frac{\partial}{\partial t} \vec{H} \Rightarrow ikB - C \frac{m\pi}{b} = -i \frac{\omega}{c} A' \quad (\text{B.7})$$

$$C \frac{n\pi}{a} - ikA = -i \frac{\omega}{c} B' \quad (\text{B.8})$$

$$A \frac{m\pi}{b} - B \frac{Dn\pi}{a} = -i \frac{\omega}{c} C' \quad (\text{B.9})$$

$$\vec{\nabla} \times \vec{H} = \frac{1}{c} \frac{\partial}{\partial t} \vec{E} \Rightarrow ikB' - C' \frac{m\pi}{b} = i \frac{\omega}{c} A \quad (\text{B.10})$$

$$-C' \frac{n\pi}{a} - ikA' = i \frac{\omega}{c} B \quad (\text{B.11})$$

$$-A' \frac{m\pi}{b} + B' \frac{Dn\pi}{a} = i \frac{\omega}{c} C \quad (\text{B.12})$$

It is possible to create Eqs. B.10 to B.12 with linear combinations of Eqs. B.7 to B.9. The remaining five equations set up a homogenous, linear system of equations with six free parameters. This set of equations can be described in terms of two new parameters, called D and D' , which is equivalent to Eqs. B.5 to B.9:

$$\begin{aligned} A &= \frac{n\pi}{a} kD + \frac{m\pi \omega}{b c} D' & A' &= \frac{n\pi}{a} kD' - \frac{m\pi \omega}{b c} D \\ B &= \frac{m\pi}{b} kD - \frac{n\pi \omega}{a c} D' & B' &= \frac{m\pi}{b} kD' - \frac{n\pi \omega}{a c} D \\ C &= -i \left(\frac{D' \omega^2}{c^2} - k^2 \right) D & C' &= i \left(\frac{D \omega^2}{c^2} - k^2 \right) D'. \end{aligned}$$

Because the boundary condition for the longitudinal electric field differs from that for the longitudinal magnetic field, one can distinguish between two categories of field configurations:

- From $D' = 0$ and $D \neq 0$ follows that $H_z = 0$, there exist only transverse magnetic field components. These waves are called Transverse Magnetic (TM) waves. Non-trivial solutions exist only if $m > 0$ and $n > 0$. The lowest TM-mode, which is able to propagate in a waveguide has a cutoff frequency

$$\omega_{TM,11} = c\pi \sqrt{\frac{1}{a^2} + \frac{1}{b^2}}.$$

- From $D = 0$ and $D' \neq 0$ follows that $E_z = 0$ resulting in Transverse Electric (TE) modes. Here the lowest mode is described when one of the indices n or m is not equal to zero. In case of $a > b$ the lowest TE-mode has a cutoff frequency

$$\omega_{TE,10} = \frac{c\pi}{a}.$$

The field pattern of the TE_{10} is illustrated in Fig. B.2 Also circular waveguides

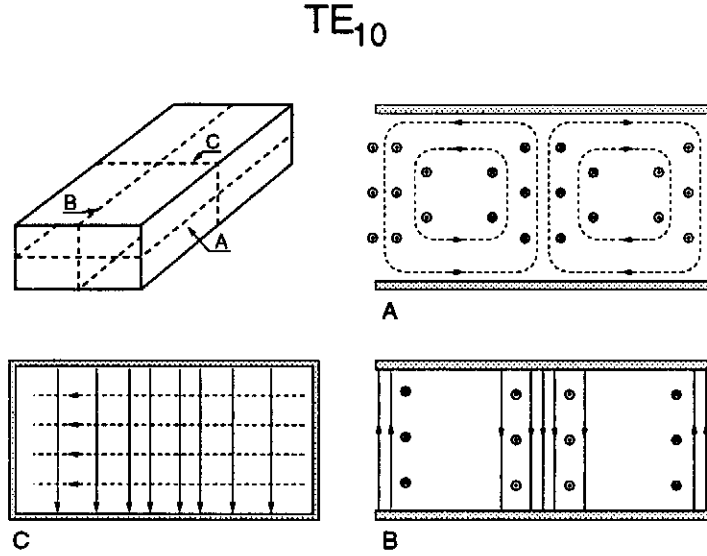


Figure B.2: Projection of the field pattern of the lowest mode which can propagate inside a rectangular waveguide. The electric field is indicated by solid lines, the magnetic field by dashed lines.

can be used for the transport of electromagnetic waves. Calculating the cutoff frequency runs similar, in a cylindrical reference frame with Besselfunction-like solutions for the electric and magnetic fields. The cutoff frequency for a circular waveguide is determined by the diameter of the waveguide and limits the propagation of electromagnetic waves to wavelengths which are less than the diameter of the pipe. The mode with the lowest cutoff frequency is the TE_{11} -mode with

$$\omega_{11} = \frac{cx'_{11}}{R} \quad (B.13)$$

where R is the waveguide radius and $x'_{11} = 1.841$ the root of the first derivative of the Besselfunction $J'_1(x)$.

Some Useful Relations

The wavenumber in the direction of propagation is defined with

$$k_z = \sqrt{k^2 - k_{nm}^2}.$$

The transverse electric and magnetic fields inside a waveguide are orthogonal to each other and related with the wave impedance:

$$\frac{E_x}{H_y} = -\frac{E_y}{H_x} = \pm Z_F$$

whereas the wave impedance Z_F is different for TE and TM waves

$$Z_F^{TM} = Z \sqrt{1 - (k_{mn}/k)^2} = \frac{k_z}{\omega \epsilon} \quad \text{and} \quad Z_F^{TE} = \frac{Z}{\sqrt{1 - (k_{mn}/k)^2}} = \frac{\omega \mu}{k_z}.$$

The free wave impedance is defined with $Z = \sqrt{\mu/\epsilon}$ and is $Z_o = 377 \, \Omega$ for vacuum. The power flow inside a waveguide of a particular mode can be calculated with the Poynting-vector

$$\vec{S} = \frac{1}{2}(\vec{E} \times \vec{H}^*).$$

The mean power flow can be computed from the mode amplitudes E_o and H_o if the wave is propagating in z -direction with

$$\bar{S}_z = \frac{1}{2} E_o \cdot H_o = \frac{1}{2Z_F} E_o^2 = \frac{Z_F}{2} H_o^2.$$

The power propagated is the integral of \bar{S}_z , calculated over the transverse section of the waveguide.

Appendix C

Remarks on BPM Resolution

The resolution of a BPM describes the precision of relative beam offset measurement, and is influenced by the signal to noise ratio (SNR) and by the quality factor of the position reconstruction algorithm.

The induced signal amplitude for one BPM channel V_S depends linearly on the bunch charge q and the coupling to the beam field k_s like

$$V_S = k_s \cdot Z \cdot q \cdot B \quad (\text{C.1})$$

where B denotes the bandwidth of the first signal processing element, usually a filter and Z its impedance. The noise amplitude in this bandwidth is [62]

$$V_N = F \cdot \sqrt{k_B \cdot B \cdot Z \cdot T} \quad (\text{C.2})$$

at temperature T and with Boltzmann's constant k_B and the noise figure F of the electronics. The signal to noise ratio is then defined by $\text{SNR} = V_S/V_N$. By using the expression for the position calculation out of signalfunctions, e.g. the horizontal position (see section 5.6.1)

$$x = b_x \cdot F_x = b_x \cdot \frac{L - R}{L + R} \quad (\text{C.3})$$

the horizontal resolution can be derived to

$$\delta x = \frac{b_x}{\sqrt{2}} \cdot \frac{1}{\text{SNR}} \quad (\text{C.4})$$

as a figure of merit for the minimal measurable offset. High signal amplitude V_S and low monitor constant b_x cause a high precision in relative offset measurements. Raising the bandwidth B will also result in a higher signal amplitude, but the noise level will be increased, too. Furthermore the resolution as defined in Eq. C.4 will be spoiled by noisy signal processing electronics elements with a finite noise figure. In Fig. C.1 isoresolution curves are illustrated giving boundary conditions for the design of signal processing electronics.

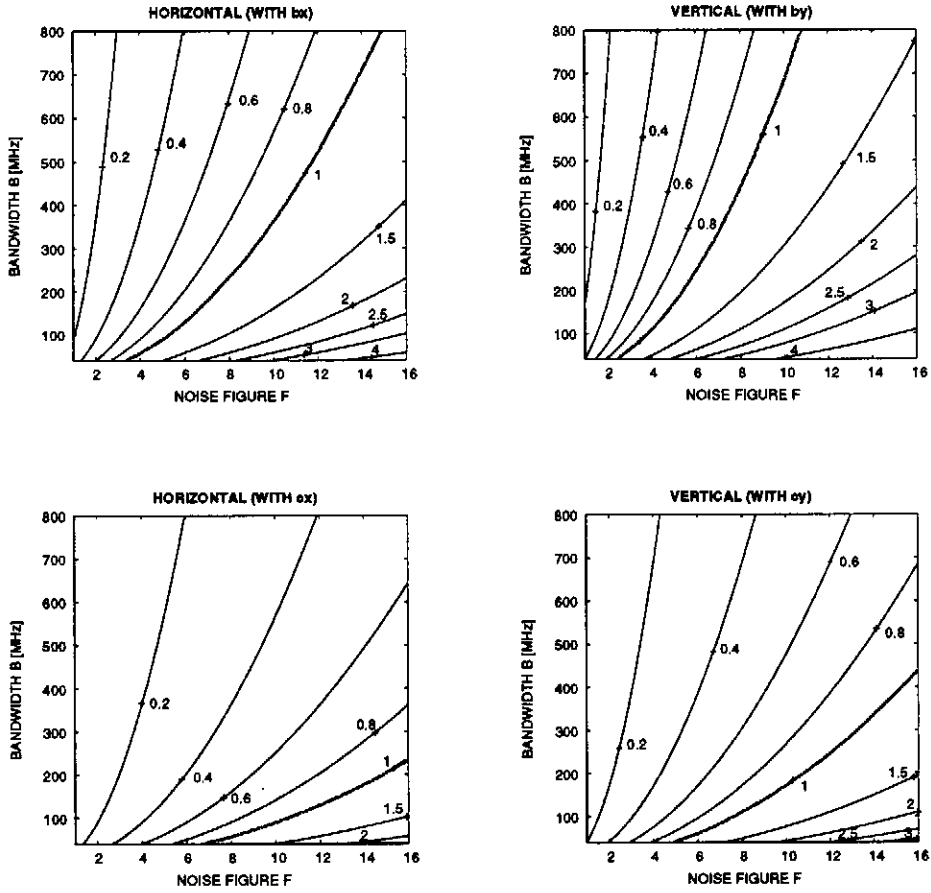


Figure C.1: Isoresolution curves for different monitor constants b_x , b_y , c_x , and c_y in the two-dimensional parameter space of bandwidth B and noise figure F of signal processing elements. The $1 \mu\text{m}$ resolution curve highlighted in each plot indicates the border of the required resolution for both parameters.

Appendix D

Electro Discharge Machining

The waveguide structure can be fabricated using Electrical (or electro) Discharge Machining (EDM) [63]. EDM is a material removal technique which uses electricity to remove metal by means of spark erosion. In industry, this process is used in making high-precision molds, dies, or machine parts. There are three basic components for the EDM technique: an electrode, a dielectric fluid, and a conductive workpiece. The electrode is the cutting tool for the EDM process. It cuts the workpiece with the negative shape of the electrode. Here the workpiece is the raw vacuum chamber slab. This slab is sunk into a dielectric fluid where the electrode is moved by a precision mover to the material. High voltage is then applied between the electrode and the workpiece. A controlled spark from the electrode to the workpiece causes a small part of the workpiece to melt and vaporize. The dielectric fluid helps to create and control the sparking. It provides a shield between the electrode and the workpiece, also it is used as a flushing agent to remove the resolidified particles from the cutting area. In this way, the electrode is sinkered from the side into the vacuum chamber slab until it reaches the desired depth. After cleaning the chamber is ready for the following production steps. In this way, two prototypes with eight channels and all 40 waveguide channels for the third undulator modules were fabricated.

Bibliography

- [1] J. Rossbach for the TESLA FEL Study Group, A VUV free electron laser at the TESLA test facility at DESY; Nucl. Instr. Meth., A375(1996)269.
- [2] A VUV Free electron Laser at the TESLA Test Facility; Conceptional Design Report, TESLA-FEL 95-03, DESY, 1995.
- [3] TESLA Test Facility Linac Design Report, Editor: D. A. Edwards; DESY Print, 1995.
- [4] R. Brinkmann, G. Materlik, J. Rossbach, A. Wagner, Conceptual Design Report of a 500 GeV e^+e^- Linear Collider with Integrated X-ray Laser Facility; DESY 1997-048.
- [5] A. M. Kondratenko, E. L. Saldin; Part. Accel. 10(1980)207.
- [6] E. L. Saldin, E. A. Schneidmiller, M. V. Yurkov, The Physics of Free Electron Lasers An Introduction; DESY 1994-219.
- [7] J. B. Murphy, C. Pellegrini, Introduction to the Physics of the Free Electron Laser, Laser Handbook Vol. 6, North-Holland, 1990.
- [8] K. Wille, Physik der Teilchenbeschleuniger und Synchrotronstrahlungsquellen, 2. Auflage; Teubner, 1996.
- [9] S. Reiche, Numerical Studies for a Single Pass High Gain Free Electron Laser; PhD Thesis, University of Hamburg, 1999.
- [10] B. Faatz, J. Pflüger, Y. M. Nikitima; Nucl. Instr. Meth., A393(1997)380.
- [11] Y. M. Nikitima, J. Pflüger; Nucl. Instr. Meth., A375(1996)332.
- [12] G. Schmidt, U. Hahn, J. Pflüger, Concept of Electron Beam Diagnostics for the VUV SASE FEL at the TESLA Test Facility (TTF FEL) at DESY; Proc. of the FEL98 Conf., Williamsburg, USA, 1998, TESLA-FEL 98-06, 1998.

- [13] K. Wittenburg, H. Schultz, A Proposal for using Wire-Scanners at the LINAC Test Facilities; TESLA 94-15, DESY, 1994.
- [14] S. Striganov, G. Schmidt, W. Wittenburg, Estimation of the Signal from the Wire Scanner in the TTF; TESLA 99-08, DESY, 1999.
- [15] R. Lorenz, T. Kamps, M. Wendt, Beam Position Measurement inside the FEL-Undulator at the TESLA Test Facility Linac; Proc. of the DIPAC97 Workshop, Frascati, Italy, 1997.
- [16] R. Lorenz, Cavity Beam Position Monitors; Proc. of the 8th Beam Instrumentation Workshop, SLAC, Stanford, USA, 1998.
- [17] R. Lorenz et al., Beam Position Monitors inside the FEL-Undulator at the TESLA Test Facility Linac; Proc. of the PAC97 Conf., Vancouver, Canada, 1997.
- [18] J. S. T. Ng, A Beam Trajectory Monitor using Spontaneous Undulator Radiation at the TTF-FEL; TESLA-FEL 96-16, DESY, 1996.
- [19] S. Hillert et al., Test Results on the Silicon Pixel Detector for the TTF-FEL Beam Trajectory Monitor; Proc. of the FEL99 Conf., Hamburg, Germany, 1999.
- [20] M. Wendt, private communication, 1999.
- [21] T. Kamps, R. Lorenz, S. deSantis, Microwave Characterisation of the Waveguide BPM; Proc. of the PAC99 Conf., New York, USA, 1999.
- [22] K. F. Sander, G. A. L. Reed, Transmission and Propagation of Electromagnetic Waves; Cambridge University Press, 1978.
- [23] The MAFIA Collaboration, MAFIA Reference Manual V3.2, 1996.
- [24] R. Klatt et al., MAFIA - A Three-Dimensional Electromagnetic CAD System for Magnets, RF Structures and Transient Wake-Field Calculations, IEEE Proc. of the LINAC86 Conf., Geneva, Switzerland, 1986.
- [25] H. A. Bethe, Theory of Diffraction by Small Holes; Phys. Rev., Vol.66, No.7 and 8, 1944, pp163-182.
- [26] R. E. Collin, Field Theory of Guided Waves; IEEE Press, 1991.

- [27] S. deSanits, Radiation effects of slots and coupling holes in the vacuum chamber of particle accelerators; PhD thesis, University of Roma 'La Sapienza', 1998.
- [28] N. A. McDonald; IEEE Trans. Microwave Theory Tech., MTT-20, 689 (1972).
- [29] C. L. Matthei, L. Young, E. M. T. Jones, Microwave Matching Networks and Coupling Structures; McGraw Hill, 1964.
- [30] R. W. Anderson et al., S-Parameter Techniques for Faster, More Accurate Network Design, Test & Measurement Application Note 95-1; Hewlett Packard, 1995.
- [31] M. Dohlus, R. Lorenz, T. Kamps, H. Schlarb, R. Wanzenberg, Estimation of the Longitudinal Wake Field Effects in the TTF-FEL Undulator Beam Pipe and Diagnostic Section, TESLA-FEL-98-02, 1998.
- [32] S. Reiche, H. Schlarb, Simulation of Time-Dependent Energy Modulation by Wake Fields and its Impact on Gain in the VUV Free Electron Laser of the TESLA Test Facility; Proc. of the FEL99 Conf., Hamburg, Germany, 1999.
- [33] K. L. F. Bane, K. Sands, Wake Fields of Very Short Bunches in an Accelerating Cavity, SLAC-PUB-4441, 1987.
- [34] A. W. Chao, Physics of Collective Beam Instabilities in High Energy Accelerators; John Wiley and Sons, 1993.
- [35] T. Shintake, private communication, 1999.
- [36] H. H. Meinke, F. W. Gundlach, Taschenbuch der Hochfrequenztechnik, Band 2, Komponenten; Springer Verlag, 1992.
- [37] U. Hahn et al., Design and Performance of the Vacuum Chambers for the Undulator of the VUV FEL at the TESLA Test Facility; Proc. of the FEL99, Hamburg, Germany, 1999.
- [38] J. H. Cuperus, Monitoring of particle beams at high frequencies; Nucl. Instr. Meth., 145(1977)219.
- [39] J. P. Delahaye, The CLIC Study of a Multi-TeV e^\pm Linear Collider; Proc. of the PAC99, New York, USA, 1999.

- [40] CLIC Team, CTF2 design report: the CLIC test facility: CTF2 a two-beam test accelerator for linear collider studies, CERN/PS-96-29, 1996.
- [41] W. Schnell, Consideration of a Two-Beam RF Scheme for Powering an RF Linear Collider; CLIC-Note 85-07, 1985.
- [42] P. Bryant, WINAGILE, WINdows Alternating Gradient Interactive Lattice DEsign; available from the author, (<http://nicewww.cern.ch/~bryant>).
- [43] M. Schmitz, Status of the S-Band Test Facility; Proc. of the LC97, Zvenigorog, Russia, 1997.
- [44] D. Sprehn, Final Report on the Development of 150 MW S-Band Klystron; Proc. of Pulsed RF Sources for Linear Colliders, Shonan Village Center, Hayama, Kamagawa, Japan, 1996.
- [45] V. E. Kaljuzhny, N. Sobenin, M. Dohlus, N. Holtkamp et al., Investigations of a Hybrid Coupler for a 6 Meter S-Band Accelerating Structure; DESY M-96-05, 1996.
- [46] U. v. Rienen, Higher Order Mode Analysis of Tapered Disc-Loaded Waveguides Using the Mode Matching Technique; Particle Accelerators, 1993, Vol. 41, pp 173-201.
- [47] T. Kamps, Calibration of Waveguide Beam Position Monitors; Proc. of the FEL99 Conf., Hamburg, Germany, 1999.
- [48] K. Satoh, Recalibration of Position Monitors with Beams; Proc. of the PAC95 Conf., Dallas, USA, 1995.
- [49] D. Marquat, An Algorithm for least-squares estimation of nonlinear parameters; SIAM J. Appl. Math. Vol.11, pp431-441, 1963.
- [50] MATLAB, Mathworks Inc., 1999.
- [51] B. Faatz, J. Pflüger, Yu. M. Nikitina, Study of the undulator specifications for the VUV-FEL at the TESLA Test Facility; Nucl. Instr. Meth., A393(1997)380.
- [52] G. Schmidt, private communication, 1999.
- [53] T. O. Raubenheimer, R. D. Ruth, A Dispersion Free Trajectory Correction for Linear Colliders; Nucl. Instr. Meth., A302(1991)61.

- [54] K. Flöttmann, B. Faatz, E. Czuchry, J. Rossbach, Beam Based Alignment Procedure for an Undulator with Superimposed FODO-Lattice; TESLA-FEL 97-05, DESY, 1997.
- [55] C. E. Adolphsen et al., Beam-Based Alignment Technique for the SLC Linac; SLAC-PUB-4902, 1989.
- [56] P. Emma, Beam Based Alignment of Sector-1 fo the SLC Linac, SLAC-PUB-5787, 1992.
- [57] P. Castro, B. Faatz, K. Flöttmann, Beam Based Alignment for an undulator with superimposed FODO lattice; Nucl. Intr. Meth., A427(1999)12.
- [58] P. Castro, TTF FEL Beam-based Alignment by Dispersion Correction Using Micado Algorithm; TESLA-FEL 97-04, DESY, 1997.
- [59] B. Autin, Y. Marti, Closed Orbit Correction of A.G. Machines using a small Number of Magnets; CERN/ISR-MA/73-17, 1973.
- [60] P. Castro, Orbit Correction by Dispersion Minimization in an Undulator with Superimposed PODO Lattice; Proc. of the EPAC98, Stockholm, Sweden, 1998.
- [61] J. Borer, C. Bovet, D. Cocq, Algorithmes de Linearisation des Pick-Ups; LEP Note 582, 1989.
- [62] S. R. Smith, Beam Position Monitor Engineering; SLAC-PUB-7244, 1996.
- [63] H. Dubbel, Taschenbuch für den Maschinenbau (19. Auflage); Springer Verlag, Berlin, 1997.

Acknowledgments

In the first place I would like to thank my thesis advisors Prof. Dr. Eberhard Jaeschke and Prof. Dr. Heino Henke for their interest in my work, frequent helpful discussions and support.

I am indebted to Prof. Dr. Thomas Weis for his willingness to read this manuscript.

I would like to thank Dr. Jürgen Schreiber and Dr. Ronald Lorenz for their constant support and many discussions.

Among all the people from DESY Zeuthen and Hamburg and the collaborating institutes around the world working on the TTF project I would like to point out (in no particular order) Prof. Dr. Peter Schmüser, Dr. Gerald Schmidt, Dr. Siegfried Schreiber, Dr. Ulrich Hahn, Dr. Stefano de Santis, Dr. Hans Weise, Dr. Jörg Rossbach, Holger Schlarb, Dr. Marc Geitz, Sven Reiche, and Dr. Pedro Castro-Garcia. I thank the summer students Dominik Fischer and Bernhard Schmitt for supporting my investigations. Furthermore my thanks are due to Dr. Dirk Kamrad, Frank Ziegler, Peter Molnar, Daniel Ruschmeier, Michael Unger, and Dr. Sabine Riemann for being fantastic colleagues. I thank Dr. Martin Sachwitz, Frank Tonisch, Dr. Heinz Thom, Wolfgang Riesch, Roland Steinbecher, and Dr. Karl Trützschler for supporting the realization of the BPM tests.

I would like to thank Dr. Hans Braun and the CTF group for their support at the CLIC Test Facility as well as all members of the SBTF group for providing us beam time at the S-Band Test Facility.

Many thanks are due to the personnel of DESY Zeuthen for their support throughout the years.

All my love goes to my family and of course to Iris.

Hiermit erkläre ich, daß ich diese Arbeit selbständig verfaßt habe und keine anderen als die angegebenen Quellen und Hilfsmittel benutzt habe.

